

Quantum Hamiltonian Learning using Time-Resolved Measurement Data and its Application to Gene Regulatory Network Inference

Mohammad Aamir Sohail*, Ranga R. Sudharshan[†], S. Sandeep Pradhan*, Arvind Rao[†]

*Department of EECS, University of Michigan, Ann Arbor, USA

[†]Department of Computational Medicine and Bioinformatics, University of Michigan, Ann Arbor, USA

Abstract

We present a new Hamiltonian-learning framework based on time-resolved measurement data from a fixed local IC-POVM and its application to inferring gene regulatory networks. We introduce the quantum Hamiltonian-based gene-expression model (QHGM), in which gene interactions are encoded as a parameterized Hamiltonian that governs gene expression evolution over pseudotime. We derive finite-sample recovery guarantees and establish upper bounds on the number of time and measurement samples required for accurate parameter estimation with high probability, scaling polynomially with system size. To recover the QHGM parameters, we develop a scalable variational learning algorithm based on empirical risk minimization. Our method recovers network structure efficiently on synthetic benchmarks and reveals novel, biologically plausible regulatory connections in Glioblastoma single-cell RNA sequencing data, highlighting its potential in cancer research. This framework opens new directions for applying quantum-like modeling to biological systems beyond the limits of classical inference.

I. INTRODUCTION

Quantum Hamiltonian learning (QHL) refers to the task of inferring the parameters of a Hamiltonian associated with a many-body quantum system without requiring resources that scale exponentially with the system size. This task is essential in areas such as quantum simulation, condensed matter physics, and the characterization of quantum devices [1]–[6]. For example, in condensed matter physics, Hamiltonian learning allows the identification of effective spin-interaction models in quantum materials, based on spectroscopic measurements of spin excitations [6]. A conceptually straightforward approach to QHL is quantum process tomography [7]–[10]. However, this approach requires resources that scale exponentially with system size, making it impractical for real experiments. [11].

To overcome the prohibitive costs of process tomography, a wide range of efficient QHL methods have been developed across diverse settings. For instance, sample-efficient algorithms have been proposed for learning local Hamiltonians from Gibbs or thermal states [12]–[16], single eigenstates [17]–[20], and the steady state of the Hamiltonian [21], [22]. Additional methods focus on using measurements of local observables [23]–[25], short-time evolution [26]–[29], and time-resolved measurements [30], [31]. Several works have also proposed using a trusted quantum simulator to infer the Hamiltonian of an untrusted device [32]–[34]. Recent advances include scalable algorithms based on matrix product state (MPS), [35] and noise-resilient learning methods [29], [36]. Additionally, a series of works have demonstrated Heisenberg-limited scaling for Hamiltonian learning [37]–[41]. In other words, the error in estimated parameters scales as the inverse of total evolution time, rather than the square-root of total evolution time as seen in the standard quantum limit [42], [43].

QHL has been traditionally applied in quantum physics to understand particle interactions. However, this can be extended to understand the underlying interaction structure of complex systems, which may not be inherently quantum-scale but exhibit behavior that cannot be accurately described by classical probabilistic models. This broader viewpoint is central to the *quantum-like* modeling paradigm [44]–[46], which utilizes the mathematical tools of quantum information theory, such as non-commutative observables, superposition in Hilbert space, and quantum measurements modeled as positive operator valued measure (POVM), to model information processing in complex systems. As put forth in [47], the quantum formalism can be applied “not only to physical systems, but to systems of any origin — whether biological, social, or financial — as long as their behavior exhibits some distinguishing features of quantum systems”. The *quantum-like* paradigm has been explored in diverse fields beyond physics, including cognitive science, decision theory, finance, and neuroscience [47]–[51].

An interesting application where *quantum-like* modeling can offer an advantage is the inference of gene regulatory networks (GRNs). The transcriptional state of a cell is highly dynamic and tightly regulated by complex interactions between genes, often mediated through multiple proteins. Understanding these regulatory relationships is critical for deciphering cellular behavior and function, yet represents one of the fundamental challenges in systems biology. In recent years, the increasing availability of large-scale single-cell RNA sequencing (scRNA-seq) data [52], which essentially captures the expression levels of individual genes across cells, has greatly facilitated the development and refinement of computational tools for GRN inference. These datasets provide unprecedented resolution to capture cell-to-cell variability, enabling more accurate modeling of gene interactions across diverse cellular states and conditions. Current classical methodologies can be broadly classified into correlation-based [53] [54], tree-based ensemble methods [55] [56], information-theory-based [57], and Bayesian network-based models [58]. While these techniques have yielded valuable insights, they may fall short in capturing the nuanced and context-dependent nature of biological regulation. Empirical

studies increasingly show that gene-expression data can violate the classical law of total probability and present non-classical features such as interference of probabilities [49], [59]–[62], as well as violation of the Bell inequality in the macroscopic world [63]. Moreover, in cancer progression, certain cell types have been observed to exist in hybrid states, simultaneously expressing features of multiple phenotypes, in a manner reminiscent of quantum superposition [64], [65]. These observations suggest that the regulatory interactions in GRNs can be better modeled using a *quantum-like* paradigm.

Recent research has started to explore *quantum-like* models for inferring complex biological networks [66]–[70]. A quantum circuit model has been proposed in [66] for GRN inference from scRNA-seq data, where each gene is represented as a qubit. However, the circuit construction is sensitive to gene ordering, as it prioritizes genes with higher activation ratios in the qubit mapping. The model also relies on the (classical) KL divergence loss function [71], which requires evaluating joint probability distributions, resulting in computational costs that scale exponentially with network size. Furthermore, existing methods lack a systematic framework for integrating multi-omics data, such as genomics, transcriptomics, and proteomics, thereby limiting their effectiveness in practical biological applications.

Building on these observations, we propose that the QHL framework offers a powerful approach to modeling gene regulatory dynamics. It enables scalable and sample-efficient inference of complex, nonlinear interactions that classical methods might overlook. Additionally, it offers a flexible foundation for integrating multi-omics data. However, applying QHL to GRNs is challenging from multiple perspectives. Existing QHL approaches are primarily tailored for quantum many-body systems and rely on entangled initial states, random Pauli measurements, Gibbs states, or access to eigenstates, resources that do not have direct relevance in the context of GRNs. To address this gap, we formulate a new Hamiltonian learning problem grounded in statistical learning theory and motivated by the biology of GRNs. Below, we summarize the key contributions of this work.

1. **Hamiltonian Learning from Time-Resolved Measurement Data:** We formulate a new Hamiltonian learning problem using measurement outcomes from a fixed local informationally complete POVM (IC-POVM) collected at multiple times, starting from a fixed initial state. We characterize the sample complexity in terms of the number of time samples, denoted as N_t , and the number of measurement outcomes per time sample, denoted as N_c , sufficient to achieve small estimation error with high probability (see Theorem 1). Both N_t and N_c scale polynomially with the number of qudits. Furthermore, we establish a finite-sample uniform convergence bound for the empirical loss (see Theorem 2).
2. **Quantum Hamiltonian-Based Generative Modeling of Gene Expression:** We instantiate our QHL framework in the context of GRNs and introduce the quantum Hamiltonian-based gene-expression model (QHGM) (see Fig. 1) for simulating GRNs. In this model, genes are treated as qubits. The QHGM generates gene-expression

data by modeling regulatory interactions as *quantum-like* couplings encoded in a parameterized Hamiltonian. Each single-qubit IC-POVM outcome corresponds to the expression level of an individual gene, and together they yield the gene-expression profile of a cell. We employ pseudotime [72], which orders cells along inferred developmental trajectories derived from scRNA-seq data, as an approximate analogue of physical evolution time. We construct a Hamiltonian for GRN by defining biologically interpretable interaction terms using tensor products of computational basis states.

3. Scalable and Sample-Efficient Network Inference Algorithm: We develop a scalable variational quantum network inference algorithm (VQ-Net) for learning QHGM parameters from scRNA-seq data (see Methods and Fig. 2). VQ-Net is built on an empirical risk minimization framework and minimizes the negative log-likelihood loss over mini-batches of scRNA-seq data collected at multiple pseudotime bins.

4. Numerical Evaluation on Synthetic Data: We provide comprehensive numerical results and performance of VQNet on synthetic gene-expression data generated by QHGM (see Fig. 3). These experiments validate the theoretical sample-complexity bounds derived in our learning framework, demonstrating the trade-off among the number of time samples, the number of measurement samples per time, and estimation accuracy.

5. Application to glioblastoma scRNA-seq data: We apply our framework to scRNA-seq from glioblastoma (GBM) patients [73], focusing on the gene regulatory programs governing differentiation of OPC-like cells (see Fig. 4). GBM is the most common malignant primary brain tumor, with poor prognosis and complex cellular heterogeneity [74], [75]. To our knowledge, this is the first application of *quantum-like* modeling to infer biologically relevant regulatory networks in cancer research. Our results reveal potential GRN structures and interaction patterns that reflect the cellular plasticity within malignant OPC-like populations, opening new avenues for quantum-driven exploration of information flows in biological systems.

II. MAIN RESULTS

We have organized our findings into three main subsections. The first subsection presents our theoretical framework for Hamiltonian learning. The second subsection builds on this foundation by demonstrating how the same framework can be applied to infer GRNs. In the final subsection, we present numerical results on synthetic and real scRNA-seq data.

A. Hamiltonian Learning using Time Dynamics of IC-POVM

Definition 1 (Statistical Model). *Consider a Hamiltonian $H(\mathbf{w}) = \sum_{j=1}^c w_j H_j$ that acts on a quantum system of n qudits, each of dimension d . It consists of c local terms $\{H_j\}$ acting on a subset of qudits and a parameter vector $\mathbf{w} \in \mathcal{W}_B := \{\mathbf{w} \in \mathbb{R}^c : \|\mathbf{w}\|_2 \leq B\}$. For an evolution time t , define the corresponding evolved quantum state as follows: $\rho_t(\mathbf{w}) := U_t(\mathbf{w}) \rho_0 U_t^\dagger(\mathbf{w})$, where $U_t(\mathbf{w}) = \exp\{-i t H(\mathbf{w})\}$, and ρ_0 is the initial state. After the evolution, an IC-POVM measurement, denoted as $\Lambda := \{\Lambda_m : m \in \mathcal{M}\}$, is performed on each qudit,*

producing an outcome in a finite set \mathcal{M} . This results in a tensored-product measurement acting on the entire system of dimension $D = d^n$. This measurement generates an outcome vector $\mathbf{m} := (m^{(1)}, \dots, m^{(n)}) \in \mathcal{M}^n$ at time t according to the probability given as

$$\phi(\mathbf{m}|t, \mathbf{w}) := \text{tr}(\Lambda_{\mathbf{m}} \rho_t(\mathbf{w})),$$

where $\Lambda_{\mathbf{m}} = (\Lambda_{m^{(1)}} \otimes \dots \otimes \Lambda_{m^{(n)}})$.

Consider a set of N_t evolution times, denoted as $\mathcal{T} := \{t_1, t_2, \dots, t_{N_t}\}$, independently drawn from a design distribution $\pi(t)$ over $(0, t_{\max}]$. For each $t_i \in \mathcal{T}$, we are given N_c measurement outcomes, denoted as $\{\mathbf{m}_{(i,1)}, \dots, \mathbf{m}_{(i,N_c)}\}$. Here, $\mathbf{m}_{(i,k)}$ is a n -length vector that denotes the k -th outcome collected at time t_i . These outcomes are independently and identically generated according to the probability distribution $\phi(\mathbf{m}|t_i, \mathbf{w}^*)$ determined by (unknown) parameters $\mathbf{w}^* \in \mathcal{W}_B$, i.e., each measurement arises from an independent preparation of ρ_0 , followed by evolution for time t_i , and performing the IC-POVM Λ . Note that the outcomes $\{\mathbf{m}_{(1,k)}, \mathbf{m}_{(2,k)}, \dots, \mathbf{m}_{(N_t,k)}\}$ are independent but not identically distributed.

Objective: Given the collection of measurement outcomes across all times, our goal is to obtain an estimate $\widehat{\mathbf{w}} := \widehat{\mathbf{w}}(\{\mathbf{m}_{(i,k)}\}_{i=1, k=1}^{N_t, N_c}) \in \mathcal{W}_B$ of parameter \mathbf{w}^* such that for any $\delta \in (0, 1)$, a bound of the following form holds with probability at least $(1 - \delta)$:

$$\|\widehat{\mathbf{w}} - \mathbf{w}^*\|_2 \leq g(\delta, N_c, N_t).$$

To obtain an estimator $\widehat{\mathbf{w}}$ that meets the high-probability error bound stated above, we consider the empirical risk minimization framework. Given N_t time samples and N_c independent and identically distributed measurement outcomes for each time t , define the empirical and expected loss as follows

$$\widehat{L}(\mathbf{w}) := \frac{1}{N_t} \sum_{i=1}^{N_t} \frac{1}{N_c} \sum_{k=1}^{N_c} \ell(\phi(\mathbf{m}_{(i,k)}|t_i, \mathbf{w})) \quad \text{and} \quad L(\mathbf{w}) := \mathbb{E}_{t \sim \pi} [\mathbb{E}_{\mathbf{m} \sim \phi(\cdot|t, \mathbf{w}^*)} [\ell(\phi(\mathbf{m}|t, \mathbf{w}))]],$$

where $\ell(\cdot) := -\log(\cdot)$. Then, we obtain the minimizer of empirical loss $\widehat{L}(\mathbf{w})$ as

$$\widehat{\mathbf{w}} := \arg \min_{\mathbf{w} \in \mathcal{W}_B} \widehat{L}(\mathbf{w}).$$

Assumptions: We state the following assumptions. **A(i)** The expected loss function $L(\mathbf{w})$ is μ_0 -strongly convex (SC) over \mathcal{W}_B . **A(ii)** The likelihood function ϕ is bounded, $\phi(\mathbf{m}|t, \mathbf{w}) \geq p_{\min} > 0$ for all $\mathbf{m} \in \mathcal{M}^n, t \in (0, t_{\max}]$, and $\mathbf{w} \in \mathcal{W}_B$.

Our main result is a sample-efficient learning algorithm for the QHL problem. We provide a detailed proof in the Method section.

Theorem 1. *For the Hamiltonian learning problem described above, fix a confidence $\delta > 0$ and an empirical SC tolerance $\varepsilon > 0$. Under the assumptions stated above, if the number of sampled times N_t and the number of measurement outcomes per time N_c are chosen such that*

$$N_t = \tilde{\mathcal{O}}\left(\frac{c^3}{\varepsilon^2} \log\left(\frac{1}{\delta}\right)\right) \text{ and } N_c = \tilde{\mathcal{O}}\left(\frac{c^3}{\varepsilon^2} \log\left(\frac{N_t}{\delta}\right)\right),$$

where $\tilde{\mathcal{O}}$ hides logarithmic factors in c and $1/\varepsilon$, as well as fixed constants μ_0, B, t_{\max} , and p_{\min} . Then, with a probability at least $(1 - 2\delta)$, the empirical loss \hat{L} is $(1 - 2\varepsilon)\mu_0$ -strongly convex over \mathcal{W}_B .

Furthermore, suppose $\hat{\mathbf{w}} \in \text{interior}(\mathcal{W}_B)$ with probability 1. Then, with probability at least $(1 - 3\delta)$, the empirical minimizer satisfies

$$\|\hat{\mathbf{w}} - \mathbf{w}^*\|_2 \leq \mathcal{O}\left(\frac{1}{(1 - 2\varepsilon)\mu_0} \sqrt{\frac{c}{N_c} \log\left(\frac{N_t}{\delta}\right)}\right). \quad (1)$$

Scaling with system size. The above bounds show that the required number of sampled times N_t and the number of measurement results per time N_c scale polynomially with the number of Hamiltonian parameters. When the number of parameters c scales polynomially in n , then both N_t and N_c also scale polynomially with the number of qudits.

Insufficient N_t but N_c is large. Note that for a given sampled time t_i , it may happen that different parameter values can induce the same measurement distributions. In particular, for a given time t , there may exist $\mathbf{w} \neq \mathbf{w}^*$ such that $\phi(\cdot|t, \mathbf{w}) = \phi(\cdot|t, \mathbf{w}^*)$. If the number of time samples N_t is too small, such non-identifiability can persist across the entire set of sampled times, so that distinct parameters remain indistinguishable from the observed data. Increasing N_c only reduces the variance in estimating the per-time expected loss. As a result, increasing N_c alone cannot compensate for insufficient identifiability caused by the limited time samples.

Sufficiently large N_t but $N_c = 1$. If the number of time samples N_t becomes very large, taking only a single measurement at each time point is insufficient for accurate parameter recovery. When the number of measurements per time is small, the empirical estimate of the measurement distribution at each time is dominated by sampling noise. Consequently, although increasing N_t provides sufficient identifiability of the parameters, the information available at each time remains too noisy to be useful.

We next establish a finite-sample uniform convergence guarantee for the empirical loss \hat{L} around the expected loss L over \mathcal{W}_B . The following theorem shows that as the number of time samples N_t and the number of measurements per time sample N_c increase, \hat{L} uniformly concentrates around L , thus justifying the use of empirical risk minimization as a faithful approximation to the expected risk minimization problem.

Theorem 2. *Under the assumption A(ii), for any $\delta > 0$, the following non-asymptotic uniform deviation bound holds with probability at least $(1 - 4\delta)$:*

$$\sup_{\mathbf{w} \in \mathcal{W}_B} |\hat{L}(\mathbf{w}) - L(\mathbf{w})| \leq \frac{72\sqrt{\pi}cBL_p}{\sqrt{N_t}} + \frac{2\sqrt{2\log(2D)}}{p_{\min}\sqrt{N_c}} - 3\log p_{\min} \left(\sqrt{\frac{2\log(2/\delta)}{N_t}} + \sqrt{\frac{\log(2N_t/\delta)}{2N_c}} \right). \quad (2)$$

An important implication of this uniform convergence result is that it provides a key ingredient for establishing asymptotic strong consistency of the empirical minimizer as $N_t, N_c \rightarrow \infty$ (see [76, Theorem 4.10]).

B. Application to Gene Regulatory Network Inference

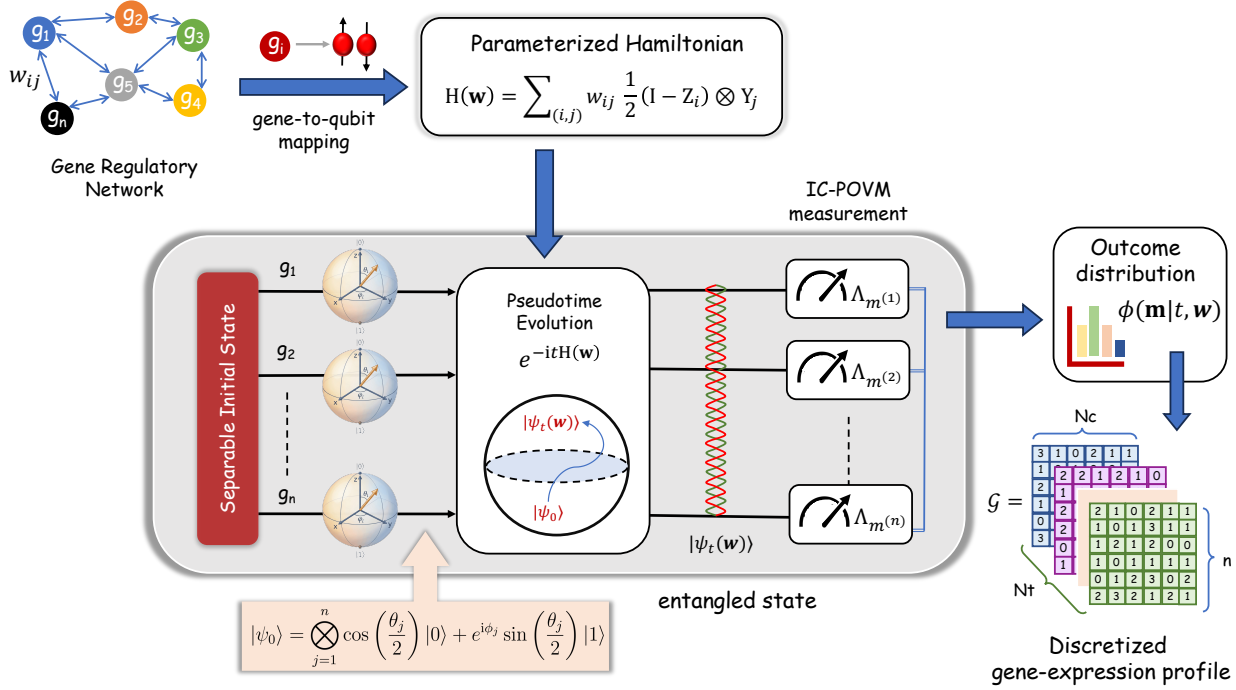


Figure 1: Overview of the quantum Hamiltonian-based gene-expression model (QHGM). A gene regulatory network (GRN) is mapped to a parameterized Hamiltonian $H(\mathbf{w})$, where the presence of gene g_i induces the action of a Pauli-Y operator on gene g_j with regulatory weights w_{ij} . The model begins from an initial separable state, representing independent gene states. As the system evolves along pseudotime, correlations between genes are gradually introduced, resulting in an entangled quantum state. At each pseudotime point, this state is measured using a fixed single-qubit IC-POVM, producing a probability distribution $\phi(\mathbf{m}|t, \mathbf{w})$ over measurement outcomes. Collecting repeated measurements outcomes at each pseudotime point yields discretized gene-expression profiles, denoted as \mathcal{G} , with dimension (N_t, N_c, n) that serve as the observable data for inference. Here, N_t is the number of pseudotime bins, N_c is the number of independently measured cells per bin, and n is the number of genes in the network.

Building on our QHL framework, we apply it to GRNs and obtain a statistical generative model for gene-expression data, which we call the *quantum Hamiltonian-based gene-expression model* (QHGM) (see Fig. 1). In QHGM, for simplicity of exposition, we represent each gene as a qubit. The computational basis states $|1\rangle$ and $|0\rangle$ correspond to the transcriptional state of the gene, indicating whether it is expressed or unexpressed in a cell, respectively. The model consists of three main components: (i) a Hamiltonian that encodes the

regulatory structure of the GRN, (ii) initial state preparation and pseudotime state evolution, and (iii) an IC-POVM measurement, each described in detail below.

1. Hamiltonian for GRNs: The regulatory interactions between genes are encoded in a parameterized Hamiltonian as

$$H(\mathbf{w}) = \sum_{(i,j) \in \mathcal{E}} w_{ij} \frac{1}{2}(\mathbf{I} - Z_i) \otimes Y_j, \quad (3)$$

where $\mathcal{E} := \{(i, j) : i, j \in \{1, 2, \dots, n\}, i \neq j\}$ and n is the number of genes in the network. The weights w_{ij} capture both the strength and direction of regulatory influence, with each w_{ij} quantifying the effect of gene g_i on gene g_j . A positive w_{ij} indicates activation, meaning that the presence of gene g_i promotes the expression of g_j , whereas a negative w_{ij} implies that g_i suppresses g_j . Each coefficient is bounded, i.e., $|w_{ij}| \leq w_{\max}$, to maintain biologically meaningful interaction strengths [77]–[79]. The magnitude $|w_{ij}|$ reflects the strength of regulation, with larger absolute values corresponding to stronger activating or repressing effects. We exclude the self-interaction links, as they correspond to intrinsic gene dynamics rather than inter-gene regulation. We provide additional details on the construction of the GRN Hamiltonian in the Methods section.

2. Initial State Preparation and Pseudotime Evolution: The QHGM begins by initializing the system in a separable state

$$|\psi_0\rangle := \bigotimes_{i=1}^n |\psi_0^{(i)}\rangle, \quad \text{where} \quad |\psi_0^{(i)}\rangle = \cos \theta_i |0\rangle + e^{i\phi_i} \sin \theta_i |1\rangle. \quad (4)$$

Each qubit-state $|\psi_0^{(i)}\rangle$ represents the transcriptional state of g_i as a point on the Bloch sphere, where $\sin^2 \theta_i$ and $\cos^2 \theta_i$ denote the prior probabilities of g_i being expressed or unexpressed, respectively. The angle ϕ_i encode its initial directional or kinetic phase information [80]. This initialization reflects an assumption that genes exist independently without correlations, with correlations emerging dynamically through the regulatory interactions encoded in the Hamiltonian. The system then evolves following the Schrödinger equation $d|\psi_t\rangle/dt = -iH(\mathbf{w})|\psi_t\rangle$, with the time-independent Hamiltonian $H(\mathbf{w})$, yielding a final state $|\psi_t(\mathbf{w})\rangle = \exp\{-itH(\mathbf{w})\}|\psi_0\rangle$, where t represents the pseudotime, which corresponds to the temporal progression of cell-state transition. Pseudotime is the approximate position of cells along a trajectory that quantifies the relative progression of the underlying biological process [81].

3. Measurement and Gene Expression Readout: Following pseudotime evolution, each qubit (gene) is measured using a single-qubit IC-POVM $\{\Lambda_m\}_{m=0}^3$ given as

$$\begin{aligned} \Lambda_0 &= \frac{1}{4}(\mathbf{I} + \frac{1}{2}\mathbf{X} + \frac{\sqrt{3}}{2}\mathbf{Z}), & \Lambda_1 &= \frac{1}{4}(\mathbf{I} - \frac{1}{2}\mathbf{X} - \frac{1}{\sqrt{2}}\mathbf{Y} + \frac{1}{2}\mathbf{Z}), \\ \Lambda_2 &= \frac{1}{4}(\mathbf{I} - \frac{1}{2}\mathbf{X} + \frac{1}{\sqrt{2}}\mathbf{Y} - \frac{1}{2}\mathbf{Z}), & \Lambda_3 &= \frac{1}{4}(\mathbf{I} + \frac{1}{2}\mathbf{X} - \frac{\sqrt{3}}{2}\mathbf{Z}). \end{aligned} \quad (5)$$

We provide further details on the construction of IC-POVM for GRN in Methods. The outcomes of the IC-POVM measurement provide a discretized representation of the gene expression at a given pseudotime. For

example, the measurement label for the j -th qubit, denoted by $m^{(j)} \in \{0, 1, 2, 3\}$, represents a discretized expression level of gene g_j : $m^{(i)} = 0$ indicates that gene g_j is not expressed, while $m^{(j)} = 3$ signifies that gene g_j is highly expressed in a cell. The overall measurement outcome vector is denoted as $\mathbf{m} = (m^{(1)}, m^{(2)}, \dots, m^{(n)})$ and spans 4^n possible joint outcomes. The probability distribution over these joint outcomes at pseudotime t is given by $\phi(\mathbf{m}|t, \mathbf{w}) = \langle \psi_t(\mathbf{w}) | \Lambda_{\mathbf{m}} | \psi_t(\mathbf{w}) \rangle$.

Collecting repeated measurement outcomes at each pseudotime $t_i \in \{t_1, \dots, t_{N_t}\}$ yields a discretized gene-expression dataset

$$\mathcal{G} := \{\mathbf{m}_{(i,k)}\}_{i=1, k=1}^{N_t, N_c} \in \{0, 1, 2, 3\}^{N_t \times N_c \times n},$$

which serves as the observable data for inference. Here, N_t denotes the number of pseudotime bins (discrete time points), N_c denotes the number of independently measured cells (measurement outcomes) per bin, and n is the number of genes (qubits) in the network. This concludes the description of QHGM.

Learning regulatory coefficients \mathbf{w} : Building on QHL using empirical risk minimization, we design a variational quantum network inference algorithm (VQ-Net) to learn the weights from the discretized scRNA-seq data collected at multiple pseudotime points. In this algorithm, the normalized scRNA-seq data is first converted into four discrete values. During each iteration, the algorithm minimizes the average negative log-likelihood function across all pseudotime bins. Furthermore, if the priors θ_i and ϕ_i are not available for the initial state preparation, the algorithm jointly learns these parameters alongside \mathbf{w} . Further implementation details are provided in the Methods and summarized in Fig. 2.

C. Numerical Experiments and Results

We evaluate the proposed VQ-Net through numerical experiments on synthetic data generated using QHGM. Moreover, we demonstrate the usage of QHGM on the GBMap scRNA-seq data to infer GRNs with both known and novel regulatory interactions.

Synthetic Data: To evaluate the performance of VQ-Net, we generate synthetic time-resolved measurement data using the QHGM as the ground-truth generative model. We consider a 12-qubit system with 132 randomly chosen weights $w_{ij} \in [-1, 1]$. A detailed description of the simulation setup, including data generation and training, is provided in Methods. Fig. 3 summarizes the empirical tradeoff between the number of times samples N_t and the number of measurement per time sample N_c .

In Fig. 3A, we test different $N_t \in \{5, 15, 25, 35, 45\}$ and $N_c \in \{100, 500, 1000, 1500, 2000\}$ and report the maximum absolute weight error between learned weights and true weights ($\max_{(i,j)} |w_{ij} - w_{ij}^{\text{true}}| \in [0, 2]$) against training epochs. For $N_t = 5$, the error diverges and eventually saturates near the maximum error of 2 for all values of N_c . This suggests potential issues with insufficient empirical identifiability due to fewer time samples. In contrast, when N_t exceeds 15, the error decreases monotonically and converges towards

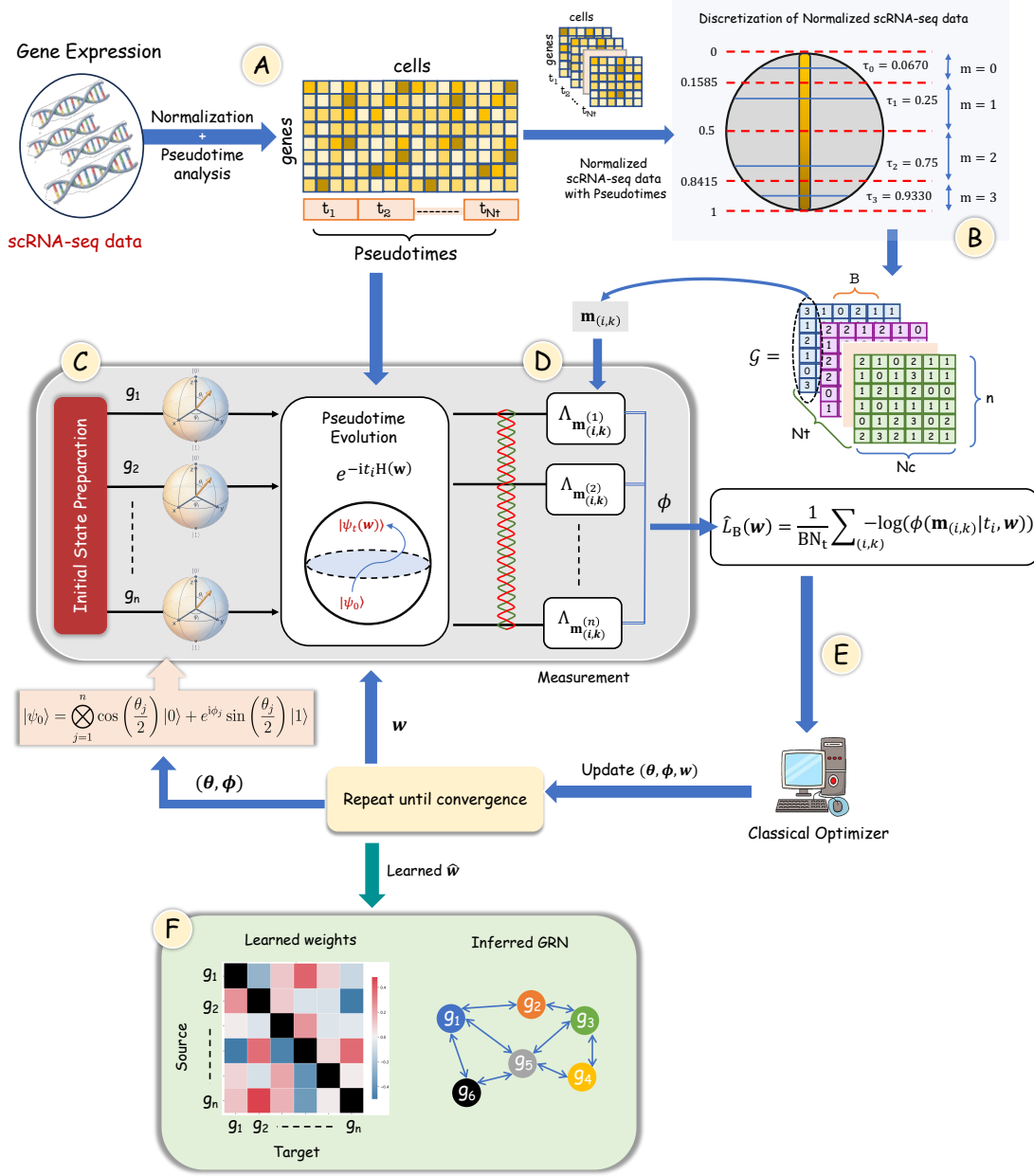


Figure 2: VQ-Net. (A) Raw scRNA-seq data are preprocessed, normalized, and assigned pseudotime values, providing a temporal ordering of cells along a developmental trajectory. (B) The normalized pseudotime-ordered scRNA-seq data are converted into four discrete values, denoted as \mathcal{G} , where N_t denotes the number of pseudotime bins, N_c denotes the number of independently measured cells per bin, and n is the number of genes in the network. (C) Prepares a separable initial state and evolves under the parameterized Hamiltonian $H(\mathbf{w}) = \sum_{(i,j)} w_{ij} \frac{1}{2} (I - Z_i) \otimes Y_j$, which encodes directed regulatory interactions. (D) For each pseudotime bin t_i , the single-qubit IC-POVM is applied as measurement observables on entangled evolved states conditioned on the discretized scRNA-seq data $\mathbf{m}_{(i,k)}$ as input. Here, k is the index of the cell in the corresponding pseudotime bin. (E) The parameters $(\theta, \phi, \mathbf{w})$ are optimized by minimizing the mini-batch empirical loss using a classical optimizer. (F) The learned weights \mathbf{w} are visualized as a signed, asymmetric weight matrix, from which the GRN is inferred.

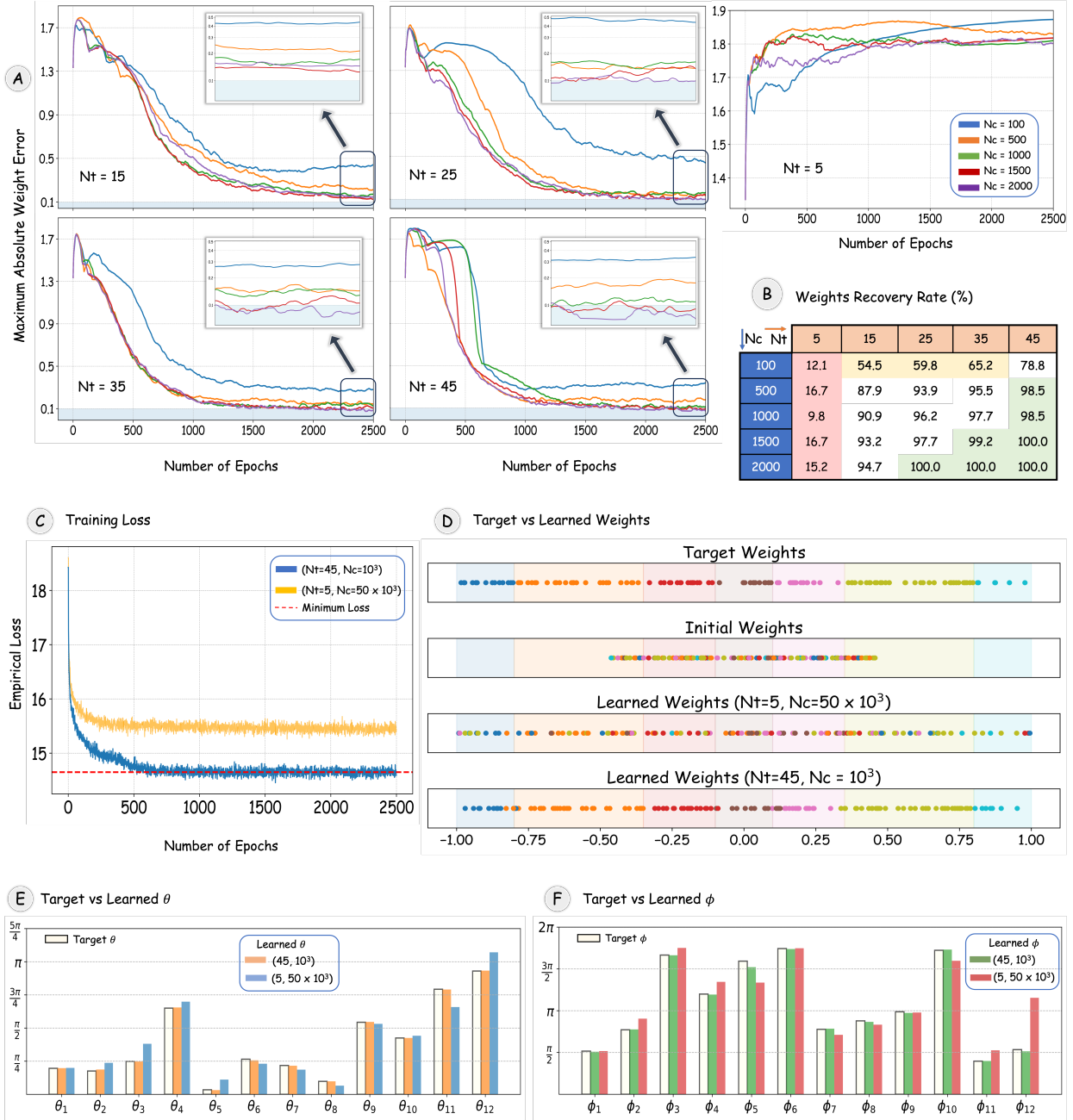


Figure 3: Performance of VQ-Net on the synthetic data generated using QHGM. **(A)** Maximum absolute weight error versus epochs for different numbers of sampled times N_t and measurements per time N_c . **(B)** Percentage of recovered weights within 10% error, illustrating the tradeoff between empirical identifiability (controlled by N_t) and sampling variance (controlled by N_c). **(C)** Batch empirical loss during training is computed using a mini-batch of size 20 and 200 for $N_t = 45$ and 5, respectively. The results indicate convergence to the theoretical optimum for $N_t = 45$. **(D)** Learned weights compared to ground truth, demonstrating strong recovery for $N_t = 45$ and dispersion for $N_t = 5$. **(E–F)** Recovered initial-state parameters (θ, ϕ) with relative errors of (0.0098, 0.0194) for $(N_t, N_c) = (45, 10^3)$ and (0.1638, 0.180) for $(N_t, N_c) = (5, 50 \times 10^3)$, respectively.

zero. Additionally, more stable convergence and reduced error are observed as N_c increases. In Fig. 3B, we report the percentage of recovered weights within a tolerance of 0.1 (i.e., less than 10% maximum absolute error). For all N_t greater than 5, the recovery rate improves monotonically as N_c increases. However, when the number of measurements per time is small ($N_c = 100$), we observe a sharp degradation in performance, up to a 30% drop in recovery rate (highlighted in yellow), relative to $N_c > 100$. The sudden decrease can be attributed to high sample variance at low N_c , which results in noisy empirical estimates of the true likelihood function, even when there are enough time samples. In this scenario, the optimizer is significantly influenced by sampling noise rather than structural information, causing many weights to exceed the 0.1 tolerance level. For $N_t = 5$, the recovery rate decreases significantly, by as much as 80% compared to larger values of N_t (highlighted in red). This decline is likely due to parameter indistinguishability when the number of sampled time points is small. Specifically, multiple distinct weight configurations produce nearly identical measurement statistics across the observed times, resulting in a drop in weight recovery accuracy that does not reliably improve even with increasing N_c . For example, the relative error, defined as $\|\mathbf{w}^{\text{learned}} - \mathbf{w}^{\text{true}}\|/\mathbf{w}^{\text{true}}$, for $(N_t, N_c) = (5, 50 \times 10^3)$ is 1.0055, whereas it is 1.251 for $(N_t, N_c) = (5, 10^2)$.

Fig. 3C shows the batch empirical loss, computed as the average negative log-likelihood over a mini-batch, versus training epochs. In this figure, $(N_t, N_c) = (45, 10^3)$ (blue) converges to the theoretical minimum (dashed line), which corresponds to the expected negative log-likelihood loss averaged over the sampled times. In contrast, $(N_t, N_c) = (5, 50 \times 10^3)$ (yellow) remains trapped above the optimum. The learned weights (color-coded by target bins) corresponding to these two cases are shown in Fig. 3D. For $N_t = 45$, the learned weights cluster tightly around their true values. For $N_t = 5$, the learned weights remain dispersed despite receiving the same initialization. Finally, in Fig. 3E and F, we inspect the reconstructed initial-state parameters (θ, ϕ) . For $(45, 10^3)$, the relative errors for θ and ϕ are 0.0098 and 0.0194, respectively. Interestingly, even when the weights are not accurately estimated at $(5, 50 \times 10^3)$, the initial-state parameters are learned with a lower error of 0.1638 for θ and 0.180 for ϕ . This indicates that VQ-Net can simultaneously infer both the weights and the initial state, and the estimation of initial-state parameters is comparatively more robust to changes in N_t and N_c than the recovery of weights. These observations align closely with our theoretical analysis: the indistinguishability of the parameters is governed by the number of times sampled N_t , while the sampling variance of the empirical loss is controlled by the number of measurements per time N_c . Therefore, simply increasing N_t or N_c on its own is not enough to drive the weight estimation error to zero. To achieve consistent recovery, it is necessary to have both a sufficient number of time samples and a sufficient number of measurements at each time point.

GBMap scRNA-seq data: We implemented the VQ-Net to build QHGM using the core GBmap scRNA-seq data comprising 16 independent studies and 109 patients, post standardization and batch normalization

[73]. We focused on Differentiated-like and Stem-like cells in the annotation level 2 classification, yielding approximately 127,000 cells in total. At annotation level 3, these cells were further classified as Astrocyte-like (AC-like) (50,847), Mesenchymal-like (MES-like) (33,167), Neural Progenitor Cell-like (NPC-like) (22,117), and Oligodendrocyte Progenitor Cell-like (OPC-like) (21,390). Pseudotime is inferred using the VIA algorithm [72], with an OPC-like cell as the root representing the putative progenitor state and AC-like and MES-like cells as terminal endpoints (see Fig. 4A). Cells are embedded in UMAP space based on the 5,000 most variable genes, and a streamplot is overlaid on the embedding to visualize the dominant probabilistic flow along pseudotime. Higher pseudotime values correspond to more differentiated states, and the trajectory highlights branching points and intermediate transitional states along the differentiation continuum. To examine the gene regulatory dynamics along this trajectory, we considered a set of 14 genes: *BCAN*, *STMN1*, *HES6*, *ETV1*, *CADM2*, *MMP16*, *CKB*, *LIMA1*, *VCAN*, *JPT1*, *ASCL1*, *CDK4*, *TUBB2B*, and *NCAM1*. A detailed description of the data preparation and training details is provided in Methods. The learned weights are shown in Fig. 4B, which illustrates the median learned weights across independent training instances. To quantify interaction selectivity, we computed the coefficient of variation (CV), defined as the ratio of the standard deviation to the absolute value of the mean, separately for positive and negative learned weights (Fig. 4C). A high CV indicates selective regulation, in which a gene strongly influences only a subset of the gene set, whereas a low CV reflects broad and more uniform regulatory influence across the gene set. Fig. 4D shows the inferred GRN, consisting of the strongest regulatory interactions, defined by row-wise selection of the top 15th percentile of positive and negative weights.

To validate the accuracy of these inferred interactions, we compared the weights learned via VQ-Net against known regulatory pairs reported in the literature. As seen in Fig. 4D, QHGM correctly identifies *ASCL1*'s broad regulatory influence and recovers strong interactions with targets such as *BCAN*, *CDK4*, and *CKB*, confirming its established role in driving GBM heterogeneity [82]. Nodes like *STMN1*, integrate various regulatory inputs that have opposing effects. This is consistent with the known sensitivity of microtubule dynamics and cell cycle regulators to competing upstream signals [83]. The cyclin-dependent kinase axis, particularly *CDK4/6*, is well-established as a driver of GBM cell proliferation and cell-cycle progression, with inhibition altering subtype programs in proneural stem-like cells supporting dynamic reprogramming under perturbation [84] [85]. Proliferation-associated genes (*CDK4*, *STMN1*, *TUBB2B*) are coupled to extracellular matrix (ECM) and cell-adhesion components (*BCAN*, *VCAN*, *NCAM1*, *MMP16*). This aligns with the literature on ECM proteoglycans (e.g., versican/*VCAN*), which promotes glioma proliferation and invasion [86], and adhesion molecules that mediate GBM cell migration in a context-dependent manner [87]. Beyond the central hub structure, the model captures specific pairwise regulatory dynamics that are well supported by functional biology studies. Also, QHGM recovers biologically meaningful feedback regulatory

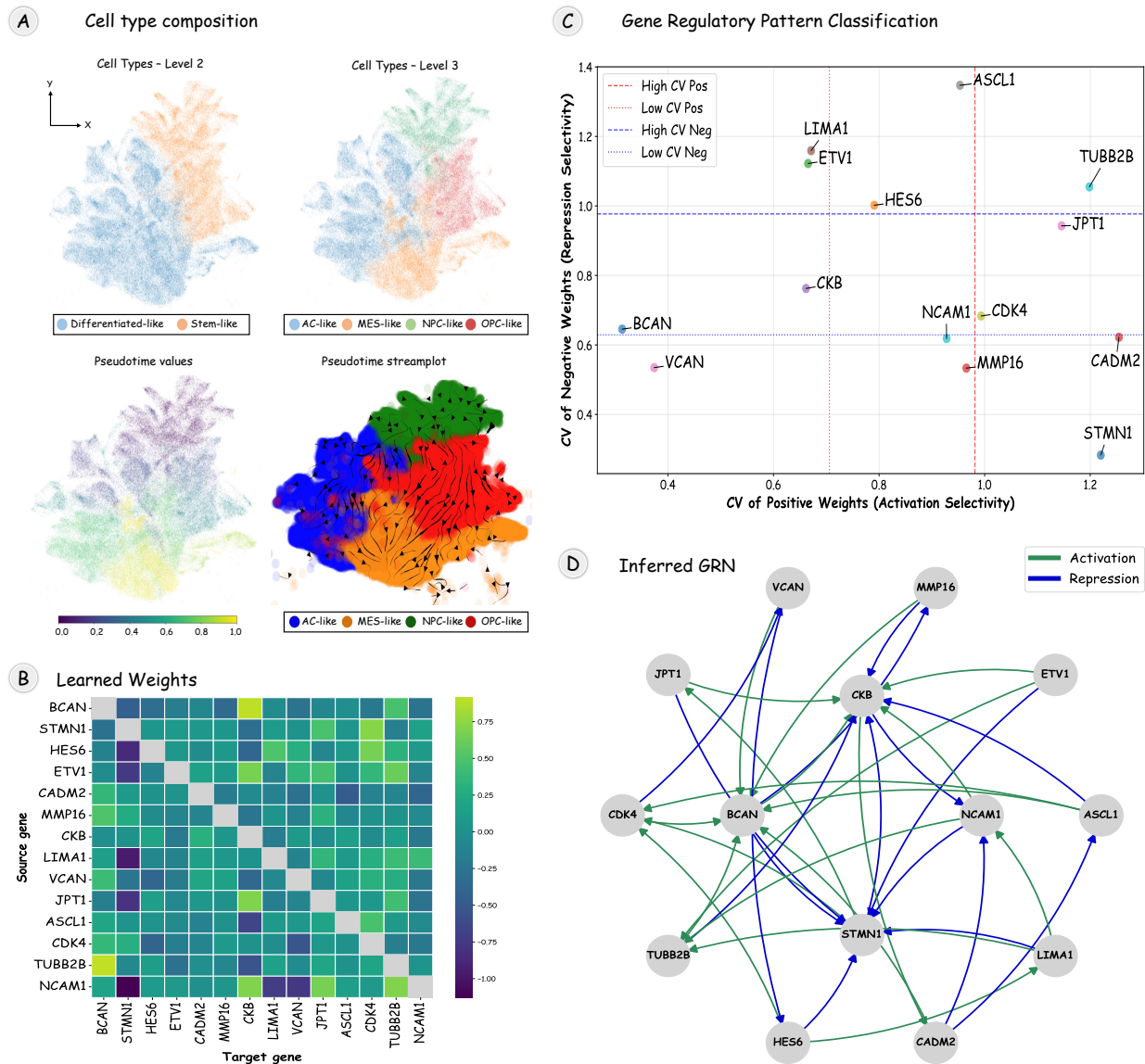


Figure 4: Inferred GRN from QHGM on GMap scRNA-seq data. **(A)** Cells are shown at increasing annotation granularity (Level 2 and Level 3) at UMAP coordinates. The trajectory inference is set with an OPC-like cell as the root node and progresses toward AC-like and MES-like cell types specified as terminal endpoints. The streamplot overlaid on the UMAP embedding visualizes this progression, showing the dominant probabilistic flow of cells along pseudotime, where higher pseudotime values correspond to more differentiated states. **(B)** Heatmap of median learned weights across 10 simulations, which summarizes central tendencies across simulations. **(C)** Gene-wise classification of regulatory behavior based on the coefficient of variation (CV) of positive and negative weights across simulations. The joint CV analysis distinguishes genes with selective, stable activation or repression from those exhibiting high variability, providing a quantitative measure of regulatory consistency and context dependence. **(D)** GRN is inferred from the learned weights by selecting the top 15th percentile of positive (activation) and negative (repression) Hamiltonian weights separately, visualized as a directed network. Green and blue edges denote activating and repressing interactions, respectively.

loops. Notably, the model identifies a positive association between **VCAN** and **BCAN**. This finding aligns with analyses comparing high versus low **VCAN** expression groups, where increased **VCAN** levels were accompanied by upregulation of **BCAN** [86]. These results suggest that our *quantum-like* model demonstrates high precision in recovering interactions.

Overall, QHGM reveals extensive feedback loops and context-dependent sign switching, particularly involving lineage regulators such as **ASCL1**, which has been implicated in multiple biological contexts, such as proneural transcriptional programs [88] and the neural stem cell-like features of glioma stem cells [89]. Such context dependency indicates that regulatory effects are not fixed, instead vary with the global state of the cell, consistent with the heterogeneity observed in GBM stem-like populations and dynamic state transitions [90]. Moreover, the order and combination of regulatory events, such as lineage specification versus microenvironmental engagement, can yield distinct downstream outcomes, supporting the notion that OPC-like GBM cells occupy a continuum of regulatory states rather than discrete phenotypes. The inferred GRN reveals that OPC-like GBM states are governed by a densely interconnected regulatory architecture rather than by linear or modular signaling pathways. Collectively, these results suggest that regulatory information in OPC-like cells propagates through interfering, context-dependent, and non-separable pathways, producing dynamic cellular states that are not adequately captured by classical additive or modular gene regulatory models.

III. DISCUSSION

In this work, we introduce a framework for Hamiltonian learning based on time-resolved measurement outcomes from a fixed local IC-POVM, and the system evolves from a fixed initial state. We evaluate the QHL problem from a non-asymptotic perspective, deriving sample complexity bounds that scale polynomially with the number of qudits. Our approach first establishes the strong convexity of the empirical loss with high probability, which allows for a rigorous error bound between the empirical minimizer and the true parameters \mathbf{w}^* . Furthermore, using Rademacher complexity arguments, we obtain a high-probability, finite-sample uniform convergence guarantee for the empirical loss. The resulting bound identifies the contributions of two distinct stochastic sources: a $N_t^{-1/2}$ term arising from the time sampling and a $N_c^{-1/2}$ term arising from the finite number of measurement outcomes collected at each time point. Although these terms provide a baseline for convergence, tighter error bounds can be found by exploiting the local structure of the loss. For example, through local Rademacher complexity [91], one can potentially achieve faster rates of order $\mathcal{O}(1/N_t)$ and $\mathcal{O}(1/N_c)$. A promising direction is developing a learning algorithm that achieves Heisenberg-scaling error bounds in the fixed-measurement-model setting. Another natural next step is to move beyond closed-system dynamics and investigate open-system evolution, where learning non-unitary generators introduces new questions around identifiability and sample complexity.

Having established the theoretical guarantees of QHL, we next apply it to GRN inference. In contrast to quantum circuit-based approaches [66], our Hamiltonian formulation is agnostic to gene ordering, and the computational complexity of VQ-Net scales polynomially with the number of genes, making it suitable for large GRNs. From a modeling perspective, the QHGM provides a *quantum-like* representation of biological regulation: regulatory interactions correspond to coupling terms in the Hamiltonian and pseudotime play the role of a physical evolution time. This viewpoint may offer deeper insight into biological networks that exhibit non-classical statistical features such as interference and contextuality [59], [60], which are challenging to capture with classical graphical models. A practical advantage of the Hamiltonian formulation is extensibility and expressivity. The QHL framework can incorporate multi-omics data (gene expression [92], chromatin accessibility [93], transcription factor binding [94], epigenetics [95], etc.) by adding corresponding terms to the Hamiltonian or introducing multiple measurements. Higher-order regulatory interactions can be represented via hypergraph-inspired Hamiltonians (e.g., k -local terms for $k > 2$), enabling models that go beyond pairwise interactions [96]. Further, avenues to incorporate additional ancillas corresponding to external factors (other genes, environmental factors), such as open system characterizations, may also be worth looking at. All of these directions provide a structured conceptual path toward integrating multi-scale biological mechanisms and exogenous terms within a unified inference framework.

Beyond genomics, this Hamiltonian perspective suggests potential applications in other networked systems. A compelling direction is modeling mind–body interactions using time-series data from IoT wearables (e.g., heart-rate variability, stress markers, behavioral signals), as well as in evolving social systems. Such data exhibit contextuality and interference-like effects that violate classical Markov assumptions, suggesting that *quantum-like* models may reveal underlying information structures in human physiology and social behavior, analogous to *quantum-like* dependencies in GRNs. Finally, although we demonstrate the usage of the QHL framework on GRN inference, the methodology is not specific to genomics. This can be extended to quantum many-body learning problems, and other *quantum-like* systems, such as social and economic networks, where contextual or non-classical probabilistic effects may arise.

IV. METHODS

In this section, we present the proof of Theorems 1 and 2 and outline the technical details of QHGM, VQ-Net, and the training details of our numerical results. We begin by introducing the necessary preliminaries used in the proofs. We then describe the construction of the parameterized Hamiltonian used to model GRNs (Eq. (3)), followed by the construction of the IC-POVM measurements employed in our framework (see Eq. (5)). Next, we will provide the details of the VQ-Net algorithm. Finally, we will outline the data generation and training details used in our numerical results.

A. Preliminaries

Let $\mathcal{H} := \mathbb{C}^D$ denote the D -dimensional Hilbert space, which serves as the configuration space for quantum states. For the rest of the paper, $\|\cdot\|$ denotes the Euclidean norm for vectors and the spectral (or Schatten- ∞) norm for matrices unless otherwise stated. We use $\|\cdot\|_p$ to denote Schatten p -norm for matrices for $p \in [1, \infty)$.

Definition 2 (IC-POVM [97]). *An IC-POVM $\Lambda := \{\Lambda_{\mathbf{m}}\}_{\mathbf{m} \in \mathcal{M}}$ is a finite collection of positive semidefinite operators that sum to the identity, and span the space of Hermitian operators $\text{Herm}(\mathcal{H})$, i.e.,*

$$\Lambda_{\mathbf{m}} \geq 0, \quad \sum_{\mathbf{m} \in \mathcal{M}} \Lambda_{\mathbf{m}} = I, \quad \text{and} \quad \text{span}\{\Lambda_{\mathbf{m}}\}_{\mathbf{m} \in \mathcal{M}} = \text{Herm}(\mathcal{H}).$$

The minimum number of elements required for informational completeness is $M_{\min} = D^2$.

Lemma 1 (Matrix Bernstein-type inequality [98, Corollary 6.2.1]). *Let μ_X be a fixed $d_1 \times d_2$ matrix. Construct a random matrix $X \in \mathbb{C}^{d_1 \times d_2}$ such that $\mathbb{E}X = \mu_X$ and $\|X\| \leq L$. Let*

$$\bar{X}_n := \frac{1}{n} \sum_{k=1}^n X_k,$$

where $\{R_k\}_{k=1}^n$ are independent copies of R . Then, for all $t \geq 0$,

$$\Pr \left\{ \|\bar{X}_n - \mu_X\| \geq t \right\} \leq (d_1 + d_2) \exp\left(-\frac{nt^2/2}{\sigma^2 + 2Lt/3}\right), \quad (6)$$

where σ^2 is the per-sample second moment, defined as $\sigma^2 := \max\{\|\mathbb{E}(XX^\dagger)\|, \|\mathbb{E}(X^\dagger X)\|\}$. In other words, for any $\delta \in (0, 1)$, the following inequality holds:

$$\|\bar{X}_n - \mu_X\| \leq \sqrt{\frac{2\sigma^2}{n} \log\left(\frac{(d_1 + d_2)}{\delta}\right)} + \frac{2L}{3n} \log\left(\frac{(d_1 + d_2)}{\delta}\right). \quad (7)$$

with probability at least $(1 - \delta)$.

Lemma 2. *Consider a finite sequence $\{\Lambda_k\}$ of fixed $D \times D$ Hermitian matrices, and let $\{\sigma_i\}$ be i.i.d. Rademacher random variables. Then the following inequality holds:*

$$\mathbb{E}_\sigma \left\| \sum_k \sigma_k \Lambda_k \right\| \leq \sqrt{2 \log(2D)} \left\| \sum_k \Lambda_k^2 \right\|^{1/2}.$$

Proof. The proof is provided in Appendix C. □

Lemma 3. *Consider a time-independent Hamiltonian $H(\mathbf{w}) = \sum_{k=1}^c w_k H_k$. Let $U_t(\mathbf{w}) = e^{-itH(\mathbf{w})}$ and assume the system starts in the state ρ_0 . For an observable $\Lambda_{\mathbf{m}}$ satisfying $\|\Lambda_{\mathbf{m}}\| \leq 1$, define $\phi(\mathbf{m}|t, \mathbf{w}) := \text{tr}(\Lambda_{\mathbf{m}} \rho_t(\mathbf{w}))$. Then, for every $\mathbf{m} \in \mathcal{M}^n$ and $t \in (0, t_{\max}]$, the following statements hold.*

(i) *The likelihood function $\phi(\mathbf{m}|t, \mathbf{w})$ is twice differentiable in \mathcal{W}_B . The first-order partial derivative with respect to the parameter w_k is given by*

$$\frac{\partial}{\partial w_k} \text{tr}(\Lambda_{\mathbf{m}} \rho_t(\mathbf{w})) = -i \int_0^t \text{tr}\left(\Lambda_{\mathbf{m}}(s) [H_k(s), \rho_0]\right) ds. \quad (8)$$

Moreover, the second-order partial derivative with respect to parameters w_j and w_k is given by

$$\begin{aligned} \frac{\partial^2}{\partial w_j \partial w_k} \text{tr}(\Lambda_{\mathbf{m}} \rho_t(\mathbf{w})) &= - \int_0^t \int_0^{s_1} \text{tr} \left(\Lambda_{\mathbf{m}}(t) [\mathbf{H}_j(s_1), [\mathbf{H}_k(s_2), \rho_0]] \right) ds_2 ds_1 \\ &\quad - \int_0^t \int_0^{s_1} \text{tr} \left(\Lambda_{\mathbf{m}}(t) [\mathbf{H}_k(s_1), [\mathbf{H}_j(s_2), \rho_0]] \right) ds_2 ds_1, \end{aligned} \quad (9)$$

where $\Lambda_{\mathbf{m}}(t) := U_t^\dagger(\mathbf{w}) \Lambda_{\mathbf{m}} U_t(\mathbf{w})$, and $\mathbf{H}_k(s) := U_s^\dagger(\mathbf{w}) \mathbf{H}_k U_s(\mathbf{w})$.

(ii) *Bounded gradient and hessian.*

– For all $\mathbf{w} \in \mathcal{W}_B$, $\|\nabla_{\mathbf{w}} \phi(\mathbf{m}|t, \mathbf{w})\| \leq L_\phi$ and $\|\nabla_{\mathbf{w}}^2 \phi(\mathbf{m}|t, \mathbf{w})\| \leq L_\phi^2$.

(iii) *Lipschitz continuity.* For all $\mathbf{w}, \mathbf{w}' \in \mathcal{W}_B$,

– $|\phi(\mathbf{m}|t, \mathbf{w}) - \phi(\mathbf{m}|t, \mathbf{w}')| \leq L_\phi \|\mathbf{w} - \mathbf{w}'\|$
– $\|\nabla_{\mathbf{w}} \phi(\mathbf{m}|t, \mathbf{w}) - \nabla_{\mathbf{w}} \phi(\mathbf{m}|t, \mathbf{w}')\| \leq L_\phi^2 \|\mathbf{w} - \mathbf{w}'\|$
– $\|\nabla_{\mathbf{w}}^2 \phi(\mathbf{m}|t, \mathbf{w}) - \nabla_{\mathbf{w}}^2 \phi(\mathbf{m}|t, \mathbf{w}')\| \leq 2L_\phi^3 \|\mathbf{w} - \mathbf{w}'\|$,

where $L_\phi := 2t_{\max} \sqrt{c} \|\mathbf{H}\|_{\infty, \max}$.

Proof. The proof is provided in Appendix D. □

B. Proof of Theorem 1

Proof Outline: The proof establishes a finite-sample error bound between $\hat{\mathbf{w}}$ and \mathbf{w}^* by first showing that the empirical loss inherits the strong convexity of the expected loss with high probability. The proof begins by observing that the complete set of measurement outcomes $\{\mathbf{m}_{(i,k)}\}_{i=1, k=1}^{\mathbf{N}_t, \mathbf{N}_c}$ is jointly independent but not identically distributed. However, for each time index i , outcomes are independent and identically distributed. This structure motivates decomposing the difference between the empirical and expected Hessian into two terms, first measuring deviation within the conditional samples $\{\mathbf{m}_{(i,k)}\}_{k=1}^{\mathbf{N}_c}$ for each time index i , and the second term measuring deviation across the time. By applying the matrix Bernstein inequality (Lemma 1) to both terms in this decomposition, we show that the empirical Hessian concentrates near its expectation pointwise for each $\mathbf{w} \in \mathcal{W}_B$ with high probability. We then employ a covering argument [76, Chapter 5] to extend this concentration uniformly over \mathcal{W}_B . By applying Weyl's inequality [76, Equation 8.9] and invoking assumption A(i), we establish the empirical strong convexity of the loss, ensuring a unique empirical minimizer $\hat{\mathbf{w}}$ with high probability. However, even \hat{L} has a unique minimizer, $\hat{\mathbf{w}}$ can still be distant from \mathbf{w}^* . Therefore, under the high-probability event of empirical strong convexity, we bound the distance $\|\hat{\mathbf{w}} - \mathbf{w}^*\|_2$ by the norm of the gradient of the empirical loss at the true parameter, $\|\nabla \hat{L}(\mathbf{w}^*)\|$. Using Lemma 1 again, we bound this gradient norm, which in turn provides a finite-sample bound that vanishes as $\mathbf{N}_t, \mathbf{N}_c \rightarrow \infty$, ensuring that the unique empirical minimizer concentrates around \mathbf{w}^* .

Let $\widehat{H}(\mathbf{w}) := \nabla^2 \widehat{L}(\mathbf{w})$ denote the Hessian of the empirical loss. We begin the proof by introducing the following definitions: $\widehat{H}_{(i,k)}(\mathbf{w}) := -\nabla_{\mathbf{w}}^2 \log(\phi(\mathbf{m}_{(i,k)}|t_i, \mathbf{w}))$ and $\bar{H}_{t_i}(\mathbf{w}) := \mathbb{E}_{\phi(\cdot|t_i, \mathbf{w}^*)}[-\nabla_{\mathbf{w}}^2 \log(\phi(\mathbf{m}|t_i, \mathbf{w}))]$. Next, consider the following inequalities:

$$\begin{aligned} \|\widehat{H}(\mathbf{w}) - \bar{H}(\mathbf{w})\| &\leq \left\| \widehat{H}(\mathbf{w}) - \frac{1}{N_t} \sum_{i=1}^{N_t} \bar{H}_{t_i}(\mathbf{w}) \right\| + \left\| \frac{1}{N_t} \sum_{i=1}^{N_t} \bar{H}_{t_i}(\mathbf{w}) - \bar{H}(\mathbf{w}) \right\| \\ &\leq \frac{1}{N_t} \sum_{i=1}^{N_t} \left\| \frac{1}{N_c} \sum_{k=1}^{N_c} \widehat{H}_{(i,k)}(\mathbf{w}) - \bar{H}_{t_i}(\mathbf{w}) \right\| + \left\| \frac{1}{N_t} \sum_{i=1}^{N_t} \bar{H}_{t_i}(\mathbf{w}) - \bar{H}(\mathbf{w}) \right\| \leq T_1 + T_2, \end{aligned}$$

where $T_1 := \max_i \left\| \frac{1}{N_c} \sum_{k=1}^{N_c} \widehat{H}_{(i,k)}(\mathbf{w}) - \bar{H}_{t_i}(\mathbf{w}) \right\|$ and $T_2 := \left\| \frac{1}{N_t} \sum_{i=1}^{N_t} \bar{H}_{t_i}(\mathbf{w}) - \bar{H}(\mathbf{w}) \right\|$. Note by using Jensen's inequality and Lemma 3, we establish a bound on $\|\widehat{H}_{(i,k)}(\mathbf{w})\|$ and $\|\bar{H}_{t_i}(\mathbf{w})\|$ for a given time t_i . For every $\mathbf{m} \in \mathcal{M}^n$, $\mathbf{w} \in \mathcal{W}_B$, and $t \in (0, t_{\max}]$, we have

$$\|-\nabla_{\mathbf{w}}^2 \log(\phi(\mathbf{m}|t, \mathbf{w}))\| \leq 2(L_\phi/p_{\min})^2 \quad \text{and} \quad \|\bar{H}_t(\mathbf{w})\| \leq 2(L_\phi/p_{\min})^2, \quad (10)$$

where $L_\phi = 2t_{\max}\sqrt{c}\|H\|_{\infty, \max}$. The proof is provided in Appendix E. Next, we bound the terms T_1 and T_2 using the following proposition.

Proposition 1. *For each $\mathbf{w} \in \mathcal{W}_B$, and for all $\varepsilon_1, \varepsilon_2 \geq 0$, the following inequality holds:*

$$\text{(Within-time concentration.)} \quad \Pr\{T_1 \geq \varepsilon_1\} \leq 2c N_t \exp \left\{ -\frac{N_c \varepsilon_1^2/2}{\sigma^2 + 4\varepsilon_1(L_\phi/p_{\min})^2/3} \right\}, \quad (11)$$

$$\text{(Across-time concentration.)} \quad \Pr\{T_2 \geq \varepsilon_2\} \leq 2c \exp \left\{ -\frac{N_t \varepsilon_2^2/2}{\sigma^2 + 4\varepsilon_2(L_\phi/p_{\min})^2/3} \right\}, \quad (12)$$

where $\sigma^2 := 4(L_\phi/p_{\min})^4$.

The proof can be found in Appendix F. Finally, combining the bounds on T_1 (11) and T_2 (12), and letting $\varepsilon_1 = \varepsilon_2 = \varepsilon\mu_0/2$, we conclude that for each $\mathbf{w} \in \mathcal{W}_B$, and for all $\varepsilon > 0$,

$$\begin{aligned} \Pr\{\|\widehat{H}(\mathbf{w}) - \bar{H}(\mathbf{w})\| \geq \varepsilon\mu_0\} &\leq \Pr\{T_1 \geq \varepsilon\mu_0/2\} + \Pr\{T_2 \geq \varepsilon\mu_0/2\} \\ &\leq 2c \left(N_t \exp \left\{ \frac{-N_c \mu_0^2 \varepsilon^2/8}{\sigma^2 + 2\varepsilon\mu_0(L_\phi/p_{\min})^2/3} \right\} + \exp \left\{ \frac{-N_t \mu_0^2 \varepsilon^2/8}{\sigma^2 + 2\varepsilon\mu_0(L_\phi/p_{\min})^2/3} \right\} \right). \end{aligned} \quad (13)$$

We now extend the pointwise bound to hold uniformly over \mathcal{W}_B . To this end, we first establish the Lipschitz continuity of \widehat{H} and \bar{H} . The proof is provided in Appendix G.

Proposition 2. *For every $\mathbf{m} \in \mathcal{M}^n$ and $t \in (0, t_{\max}]$, both the expected Hessian and the empirical Hessian are Lipschitz continuous.*

$$\|\widehat{H}(\mathbf{w}) - \widehat{H}(\mathbf{w}')\| \leq 7(L_\phi/p_{\min})^3 \|\mathbf{w} - \mathbf{w}'\| \quad \text{and} \quad \|\bar{H}(\mathbf{w}) - \bar{H}(\mathbf{w}')\| \leq 7(L_\phi/p_{\min})^3 \|\mathbf{w} - \mathbf{w}'\|,$$

for each $\mathbf{w}, \mathbf{w}' \in \mathcal{W}_B$.

Fix $\eta > 0$, to be specified later. To control the supremum over \mathcal{W}_B , we cover \mathcal{W}_B with an η -net. That is, there exists a finite set $\mathcal{N}_\eta \subset \mathcal{W}_B$ such that for every $\mathbf{w} \in \mathcal{W}_B$, there exists $\mathbf{w}' \in \mathcal{N}_\eta$ with $\|\mathbf{w} - \mathbf{w}'\|_2 \leq \eta$. The cardinality of such a net can be bounded as $N_\eta := |\mathcal{N}_\eta| \leq (\frac{3B}{\eta})^c$, where the inequality follows from the standard bound on the covering number of a c -dimensional Euclidean ball [76, Chapter 5]. Let $\mathcal{N}_\eta := \{\mathbf{w}_1, \mathbf{w}_2, \dots, \mathbf{w}_{N_\eta}\}$ be an η -net points of \mathcal{W}_B . Now, fix any $\mathbf{w} \in \mathcal{W}_B$, and let \mathbf{w}_k be its closest η -net point. Then, using Proposition 2, we obtain

$$\begin{aligned} \|\widehat{H}(\mathbf{w}) - \bar{H}(\mathbf{w})\| &\leq \|\widehat{H}(\mathbf{w}) - \widehat{H}(\mathbf{w}_k)\| + \|\widehat{H}(\mathbf{w}_k) - \bar{H}(\mathbf{w}_k)\| + \|\bar{H}(\mathbf{w}_k) - \bar{H}(\mathbf{w})\| \\ &\leq \|\widehat{H}(\mathbf{w}_k) - \bar{H}(\mathbf{w}_k)\| + 14(L_\phi/p_{\min})^3 \|\mathbf{w} - \mathbf{w}_k\|. \end{aligned}$$

Thus, $\sup_{\mathbf{w} \in \mathcal{W}_B} \|\widehat{H}(\mathbf{w}) - \bar{H}(\mathbf{w})\| \leq \max_{k \in \{1, \dots, N_\eta\}} \|\widehat{H}(\mathbf{w}_k) - \bar{H}(\mathbf{w}_k)\| + 14\eta(L_\phi/p_{\min})^3$. Next, using (13) and union bound over the finite η -net, we obtain, for all $\varepsilon > 0$

$$\begin{aligned} &\Pr\{\max_{k \in \{1, \dots, N_\eta\}} \|\widehat{H}(\mathbf{w}_k) - \bar{H}(\mathbf{w}_k)\| \geq \varepsilon\mu_0\} \\ &= \Pr\left\{\bigcup_{k \in \{1, \dots, N_\eta\}} \{\|\widehat{H}(\mathbf{w}_k) - \bar{H}(\mathbf{w}_k)\| \geq \varepsilon\mu_0\}\right\} \\ &\leq 2c N_\eta \left(N_t \exp\left\{\frac{-N_c \mu_0^2 \varepsilon^2/8}{\sigma^2 + 2\varepsilon\mu_0(L_\phi/p_{\min})^2/3}\right\} + \exp\left\{\frac{-N_t \mu_0^2 \varepsilon^2/8}{\sigma^2 + \varepsilon\mu_0(L_\phi/p_{\min})^2/3}\right\} \right). \end{aligned} \quad (14)$$

Therefore, after setting $\eta = \varepsilon\mu_0/(14(L_\phi/p_{\min})^3)$, we get

$$\begin{aligned} &\Pr\left\{\sup_{\mathbf{w} \in \mathcal{W}_B} \|\widehat{H}(\mathbf{w}) - \bar{H}(\mathbf{w})\| \geq 2\varepsilon\mu_0\right\} \\ &\leq \Pr\{\max_{k \in \{1, \dots, N_\eta\}} \|\widehat{H}(\mathbf{w}_k) - \bar{H}(\mathbf{w}_k)\| \geq \varepsilon\mu_0\} \\ &\leq 2c \left(\frac{42B L_\phi^3}{\varepsilon\mu_0 p_{\min}^3}\right)^c \left(N_t \exp\left\{\frac{-N_c \mu_0^2 \varepsilon^2/8}{\sigma^2 + 2\varepsilon\mu_0(L_\phi/p_{\min})^2/3}\right\} + \exp\left\{\frac{-N_t \mu_0^2 \varepsilon^2/8}{\sigma^2 + \varepsilon\mu_0(L_\phi/p_{\min})^2/3}\right\} \right). \end{aligned}$$

Finally, for all $\varepsilon > 0$ and $\delta \in (0, 1/2)$, if we choose

$$\begin{aligned} N_t &= \mathcal{O}\left(\frac{L_\phi^4}{\mu_0^2 p_{\min}^4 \varepsilon^2} \left(c \log\left(\frac{BL_\phi^3}{\mu_0 p_{\min}^3 \varepsilon}\right) + \log\left(\frac{c}{\delta}\right)\right)\right) \\ \text{and } N_c &= \mathcal{O}\left(\frac{L_\phi^4}{\mu_0^2 p_{\min}^4 \varepsilon^2} \left(c \log\left(\frac{BL_\phi^3}{\mu_0 p_{\min}^3 \varepsilon}\right) + \log\left(\frac{cN_t}{\delta}\right)\right)\right), \end{aligned}$$

then, with probability at least $(1 - 2\delta)$, $\sup_{\mathbf{w} \in \mathcal{W}_B} \|\widehat{H}(\mathbf{w}) - \bar{H}(\mathbf{w})\| \leq 2\varepsilon\mu_0$. This establishes uniform convergence of the empirical Hessian over \mathcal{W}_B . Next, we show the empirical strong convexity using Weyl's inequality [76, Equation 8.9]. For each $\mathbf{w} \in \mathcal{W}_B$,

$$|\lambda_{\min}(\widehat{H}(\mathbf{w})) - \lambda_{\min}(\bar{H}(\mathbf{w}))| \leq \|\widehat{H}(\mathbf{w}) - \bar{H}(\mathbf{w})\|.$$

Taking the supremum over $\mathbf{w} \in \mathcal{W}_B$ yields,

$$\sup_{\mathbf{w} \in \mathcal{W}_B} |\lambda_{\min}(\widehat{H}(\mathbf{w})) - \lambda_{\min}(\bar{H}(\mathbf{w}))| \leq \sup_{\mathbf{w} \in \mathcal{W}_B} \|\widehat{H}(\mathbf{w}) - \bar{H}(\mathbf{w})\|.$$

We now use the inequality that for bounded functions $g_1, g_2 : \mathcal{X} \rightarrow \mathbb{R}$, $|\inf_{\mathcal{X}} g_1 - \inf_{\mathcal{X}} g_2| \leq \sup_{\mathcal{X}} |g_1 - g_2|$. Applying this with $g_1(\mathbf{w}) = \lambda_{\min}(\hat{H}(\mathbf{w}))$ and $g_2(\mathbf{w}) = \lambda_{\min}(\bar{H}(\mathbf{w}))$, we obtain

$$\left| \inf_{\mathbf{w} \in \mathcal{W}_B} \lambda_{\min}(\hat{H}(\mathbf{w})) - \inf_{\mathbf{w} \in \mathcal{W}_B} \lambda_{\min}(\bar{H}(\mathbf{w})) \right| \leq \sup_{\mathbf{w} \in \mathcal{W}_B} \|\hat{H}(\mathbf{w}) - \bar{H}(\mathbf{w})\|.$$

Recalling the strong convexity assumption, $\inf_{\mathbf{w} \in \mathcal{W}_B} \lambda_{\min}(\bar{H}(\mathbf{w})) \geq \mu_0$. Therefore, $\inf_{\mathbf{w} \in \mathcal{W}_B} \lambda_{\min}(\hat{H}(\mathbf{w})) \geq (1 - 2\varepsilon)\mu_0$ with probability at least $(1 - 2\delta)$. This completes the first part of Theorem 1.

Next, we derive the finite-sample bound on the parameter error. Define the event

$$\mathcal{E}_{\text{sc}} := \left\{ \inf_{\mathbf{w} \in \mathcal{W}_B} \lambda_{\min}(\hat{H}(\mathbf{w})) \geq (1 - 2\varepsilon)\mu_0 \right\}.$$

On the event \mathcal{E}_{sc} , the empirical loss \hat{L} is $(1 - 2\varepsilon)\mu_0$ -strongly convex over \mathcal{W}_B . Therefore, from the equivalent conditions of strong convexity (see Appendix H), for all $\mathbf{w} \in \mathcal{W}_B$,

$$(1 - 2\varepsilon)\mu_0 \|\mathbf{w}^* - \mathbf{w}\|^2 \leq (\nabla_{\mathbf{w}} \hat{L}(\mathbf{w}^*) - \nabla_{\mathbf{w}} \hat{L}(\mathbf{w}))^\top (\mathbf{w}^* - \mathbf{w}) \leq \|\nabla_{\mathbf{w}} \hat{L}(\mathbf{w}^*) - \nabla_{\mathbf{w}} \hat{L}(\mathbf{w})\| \|\mathbf{w}^* - \mathbf{w}\|, \quad (15)$$

where the second inequality follows from the Cauchy–Schwarz inequality. Since $\hat{\mathbf{w}} \in \text{interior}(\mathcal{W}_B)$ with probability 1, the inequality (15) holds at $\mathbf{w} = \hat{\mathbf{w}}$, yielding

$$(1 - 2\varepsilon)\mu_0 \|\mathbf{w}^* - \hat{\mathbf{w}}\| \leq \|\nabla_{\mathbf{w}} \hat{L}(\mathbf{w}^*) - \nabla_{\mathbf{w}} \hat{L}(\hat{\mathbf{w}})\| = \|\nabla_{\mathbf{w}} \hat{L}(\mathbf{w}^*)\|$$

with probability at least $(1 - 2\delta)$, where the equality follows from the first-order optimality condition $\nabla_{\mathbf{w}} \hat{L}(\hat{\mathbf{w}}) = 0$. Finally, we need to bound the norm of the gradient $\|\nabla_{\mathbf{w}} \hat{L}(\mathbf{w}^*)\|$. To do this, we use Lemma 1 along with the union bound. Consider the following inequalities:

$$\|\nabla_{\mathbf{w}} \hat{L}(\mathbf{w}^*)\| \leq \frac{1}{N_t} \sum_{i=1}^{N_t} \left\| \frac{1}{N_c} \sum_{k=1}^{N_c} \nabla_{\mathbf{w}} \ell(\phi(\mathbf{m}_{(i,k)} | t_i, \mathbf{w}^*)) \right\| \leq \max_{1 \leq i \leq N_t} \left\| \frac{1}{N_c} \sum_{k=1}^{N_c} \nabla_{\mathbf{w}} \ell(\phi(\mathbf{m}_{(i,k)} | t_i, \mathbf{w}^*)) \right\|.$$

Observe that, for a given time t_i , the random vectors $\nabla_{\mathbf{w}} \ell(\phi(\mathbf{m}_{(i,k)} | t_i, \mathbf{w}^*))$ are independent satisfying $\mathbb{E}_{\phi(\cdot | t_i, \mathbf{w}^*)}[\nabla_{\mathbf{w}} \ell(\phi(\mathbf{m}_{(i,k)} | t_i, \mathbf{w}^*))] = 0$, and by Lemma 3, we have $\|\nabla_{\mathbf{w}} \ell(\phi(\mathbf{m}_{(i,k)} | t_i, \mathbf{w}^*))\| \leq (L_\phi/p_{\min})$. Therefore, for any $\delta' \in (0, 1)$, the following inequality holds

$$\|\nabla_{\mathbf{w}} \hat{L}(\mathbf{w}^*)\| \leq \sqrt{\frac{2\tau_{\max}^2}{N_c} \log\left(\frac{(1+c)N_t}{\delta'}\right)} + \frac{2L_\phi}{3p_{\min}N_c} \log\left(\frac{(1+c)N_t}{\delta'}\right),$$

with probability at least $(1 - \delta')$, where $\tau_{\max}^2 := \max_i \tau_i^2$ and

$$\tau_i^2 := \|\mathbb{E}_{\phi(\cdot | t_i, \mathbf{w}^*)}[\nabla_{\mathbf{w}} \ell(\phi(\mathbf{m}_{(i,k)} | t_i, \mathbf{w}^*)) \nabla_{\mathbf{w}} \ell(\phi(\mathbf{m}_{(i,k)} | t_i, \mathbf{w}^*))^\top]\| \leq (L_\phi/p_{\min})^2$$

for all $1 \leq i \leq N_t$. Let $\delta' = \delta$. This gives us the desired error bound. For any $\delta > 0$, the following inequality holds:

$$\Pr\left\{ \mathcal{E}_{\text{sc}} \cap \|\hat{\mathbf{w}} - \mathbf{w}^*\| \leq \frac{(L_\phi/p_{\min})}{(1 - 2\varepsilon)\mu_0} \left(\sqrt{\frac{2}{N_c} \log\left(\frac{(1+c)N_t}{\delta}\right)} + \frac{1}{N_c} \log\left(\frac{(1+c)N_t}{\delta}\right) \right) \right\} \geq (1 - 3\delta), \quad (16)$$

This completes the proof of Theorem 1.

C. Proof of Theorem 2

Proof Outline: Similar to proof of Theorem 1, we first decompose $\sup_{\mathbf{w} \in \mathcal{W}_B} |\widehat{L}(\mathbf{w}) - L(\mathbf{w})|$ into within time and across time components. To control each part, we use the notion of empirical *Rademacher complexity* [76], [99]. Combining these components yields a uniform convergence bound that vanishes in probability as $N_t, N_c \rightarrow \infty$.

To formalize the proof outline above, we define $L_t(\mathbf{w}) := \mathbb{E}_{\mathbf{m} \sim \phi(\cdot|t, \mathbf{w}^*)}[\ell(\phi(\mathbf{m}|t, \mathbf{w}))]$. Note by using Jensen's inequality and Lemma 3, the function $L_t(\mathbf{w})$ is Lipschitz continuous on \mathcal{W}_B with constant L_ϕ/p_{\min} : for any $t \in (0, t_{\max}]$ and any $\mathbf{w}, \mathbf{w}' \in \mathcal{W}_B$,

$$|L_t(\mathbf{w}) - L_t(\mathbf{w}')| \leq \frac{L_\phi}{p_{\min}} \|\mathbf{w} - \mathbf{w}'\|. \quad (17)$$

Consider the following inequalities:

$$\begin{aligned} |\widehat{L}(\mathbf{w}) - L(\mathbf{w})| &= \left| \frac{1}{N_t N_c} \sum_{i=1}^{N_t} \sum_{k=1}^{N_c} \ell(\phi(\mathbf{m}_{(i,k)}|t_i, \mathbf{w})) - L(\mathbf{w}) \right| \\ &\leq \left| \frac{1}{N_t N_c} \sum_{i=1}^{N_t} \sum_{k=1}^{N_c} \ell(\phi(\mathbf{m}_{(i,k)}|t_i, \mathbf{w})) - \frac{1}{N_t} \sum_{i=1}^{N_t} L_{t_i}(\mathbf{w}) \right| + T_2(\mathbf{w}) \leq \frac{1}{N_t} \sum_{i=1}^{N_t} T_1^{(i)}(\mathbf{w}) + T_2(\mathbf{w}) \end{aligned}$$

where

$$T_2(\mathbf{w}) := \left| \frac{1}{N_t} \sum_{i=1}^{N_t} L_{t_i}(\mathbf{w}) - L(\mathbf{w}) \right| \text{ and } T_1^{(i)}(\mathbf{w}) := \left| \frac{1}{N_c} \sum_{k=1}^{N_c} \ell(\phi(\mathbf{m}_{(i,k)}|t_i, \mathbf{w})) - L_{t_i}(\mathbf{w}) \right|.$$

Hence,

$$\sup_{\mathbf{w} \in \mathcal{W}_B} |\widehat{L}(\mathbf{w}) - L(\mathbf{w})| \leq \frac{1}{N_t} \sum_{i=1}^{N_t} \sup_{\mathbf{w} \in \mathcal{W}_B} T_1^{(i)}(\mathbf{w}) + \sup_{\mathbf{w} \in \mathcal{W}_B} T_2(\mathbf{w}) \leq \max_{1 \leq i \leq N_t} \sup_{\mathbf{w} \in \mathcal{W}_B} T_1^{(i)}(\mathbf{w}) + \sup_{\mathbf{w} \in \mathcal{W}_B} T_2(\mathbf{w}).$$

Next, define $\mathcal{S}_i := \{\mathbf{m}_{(i,1)}, \dots, \mathbf{m}_{(i,N_c)}\}$ be the set of measurement outcomes at a time t_i and $\mathcal{T} := \{t_1, \dots, t_{N_t}\}$ be the set of times. We now bound the above terms using McDiarmid's inequality [76, Corollary 2.21] [99, Lemma 26.4]. In particular, for any $\delta_1, \delta_2 > 0$, the following bounds hold:

$$\max_{1 \leq i \leq N_t} \sup_{\mathbf{w} \in \mathcal{W}_B} T_1^{(i)}(\mathbf{w}) \leq \max_i 2 \hat{\mathfrak{R}}_{\mathcal{S}_i}(\mathcal{L}_{\mathbf{m}}^{(i)}) + 3(-\log p_{\min}) \sqrt{\frac{\log(2N_t/\delta_1)}{2N_c}} \quad (18)$$

$$\text{and } \sup_{\mathbf{w} \in \mathcal{W}_B} T_2(\mathbf{w}) \leq 2 \hat{\mathfrak{R}}_{\mathcal{T}}(\mathcal{L}_t) + 3(-\log p_{\min}) \sqrt{\frac{2 \log(2/\delta_2)}{N_t}}, \quad (19)$$

with probabilities of at least $(1-2\delta_1)$ and $(1-2\delta_2)$, respectively. The derivation of equations (18) and (19) are provided in Appendices I and J, respectively. Here, $\mathcal{L}_{\mathbf{m}}^{(i)} := \{\mathbf{m} \mapsto \ell(\phi(\mathbf{m}|t_i, \mathbf{w})) : \mathbf{w} \in \mathcal{W}_B\}$ is the loss class defined over outcomes \mathbf{m} at time t_i , and $\mathcal{L}_t := \{t \mapsto \mathbb{E}_{\phi(\cdot|t, \mathbf{w}^*)}[\ell(\phi(\mathbf{m}|t, \mathbf{w}))] : \mathbf{w} \in \mathcal{W}_B\}$ is the loss class defined over time t . The empirical Rademacher complexities are defined as:

$$\hat{\mathfrak{R}}_{\mathcal{S}_i}(\mathcal{L}_{\mathbf{m}}^{(i)}) := \mathbb{E}_{\sigma} \left[\sup_{\mathbf{w} \in \mathcal{W}_B} \frac{1}{N_c} \sum_{k=1}^{N_c} \sigma_{(i,k)} \ell(\phi(\mathbf{m}_{(i,k)}|t_i, \mathbf{w})) \right] \text{ and } \hat{\mathfrak{R}}_{\mathcal{T}}(\mathcal{L}_t) := \mathbb{E}_{\sigma} \left[\sup_{\mathbf{w} \in \mathcal{W}_B} \frac{1}{N_t} \sum_{i=1}^{N_t} \sigma_i L_{t_i}(\mathbf{w}) \right],$$

where $\{\sigma_{(i,k)}\}$ and $\{\sigma_i\}$ are independent Rademacher random variables (i.e., uniformly distributed on $\{\pm 1\}$). It remains to derive bounds on the Rademacher complexities of the loss classes. We bound $\hat{\mathfrak{R}}_{\mathcal{S}_i}(\mathcal{L}_m^{(i)})$ using the contraction lemma [99, Lemma 26.9] together with Lemma 3, as stated in Proposition 3. Additionally, we bound $\hat{\mathfrak{R}}_{\mathcal{T}}(\mathcal{L}_t)$ using Dudley's theorem [100] [76, Example 5.24] and Eqn. 17, as stated in Proposition 4.

Proposition 3. *Given a set of sampled times \mathcal{T} , the empirical Rademacher complexity of the loss class $\mathcal{L}_m^{(i)}$ satisfies the following bound:*

$$\max_i \hat{\mathfrak{R}}_{\mathcal{S}_i}(\mathcal{L}_m^{(i)}) \leq \frac{\sqrt{2 \log(2D)}}{p_{\min} \sqrt{N_c}},$$

for each $t_i \in \mathcal{T}$, as well as for any set of measurement outcomes \mathcal{S}_i .

Proof. The proof is provided in Appendix K. □

Proposition 4. *The empirical Rademacher complexity of the loss class \mathcal{L}_t satisfies the following bound:*

$$\hat{\mathfrak{R}}_{\mathcal{T}}(\mathcal{L}_t) \leq \frac{36 L_\phi B \sqrt{\pi c}}{p_{\min} \sqrt{N_c}},$$

for any set of sampled times \mathcal{T} .

Proof. The proof is provided in Appendix L. □

Finally, by applying Propositions 3 and 4, along with equations (18) and (19), and setting $\delta_1 = \delta_2 = \delta$, we derive the following: for any $\delta \in (0, 1/4)$, with probability at least $(1 - 4\delta)$, we conclude that

$$\sup_{\mathbf{w} \in \mathcal{W}_B} |\hat{L}(\mathbf{w}) - L(\mathbf{w})| \leq \frac{36 L_\phi B \sqrt{\pi c}}{p_{\min} \sqrt{N_t}} + \frac{2\sqrt{2 \log(2D)}}{p_{\min} \sqrt{N_c}} + 3(-\log p_{\min}) \left(\sqrt{\frac{2 \log(2/\delta)}{N_t}} + \sqrt{\frac{\log(2N_t/\delta)}{2N_c}} \right).$$

D. Construction of the parameterized Hamiltonian for GRNs (Eqn. 3)

We first write the Hamiltonian as a sum of pairwise interaction terms, $H(\mathbf{w}) = \sum_{(i,j) \in \mathcal{E}} w_{ij} H_{ij}$, where w_{ij} quantifies the strength and direction of regulation from \mathbf{g}_i to \mathbf{g}_j and the operator H_{ij} represents the pairwise interaction term that captures the *quantum-like* directed regulatory influence of \mathbf{g}_i on \mathbf{g}_j . The structure of the interaction terms H_{ij} is as follows. Each such term must (i) act on the gene \mathbf{g}_j only when gene \mathbf{g}_i is expressed, and (ii) given \mathbf{g}_i is expressed, it must change the state of \mathbf{g}_j between $|0\rangle_j$ and $|1\rangle_j$. The first conditionality is naturally enforced by the operator $|1\rangle\langle 1|_i$. Note that operators such as $|1\rangle\langle 0|_i$ and $|0\rangle\langle 1|_i$ are not suitable in this context, as they would change the state of \mathbf{g}_i instead of simply conditioning the interaction on its presence. Therefore, H_{ij} takes the form $H_{ij} = |1\rangle\langle 1|_i \otimes O_j$, where O_j is an operator acting on \mathbf{g}_j .

The second condition requires that the operator O_j contains only off-diagonal elements, i.e., $|1\rangle\langle 0|_j$ (transition from unexpressed to expressed) and $|0\rangle\langle 1|_j$ (transition from expressed to unexpressed). To determine the relative signs of these transitions, recall that the system evolves according to the Schrodinger equation $\frac{d}{dt} |\psi(t)\rangle = -iH|\psi(t)\rangle$. The generator $-iw_{ij}H_{ij}$ governs the direction of regulatory influence of \mathbf{g}_i on \mathbf{g}_j . To

encode a meaningful distinction between activation $|0\rangle_j \rightarrow |1\rangle_j$ and repression $|1\rangle_j \rightarrow |0\rangle_j$, we impose a condition on the action of this generator. When g_i is expressed, we require

$$-iw_{ij}H_{ij}|1\rangle_i|0\rangle_j = +w_{ij}|1\rangle_i|1\rangle_j, \quad -iw_{ij}H_{ij}|1\rangle_i|1\rangle_j = -w_{ij}|1\rangle_i|0\rangle_j.$$

This asymmetry condition ensures that the sign associated with the transitions between the expression states of g_j is consistent with our convention for w_{ij} . In particular, when $w_{ij} > 0$, corresponding to activation, the transition $|0\rangle_j \rightarrow |1\rangle_j$ appears with a positive sign, while the reverse transition $|1\rangle_j \rightarrow |0\rangle_j$ appears with a negative sign. Conversely, when $w_{ij} < 0$, corresponding to repression, the sign assignments are reversed: the transition $|1\rangle_j \rightarrow |0\rangle_j$ receives a positive sign and $|0\rangle_j \rightarrow |1\rangle_j$ receives a negative sign. These requirements uniquely lead to the selection of the Pauli operator Y_j . Moreover, this construction preserves Hermiticity. Note that X_j also contains only off-diagonal elements. However, it assigns identical signs for both $|0\rangle_j \rightarrow |1\rangle_j$ and $|1\rangle_j \rightarrow |0\rangle_j$. As a result, it does not provide a distinction between activation and repression at the level of the generator. Taking into account all the requirements, the GRN Hamiltonian is therefore expressed as

$$H(\mathbf{w}) = \sum_{(i,j) \in \mathcal{E}} w_{ij} (|1\rangle\langle 1|_i \otimes (i|1\rangle\langle 0|_j - i|0\rangle\langle 1|_j)) = \sum_{(i,j) \in \mathcal{E}} w_{ij} \frac{1}{2}(\mathbf{I} - Z_i) \otimes Y_j.$$

E. Construction of the IC-POVM for GRNs (Eqn. 5)

We employ an *informationally complete* measurement in QHGM, assuming that gene expression data are sufficient to reconstruct the underlying regulatory state of the system. In other words, by observing the distribution of expression levels across all genes, we can infer the latent state that encodes the regulatory logic of the network. This aligns with a common assumption in systems biology that transcriptomic data across sufficiently enough pseudotime can be used to infer gene–gene interactions [56], [58], [101], [102].

The main idea behind the construction of the IC-POVM is that its outcomes should provide a discrete representation of gene expression in a cell. Since we represent a gene as a qubit, the IC-POVM requires at least four linearly independent elements [97]. To construct these four IC-POVM elements, consider the parameterized Bloch-sphere representation of a single-qubit Hermitian operator in terms of Pauli operators [103]

$$\Lambda_m = \frac{1}{4}(\mathbf{I} + \vec{r}_m \cdot \vec{\sigma}), \quad m \in \{0, 1, 2, 3\},$$

where $\vec{r}_m \in \mathbb{R}^3$ are Bloch vectors and $\vec{\sigma} = (X, Y, Z)$. The POVM condition requires $\sum_{m=0}^3 \Lambda_m = \mathbf{I}$, which implies $\sum_{m=0}^3 \vec{r}_m = 0$ and $\|\vec{r}_m\|_2 = 1$ for all m . Furthermore, the informational completeness requires the four operators $\{\Lambda_m\}_{m=0}^3$ to be linearly independent, i.e., the following 4×4 matrix

$$R = \begin{bmatrix} 1 & 1 & 1 & 1 \\ \vec{r}_0 & \vec{r}_1 & \vec{r}_2 & \vec{r}_3 \end{bmatrix}$$

having full rank. The constraints imposed by normalization, positivity, and informational completeness define an underdetermined system for the Bloch vectors $\{\vec{r}_m\}_{m=0}^3$. As a result, many IC-POVM constructions are possible. However, we construct a set of four elements whose measurement outcomes m correspond to distinct levels of gene expression.

To this end, we introduce *expression score* $\tau_m \in [0, 1]$, defined as

$$\tau_m := \frac{\text{tr}(|1\rangle\langle 1| \Lambda_m)}{\text{tr}(\Lambda_m)} = \frac{(1 - \cos \alpha_m)}{2},$$

where α_m measures the alignment of \vec{r}_m with the reference state $|0\rangle$ and $\cos \alpha_m$ corresponds to the Z-axis component of the Bloch vector \vec{r}_m . For instance, $\vec{r}_m = (0, 0, \cos 0) = (0, 0, 1)$ yields $\tau_m = 0$, corresponding to the state $|0\rangle$ and $\vec{r}_m = (0, 0, \cos \pi) = (0, 0, -1)$ yields $\tau_m = 1$, corresponding to the state $|1\rangle$. Note that τ_m is not a Born probability of any measurement on the unknown state; rather, it provides a fixed, geometry-based encoding of measurement outcomes that is consistent with our Z-axis interpretation of a gene being *unexpressed* or *expressed* within a cell. Guided by this interpretation, we choose angles $\{\alpha_m\}_{m=0}^3$ symmetrically as $\pi/6, 2\pi/6, 4\pi/6$, and $5\pi/6$, respectively. This choice yields an ordered set of expression scores: $\tau_0 = 0.0670, \tau_1 = 0.25, \tau_2 = 0.75, \tau_3 = 0.9330$, representing four distinct levels of gene expression ranging from lower to higher expression, respectively. The associated Z-components of Bloch vectors $\{\vec{r}_m\}_{m=0}^3$ are $\sqrt{3}/2, 1/2, -1/2$, and $-\sqrt{3}/2$, respectively, which remains consistent with the zero-sum constraint $\sum_{m=0}^3 \vec{r}_m = 0$. The X and Y components of Bloch vectors are then selected so that each \vec{r}_m is a unit vector and the matrix R is of full rank. One explicit solution satisfying these constraints is given as $\vec{r}_0 = (1/2, 0, \sqrt{3}/2)$, $\vec{r}_1 = (-1/2, -1/\sqrt{2}, 1/2)$, $\vec{r}_2 = (-1/2, 1/\sqrt{2}, 1/2)$, and $\vec{r}_3 = (1/2, 0, -\sqrt{3}/2)$, which gives the IC-POVM given in (5).

Remark 1. A canonical example of an informationally complete measurement for a qubit is the symmetric informationally complete POVM (SIC-POVM) [104], whose four elements correspond to Bloch vectors pointing to the vertices of a regular tetrahedron. While mathematically elegant, this construction does not readily admit a biologically interpretable ordering of measurement outcomes. The Bloch vectors corresponding to the SIC-POVM are given as

$$\vec{r}_0 = (0, 0, 1), \vec{r}_1 = \left(\frac{2\sqrt{3}}{3}, 0, -\frac{1}{3}\right), \vec{r}_2 = \left(-\frac{\sqrt{2}}{3}, \frac{\sqrt{6}}{3}, -\frac{1}{3}\right), \text{ and } \vec{r}_3 = \left(-\frac{\sqrt{2}}{3}, -\frac{\sqrt{6}}{3}, -\frac{1}{3}\right).$$

The resulting expression scores are as follows: $\tau_0 = 0, \tau_1 = \tau_2 = \tau_3 = 0.667$. Thus, three of the four SIC-POVM elements give identical τ_m . This degeneracy prevents a meaningful ordering of measurement outcomes, making SIC-POVM unsuitable for the discrete representation of gene expression in a cell.

Remark 2 (Infeasible symmetric angles). A natural symmetric choice of angles is $\{0, \pi/3, 2\pi/3, \pi\}$. However, imposing these angles together with the normalization and zero-sum constraints leads to Bloch

vectors of the form $\vec{r}_0 = (0, 0, 1)$, $\vec{r}_1 = (a, \pm\sqrt{1-a^2}, 0)$, $\vec{r}_2 = (-a, \mp\sqrt{1-a^2}, 0)$, and $\vec{r}_3 = (0, 0, -1)$, for some $a \in [0, 1]$. As a result, the matrix R constructed from these vectors is rank-deficient. This means the corresponding POVM elements are not linearly independent, making it impossible to construct an IC-POVM from this selection.

Remark 3 (Uniform discretization). *An alternative feasible construction can be obtained by choosing evenly spaced angles, i.e., $\alpha_m = (m + 1)\pi/5$, $m = 0, \dots, 3$. However, this construction yields nearly uniform bins for discretizing normalized scRNA-seq data. In contrast, our choice $\{\pi/6, 2\pi/6, 4\pi/6, 5\pi/6\}$ deliberately produces non-uniform bin widths (see Fig. 2B). This asymmetry is beneficial in the current gene expression context. Since near-unexpressed and strongly expressed regimes, i.e., $m = 0$ and $m = 3$, are more decisive for characterizing gene regulation. Therefore, these extreme categories must be assigned finer resolution through smaller bin widths, whereas the intermediate expression regimes, i.e., $m = 1$ and $m = 2$, can accommodate coarser grouping.*

F. Variational Quantum Algorithm for GRN Inference

We now describe the VQ-Net algorithm for learning the QHGM parameters using discretized scRNA-seq data collected along pseudotime. The raw scRNA-seq data (genes \times cells) is first preprocessed using tools such as Scanpy [105] or the Seurat (R package) toolkit [106]. Next, the expression profile of each cell is normalized to the range $[0, 1]$ using methods such as Min-Max normalization.

1. Pseudotime analysis: Following preprocessing and normalization, a pseudotime value is assigned to each cell to capture its position along an inferred developmental trajectory. This step can be performed using established pseudotime inference methods such as Monocle [107] or graph-based approaches, including VIA [72], which output a scalar pseudotime value for each cell. The resulting pseudotime t represents the progression of cell-state transitions inferred from the transcriptomic data. In practice, however, these inferred pseudotime values are affected by the noise in scRNA-seq data [108], [109]. This leads to small differences between consecutive pseudotime values assigned to cells. Such fine-scale variability can introduce numerical instability and increase statistical noise during learning. To obtain stable pseudotime values and align with our QHL framework (which requires repeated measurements at discrete time points), the algorithm categorizes pseudotime by grouping cells into bins. Each bin is then assigned a representative pseudotime given by the median pseudotime of the cells it contains.

2. Discretization of scRNA-seq data: The algorithm uses the presence score τ_m to determine the bins for discretizing the continuous and normalized scRNA-seq data into four discrete levels, corresponding to the measurement outcomes $m \in \{0, 1, 2, 3\}$. These levels represent lower to higher gene expression, respectively. The boundaries of the discretization bins are defined by the midpoints between consecutive expression scores.

Let $b_i = (\tau_{i-1} + \tau_i)/2$ for $i = 1, 2, 3$. Additionally, define $b_0 = 0$ and $b_4 = 1$. Then, a normalized expression value $g \in [0, 1]$ is assigned to a discrete level m as follows

$$m = i \quad \text{if} \quad b_i \leq x < b_{i+1}, \quad i \in \{0, 1, 2, 3\}.$$

The discretization process is summarized in Fig. 2B. Thus, we get the discretized scRNA-seq data $\mathcal{G} \in \{0, 1, 2, 3\}^{N_t \times N_c \times n}$. Here, N_t denotes the number of pseudotime bins, N_c denotes the number of cells per bin, and n is the number of genes in the network.

3. Initial state preparation: The system is initialized in a product state as given in (4), using available biological priors to estimate the amplitude angles θ_i and phase angles ϕ_i of individual qubits. For example, gene-specific θ_i can be estimated from the single-cell expression profiles corresponding to the pseudotime $t = 0$ [110], by mapping normalized expression levels to empirical activation frequencies [66]. The phases ϕ_i can be computed using kinetic information derived from transcriptional velocity or pseudotemporal ordering inferred from RNA velocity analyses [80] [111]. In the absence of such prior information, the system can be initialized in a uniform superposition with $\theta_i = \pi/2$ and $\phi_i = 0$ for all i , providing an unbiased starting configuration. More generally, when priors are unavailable or uncertain, the amplitude and phase parameters, θ and ϕ , can be treated as trainable variables and jointly learned along with the weights \mathbf{w} .

4. Mini-Batch Optimization: The algorithm processes the data \mathcal{G} in mini-batches of size B to enhance computational efficiency and introduce stochasticity, which helps avoid non-global stationary points. At the beginning of training, during each training epoch, batches are drawn sequentially to ensure complete coverage of the dataset across all N_t pseudotime points. Once the entire dataset has been processed, subsequent batches are sampled uniformly at random to improve generalization. For each pseudotime t and each cell index k within a batch, the corresponding measurement outcome $\mathbf{m}_{(t,k)}$ is used to evaluate the model-predicted probability:

$$\phi(\mathbf{m}_{(t,k)}, (\theta, \phi, \mathbf{w})) = \langle \psi_t(\theta, \phi, \mathbf{w}) | \Lambda_{\mathbf{m}_{(t,k)}} | \psi_t(\theta, \phi, \mathbf{w}) \rangle$$

where $\Lambda_{\mathbf{m}_{(t,k)}}$ denotes the IC-POVM element corresponding to outcome $\mathbf{m}_{(t,k)}$. The empirical loss over a batch is computed as:

$$\widehat{\mathcal{L}}_B(\theta, \phi, \mathbf{w}) = -\frac{1}{BN_t} \sum_{t=1}^{N_t} \sum_{k=1}^B \log \phi(\mathbf{m}_{(t,k)}, (\theta, \phi, \mathbf{w})).$$

The parameters $(\hat{\theta}, \hat{\phi}, \hat{\mathbf{w}})$ are obtained by minimizing $\widehat{\mathcal{L}}_B$ using a classical optimizer, subject to constraints $w_{ij} \in [-w_{\max}, w_{\max}]$ for all (i, j) . Furthermore, to convert this constrained optimization into an unconstrained form, the algorithm introduces a latent variable $\tilde{w}_{ij} \in \mathbb{R}$ and reparameterizes the weights as $w_{ij} = w_{\max} \tanh(\tilde{w}_{ij})$. This transformation guarantees that w_{ij} always remains within the valid range during optimization while using optimizers over unconstrained parameters \tilde{w}_{ij} .

G. Numerical Experiments and Implementation Details

Synthetic Data Generation. We first construct a ground-truth GRN consisting of $n = 12$ genes, corresponding to a 12-qubit system. The weights \mathbf{w} are sampled independently and uniformly from the interval $[-1, 1]$ to ensure numerical stability. The initial-state parameters are sampled randomly, with $\theta_i \sim \text{Unif}[0, \pi]$ and $\phi_i \sim \text{Unif}[0, 2\pi]$ for each gene. Given the ground-truth parameters, gene-expression data are generated by simulating QHGM dynamics starting from an initial product state. We sample $N_t = 65$ pseudotime points uniformly from the interval $[0, 1]$ and, at each time point, we generate $N_c = 6000$ measurement samples using the fixed IC-POVM measurement (5). This results in a discretized gene-expression dataset $\mathcal{G} \in \{0, 1, 2, 3\}^{65 \times 6000 \times 12}$. The latent variable \tilde{w}_{ij} are initialized uniformly in $[-0.5, 0.5]$,

Training Details. We train the QHGM using PennyLane [112] and JAX [113]. The latent interaction weights \tilde{w}_{ij} are initialized uniformly in $[-0.5, 0.5]$, while the initial-state parameters are initialized as $\theta_i \in [\pi/4, 3\pi/4]$ and $\phi_i \in [\pi/2, 3\pi/2]$. The parameters $\boldsymbol{\theta}$ and $\boldsymbol{\phi}$ are optimized jointly with \mathbf{w} and are not explicitly constrained during training. The initialization ranges for θ_i and ϕ_i are chosen to ensure numerical stability of the state parameterization on the Bloch sphere. Importantly, the learning objective depends only on the induced separable initial state, not on the specific values of θ_i and ϕ_i ; different parameter values that generate the same state (up to a global phase) are therefore equivalent for the optimization. Optimization is performed using the Adam optimizer from Optax with an empirically chosen adaptive learning rate $0.85/\sqrt{\text{epoch}/4 + 1}$. All models are trained for 2500 epochs with batch size $B = 20$ and executed on an NVIDIA A40 GPU.

Glioblastoma dataset. We analyzed the core GBMap dataset, a harmonized scRNA-seq atlas of IDH-wild-type glioblastoma patients from ‘‘Charting the Single-Cell and Spatial Landscape of IDH-Wildtype Glioblastoma with GBmap’’ [73]. The core GBMap dataset comprises approximately 330,000 cells from 109 patients and spans 11 anatomical regions. The GBMap consortium performed comprehensive preprocessing, including quality control and batch correction using an scVI-based integration pipeline [114]. For this study, we focus exclusively on cells annotated as either ‘‘Differentiated-like’’ or ‘‘Stem-like’’ in the annotation level 2 classification. After subsetting, the dataset contains approximately 127,000 cells, distributed across annotation level 3 as follows: AC-like (50,847), MES-like (33,167), NPC-like (22,117), and OPC-like (21,390) (see Fig. 4A). Recent studies indicate that OPC-like cells in glioblastoma possess high proliferative capacity and tumorigenic potential, and hence, are chosen as the root node cell. They are enriched in both adult and pediatric tumors and exhibit cellular plasticity that enables transitions to other glioblastoma cell states [65] [115]. Differential expression (DE) analysis [105] is performed to identify transcriptional (gene expression) differences between the OPC-like and MES-like, and the resulting ranked gene lists were subsequently mapped onto the MSigDB Hallmark gene set collection [116], enabling functional interpretation of the DE signatures. This step identifies which well-studied biological pathways and processes are enriched, making it easier to

understand the key genes and functions involved. The final set of 14 genes are the following: BCAN, STMN1, HES6, ETV1, CADM2, MMP16, CKB, LIMA1, VCAN, JPT1, ASCL1, CDK4, TUBB2B, and NCAM1.

Training Details. Since the released dataset does not include the learned scVI.SCANVI embeddings, we will recompute them to ensure reproducibility in downstream analyses, particularly for the calculation of PCA embeddings and pseudotime. We will follow the parameters from the original study while making necessary adjustments to accommodate updates in the newer version of scvi-tools. We use the py-VIA package [72] on the PCA embedding ($k = 50$, Jacobian-weighted edges as True) to find pseudotime values for each cell. An OPC-like cell (barcode: 118_1_29) is selected as the root, with AC-like and MES-like states defined as terminal groups. Disconnected components were excluded, and a fixed random seed (42) is used to ensure reproducibility. This assigns each cell a pseudotime value along a differentiation trajectory, providing the approximate temporal index t in the subsequent quantum simulation. The scRNA-seq data is preprocessed using the Scanpy toolkit [105], and the expression values are subsequently transformed using Min-Max normalization per cell with scikit-learn [117]. To capture approximate temporal structure, the pseudotime vector is partitioned into $N_t = 50$ equally populated bins. For each pseudotime bin and each cell within the bins, the n -length vector of discretized gene expression, denoted as $\mathbf{m}_{(t,k)}$, is encoded into a single integer using a base-4 representation. This is expressed by the formula:

$$M_{(t,k)} = \sum_{i=1}^n m_{(t,k)}^{(i)} 4^{(i-1)}, \quad \text{where } m_{(t,k)}^{(i)} \in \{0, 1, 2, 3\}.$$

This encoding process converts a three-dimensional dataset \mathcal{G} (pseudotime bins \times cells \times genes) into a two-dimensional dataset (pseudotime bins \times cells). We run 10 different simulations consisting of two complementary initial state preparation strategies. In the first approach, all parameters, including rotation angles θ_i and ϕ_i for each gene (4), as well as the weights w_{ij} , are treated as learnable parameters. In the second approach, the initial state preparation parameters are fixed at $\theta_i = \pi/2$ and $\phi_i = 0$, while only the weights are learnable. For each approach, we perform five random initializations of the parameters to ensure robustness and run for 3000 epochs. The model parameters $(\boldsymbol{\theta}, \boldsymbol{\phi}, \mathbf{w})$ are updated using the ADAM optimizer, with an adaptive learning rate $0.085/\sqrt{(\text{epoch}/4) + 1}$, providing smoother convergence during later training stages. Across these independent runs, we compute the median of each weight, providing a stable, representative estimate of network interactions while accounting for parameter initialization variability. This strategy allows us to capture a more comprehensive and robust understanding of the underlying regulatory network (see Fig. 4B).

Acknowledgments

This research was supported in part through computational resources and services provided by Advanced Research Computing at the University of Michigan, Ann Arbor.

Data Availability

The scRNA-seq data analyzed in this study are publicly available in the core GBMap section through the CZ CELLxGENE Discover portal.

Link: <https://cellxgene.cziscience.com/collections/999f2a15-3d7e-440b-96ae-2c806799c08c>.

Code Availability

All the experimental results and source codes are available at <https://github.com/mdaamirQ/QHGM>.

REFERENCES

- [1] D. Burgarth and A. Ajoy, “Evolution-free hamiltonian parameter estimation through zeeman markers,” *Physical Review Letters*, vol. 119, no. 3, p. 030402, 2017.
- [2] J. Wang, S. Paesani, R. Santagati, S. Knauer, A. A. Gentile, N. Wiebe, M. Petruzzella, J. L. O’Brien, J. G. Rarity, A. Laing, *et al.*, “Experimental quantum hamiltonian learning,” *Nature Physics*, vol. 13, no. 6, pp. 551–555, 2017.
- [3] H. Y. Kwon, H. Yoon, C. Lee, G. Chen, K. Liu, A. Schmid, Y. Wu, J. Choi, and C. Won, “Magnetic hamiltonian parameter estimation using deep learning techniques,” *Science advances*, vol. 6, no. 39, p. eabb0872, 2020.
- [4] D. Wang, S. Wei, A. Yuan, F. Tian, K. Cao, Q. Zhao, Y. Zhang, C. Zhou, X. Song, D. Xue, *et al.*, “Machine learning magnetic parameters from spin configurations,” *Advanced Science*, vol. 7, no. 16, p. 2000566, 2020.
- [5] S.-A. Guo, Y.-K. Wu, J. Ye, L. Zhang, Y. Wang, W.-Q. Lian, R. Yao, Y.-L. Xu, C. Zhang, Y.-Z. Xu, *et al.*, “Hamiltonian learning for 300 trapped ion qubits with long-range couplings,” *Science Advances*, vol. 11, no. 5, p. eadt4713, 2025.
- [6] N. Karjalainen, G. Lupi, R. Koch, A. O. Fumega, and J. L. Lado, “Hamiltonian learning quantum magnets with dynamical impurity tomography,” *arXiv preprint arXiv:2510.18613*, 2025.
- [7] J. B. Altepeter, D. Branning, E. Jeffrey, T. Wei, P. G. Kwiat, R. T. Thew, J. L. O’Brien, M. A. Nielsen, and A. G. White, “Ancilla-assisted quantum process tomography,” *Physical Review Letters*, vol. 90, no. 19, p. 193601, 2003.
- [8] D. W. Leung, “Choi’s proof as a recipe for quantum process tomography,” *Journal of Mathematical Physics*, vol. 44, no. 2, pp. 528–533, 2003.
- [9] S. Rahimi-Keshari, A. Scherer, A. Mann, A. T. Rezakhani, A. Lvovsky, and B. C. Sanders, “Quantum process tomography with coherent states,” *New Journal of Physics*, vol. 13, no. 1, p. 013006, 2011.
- [10] M. Mohseni, A. T. Rezakhani, and D. A. Lidar, “Quantum-process tomography: Resource analysis of different strategies,” *Physical Review A—Atomic, Molecular, and Optical Physics*, vol. 77, no. 3, p. 032322, 2008.
- [11] Y. Wang, D. Dong, B. Qi, J. Zhang, I. R. Petersen, and H. Yonezawa, “A quantum hamiltonian identification algorithm: Computational complexity and error analysis,” *IEEE Transactions on Automatic Control*, vol. 63, no. 5, pp. 1388–1403, 2018.
- [12] A. Anshu, S. Kaiser, and T. Li, “Sample-efficient learning of quantum many-body hamiltonians,” *Nature Physics*, vol. 17, pp. 911–915, 2021.
- [13] J. Haah, R. Kothari, and E. Tang, “Optimal learning of quantum hamiltonians from high-temperature gibbs states,” in *2022 IEEE 63rd Annual Symposium on Foundations of Computer Science (FOCS)*, pp. 135–146, IEEE, 2022.
- [14] A. Gu, L. Cincio, and P. J. Coles, “Practical hamiltonian learning with unitary dynamics and gibbs states,” *Nature Communications*, vol. 15, no. 1, p. 312, 2024.
- [15] C.-F. Chen, A. Anshu, and Q. T. Nguyen, “Learning quantum gibbs states locally and efficiently,” *arXiv preprint arXiv:2504.02706*, 2025.

- [16] A. Bakshi, A. Liu, A. Moitra, and E. Tang, “Learning quantum hamiltonians at any temperature in polynomial time,” in *Proceedings of the 56th Annual ACM Symposium on Theory of Computing (STOC)*, (New York, NY, USA), Association for Computing Machinery, 2024.
- [17] X.-L. Qi and D. Ranard, “Determining a local hamiltonian from a single eigenstate,” *Quantum*, vol. 3, p. 159, 2019.
- [18] M. Dupont, N. Macé, and N. Laflorencie, “From eigenstate to hamiltonian: Prospects for ergodicity and localization,” *Physical Review B*, vol. 100, no. 13, p. 134201, 2019.
- [19] E. Chertkov and B. K. Clark, “Computational inverse method for constructing spaces of quantum models from wave functions,” *Physical Review X*, vol. 8, no. 3, p. 031029, 2018.
- [20] M. Greiter, V. Schnells, and R. Thomale, “Method to identify parent hamiltonians for trial states,” *Phys. Rev. B*, vol. 98, p. 081113, Aug 2018.
- [21] E. Bairey, C. Guo, D. Poletti, N. H. Lindner, and I. Arad, “Learning the dynamics of open quantum systems from their steady states,” *New Journal of Physics*, vol. 22, no. 3, p. 032001, 2020.
- [22] T. J. Evans, R. Harper, and S. T. Flammia, “Scalable bayesian hamiltonian learning,” *arXiv preprint arXiv:1912.07636*, 2019.
- [23] E. Bairey, I. Arad, and N. H. Lindner, “Learning a local hamiltonian from local measurements,” *Physical Review Letters*, vol. 122, no. 2, p. 020504, 2019.
- [24] C. Cao, S.-Y. Hou, N. Cao, and B. Zeng, “Supervised learning in hamiltonian reconstruction from local measurements on eigenstates,” *Journal of Physics: Condensed Matter*, vol. 33, no. 6, p. 064002, 2020.
- [25] A. Shabani, R. L. Kosut, M. Mohseni, H. Rabitz, M. A. Broome, M. P. Almeida, A. Fedrizzi, and A. G. White, “Estimation of many-body quantum hamiltonians via compressive sensing,” *Physical Review A*, vol. 84, no. 1, p. 012107, 2011.
- [26] D. Stilck França, L. A. Markovich, V. V. Dobrovitski, A. H. Werner, and J. Borregaard, “Efficient and robust estimation of many-qubit hamiltonians,” *Nature Communications*, vol. 15, no. 1, p. 311, 2024.
- [27] A. Zubida, E. Yitzhaki, N. H. Lindner, and E. Bairey, “Optimal short-time measurements for hamiltonian learning,” *arXiv preprint arXiv:2108.08824*, 2021.
- [28] D. Hangleiter, I. Roth, J. Fuksa, J. Eisert, and P. Roushan, “Robustly learning the hamiltonian dynamics of a superconducting quantum processor,” *Nature Communications*, vol. 15, no. 1, p. 9595, 2024.
- [29] W. Yu, J. Sun, Z. Han, and X. Yuan, “Robust and efficient hamiltonian learning,” *Quantum*, vol. 7, p. 1045, 2023.
- [30] R. Gupta, R. Selvarajan, M. Sajjan, R. D. Levine, and S. Kais, “Hamiltonian learning from time dynamics using variational algorithms,” *The Journal of Physical Chemistry A*, vol. 127, no. 14, pp. 3246–3255, 2023.
- [31] J. Zhang and M. Sarovar, “Quantum hamiltonian identification from measurement time traces,” *Phys. Rev. Lett.*, vol. 113, p. 080401, Aug 2014.
- [32] N. Wiebe, C. Granade, C. Ferrie, and D. G. Cory, “Hamiltonian learning and certification using quantum resources,” *Phys. Rev. Lett.*, vol. 112, p. 190501, May 2014.
- [33] N. Wiebe, C. Granade, C. Ferrie, and D. G. Cory, “Quantum hamiltonian learning using imperfect quantum resources,” *Phys. Rev. A*, vol. 89, p. 042314, Apr 2014.
- [34] N. Wiebe, C. Granade, and D. G. Cory, “Quantum bootstrapping via compressed quantum hamiltonian learning,” *New Journal of Physics*, vol. 17, no. 2, p. 022005, 2015.
- [35] F. Wilde, A. Kshetrimayum, I. Roth, D. Hangleiter, R. Sweke, and J. Eisert, “Scalably learning quantum many-body hamiltonians from dynamical data,” *arXiv preprint arXiv:2209.14328*, 2022.
- [36] S. Liu, X. Wu, and M. Y. Niu, “Optimal and robust in-situ quantum hamiltonian learning through parallelization,” *arXiv preprint arXiv:2510.07818*, 2025.
- [37] H.-Y. Huang, Y. Tong, D. Fang, and Y. Su, “Learning many-body hamiltonians with heisenberg-limited scaling,” *Physical Review Letters*, vol. 130, p. 200403, May 2023.

- [38] H. Li, Y. Tong, T. Gefen, H. Ni, and L. Ying, “Heisenberg-limited hamiltonian learning for interacting bosons,” *npj Quantum Information*, vol. 10, p. 83, September 2024.
- [39] H.-Y. Hu, M. Ma, W. Gong, Q. Ye, Y. Tong, S. T. Flammia, and S. F. Yelin, “Ansatz-free hamiltonian learning with heisenberg-limited scaling,” *arXiv preprint arXiv:2502.11900*, February 2025. arXiv:2502.11900.
- [40] S. D. Sinha and Y. Tong, “Improved hamiltonian learning and sparsity testing through bell sampling,” *arXiv preprint*, vol. arXiv:2509.07937, 2025. arXiv:2509.07937.
- [41] B. Baran and T. Heightman, “Heisenberg-limited quantum hamiltonian learning via randomly spread product-states,” *arXiv preprint*, vol. arXiv:2507.21374, 2025. arXiv:2507.21374.
- [42] V. Giovannetti, S. Lloyd, and L. Maccone, “Quantum-enhanced measurements: beating the standard quantum limit,” *Science*, vol. 306, no. 5700, pp. 1330–1336, 2004.
- [43] V. B. Braginskii and Y. I. Vorontsov, “Quantum-mechanical limitations in macroscopic experiments and modern experimental technique,” *Soviet Physics Uspekhi*, vol. 17, no. 5, p. 644, 1975.
- [44] A. Khrennikov, “On quantum-like probabilistic structure of mental information,” *Open Systems & Information Dynamics*, vol. 11, no. 03, pp. 267–275, 2004.
- [45] A. Khrennikov, “Quantum-like modeling of cognition,” *Frontiers in Physics*, vol. 3, p. 77, 2015.
- [46] A. Khrennikov, “Quantum-like brain: “interference of minds”,” *BioSystems*, vol. 84, no. 3, pp. 225–241, 2006.
- [47] A. Plotnitsky and E. Haven, “The quantum-like revolution,” *A Festschrift for Andrei Khrennikov with a foreword by 2022 Nobel Laureate Anton Zeilinger*, 2023.
- [48] A. Khrennikov, *Ubiquitous quantum structure*. Springer, 2010.
- [49] A. V. Melkikh and A. Khrennikov, “Nontrivial quantum and quantum-like effects in biosystems: Unsolved questions and paradoxes,” *Progress in Biophysics and Molecular Biology*, vol. 119, no. 2, pp. 137–161, 2015.
- [50] E. Haven and A. Khrennikov, *The Palgrave handbook of quantum models in social science: Applications and grand challenges*. Springer, 2017.
- [51] E. M. Pothos and J. R. Busemeyer, “Quantum cognition,” *Annual review of psychology*, vol. 73, no. 1, pp. 749–778, 2022.
- [52] V. Svensson, E. da Veiga Beltrame, and L. Pachter, “A curated database reveals trends in single-cell transcriptomics,” *Database*, vol. 2020, p. baaa073, 2020.
- [53] S. Kim, “ppcor: an r package for a fast calculation to semi-partial correlation coefficients,” *Communications for statistical applications and methods*, vol. 22, no. 6, p. 665, 2015.
- [54] A. T. Specht and J. Li, “Leap: constructing gene co-expression networks for single-cell rna-sequencing data using pseudotime ordering,” *Bioinformatics*, vol. 33, no. 5, pp. 764–766, 2017.
- [55] V. A. Huynh-Thu, A. Irrthum, L. Wehenkel, and P. Geurts, “Inferring regulatory networks from expression data using tree-based methods,” *PloS one*, vol. 5, no. 9, p. e12776, 2010.
- [56] N. Papili Gao, S. M. Ud-Dean, O. Gandrillon, and R. Gunawan, “Sincerities: inferring gene regulatory networks from time-stamped single cell transcriptional expression profiles,” *Bioinformatics*, vol. 34, no. 2, pp. 258–266, 2018.
- [57] A. A. Margolin, I. Nemenman, K. Basso, C. Wiggins, G. Stolovitzky, R. D. Favera, and A. Califano, “Aracne: an algorithm for the reconstruction of gene regulatory networks in a mammalian cellular context,” *BMC bioinformatics*, vol. 7, no. Suppl 1, p. S7, 2006.
- [58] M. Sanchez-Castillo, D. Blanco, I. M. Tienda-Luna, M. Carrion, and Y. Huang, “A bayesian framework for the inference of gene regulatory networks from time and pseudo-time series data,” *Bioinformatics*, vol. 34, no. 6, pp. 964–970, 2018.
- [59] M. Harney, “The effects of quantum entanglement on chromatin and gene expression,” *GeNeDis 2018: Genetics and Neurodegeneration*, pp. 73–76, 2020.

- [60] I. Basieva, A. Khrennikov, M. Ohya, and I. Yamato, “Quantum-like interference effect in gene expression: glucose-lactose destructive interference,” *Systems and synthetic biology*, vol. 5, pp. 59–68, 2011.
- [61] E. Rieper, J. Anders, and V. Vedral, “Quantum entanglement between the electron clouds of nucleic acids in dna,” *arXiv preprint arXiv:1006.4053*, 2010.
- [62] R. Siebert, O. Ammerpohl, M. Rossini, D. Herb, S. Rau, M. B. Plenio, F. Jelezko, and J. Ankerhold, “A quantum physics layer of epigenetics: a hypothesis deduced from charge transfer and chirality-induced spin selectivity of dna,” *Clinical Epigenetics*, vol. 15, no. 1, p. 145, 2023.
- [63] D. Aerts, S. Aerts, J. Broekaert, and L. Gabora, “The violation of bell inequalities in the macroworld,” *Foundations of Physics*, vol. 30, no. 9, pp. 1387–1414, 2000.
- [64] P. H. Alvarez, L. Gerhards, I. A. Solov’yov, and M. C. de Oliveira, “Quantum phenomena in biological systems,” *Frontiers in Quantum Science and Technology*, vol. 3, p. 1466906, 2024.
- [65] C. Neftel, J. Laffy, M. G. Filbin, T. Hara, M. E. Shore, G. J. Rahme, A. R. Richman, D. Silverbush, M. L. Shaw, C. M. Hebert, *et al.*, “An integrative model of cellular states, plasticity, and genetics for glioblastoma,” *Cell*, vol. 178, no. 4, pp. 835–849, 2019.
- [66] C. Roman-Vicharra *et al.*, “Quantum circuit model for inferring gene regulatory networks from single-cell transcriptomic data,” *npj Quantum Information*, 2023. Demonstrates qubit entanglement modeling gene interactions.
- [67] V. Dubovitskii, A. Bose, F. Utro, and L. Pardia, “On quantum random walks in biomolecular networks,” *arXiv preprint*, 2025. QRWs outperform classical methods in ranking disease genes and identifying network drivers.
- [68] D. Konar, N. Sreekumar, R. Jiang, and V. Aggarwal, “Alz-qnet: A quantum regression network for studying alzheimer’s gene interactions,” *Computers in Biology and Medicine*, vol. 196, p. 110837, 2025.
- [69] S. Romero, V. S. Kumar, R. S. Chapkin, and J. J. Cai, “Quantum generative modeling of single-cell transcriptomics: Capturing gene-gene and cell-cell interactions,” *arXiv preprint arXiv:2510.12776*, 2025.
- [70] F. Utro, A. Bose, R.-s. Wang, V. Dubovitskii, and L. Parida, “A perspective on quantum computing for analyzing cell-cell communication networks,” in *Conference on Intelligent Systems for Molecular Biology*, 2024.
- [71] T. M. Cover and J. A. Thomas, *Elements of Information Theory*. Wiley Series in Telecommunications and Signal Processing, John Wiley & Sons, Inc., 2 ed., 2006.
- [72] S. V. Stassen, G. G. Yip, K. K. Wong, J. W. Ho, and K. K. Tsia, “Generalized and scalable trajectory inference in single-cell omics data with via,” *Nature communications*, vol. 12, no. 1, p. 5528, 2021.
- [73] C. Ruiz-Moreno, S. M. Salas, E. Samuelsson, M. Minaeva, I. Ibarra, M. Grillo, S. Brandner, A. Roy, K. Forsberg-Nilsson, M. E. Kranendonk, *et al.*, “Charting the single-cell and spatial landscape of idh-wild-type glioblastoma with gbmap,” *Neuro-Oncology*, 2025.
- [74] S. Grochans, A. M. Cybulska, D. Simińska, J. Korbecki, K. Kojder, D. Chlubek, and I. Baranowska-Bosiacka, “Epidemiology of glioblastoma multiforme—literature review,” *Cancers*, vol. 14, no. 10, p. 2412, 2022.
- [75] A. Rodríguez-Camacho, J. G. Flores-Vázquez, J. Moscardini-Martelli, J. A. Torres-Ríos, A. Olmos-Guzmán, C. S. Ortiz-Arce, D. R. Cid-Sánchez, S. R. Pérez, M. D. S. Macías-González, L. C. Hernández-Sánchez, *et al.*, “Glioblastoma treatment: state-of-the-art and future perspectives,” *International journal of molecular sciences*, vol. 23, no. 13, p. 7207, 2022.
- [76] M. J. Wainwright, *High-dimensional statistics: A non-asymptotic viewpoint*, vol. 48. Cambridge university press, 2019.
- [77] D. Szklarczyk, K. Nastou, M. Koutrouli, R. Kirsch, F. Mehryary, R. Hachilif, D. Hu, M. E. Peluso, Q. Huang, T. Fang, *et al.*, “The string database in 2025: protein networks with directionality of regulation,” *Nucleic Acids Research*, vol. 53, no. D1, pp. D730–D737, 2025.
- [78] S. Müller-Dott, E. Tsvirouli, M. Vazquez, R. O. Ramirez Flores, P. Badia-i Mompel, R. Fallegger, D. Türei, A. Læg Reid, and

- J. Saez-Rodriguez, “Expanding the coverage of regulons from high-confidence prior knowledge for accurate estimation of transcription factor activities,” *Nucleic acids research*, vol. 51, no. 20, pp. 10934–10949, 2023.
- [79] E. Wingender, P. Dietze, H. Karas, and R. Knüppel, “Transfac: a database on transcription factors and their dna binding sites,” *Nucleic acids research*, vol. 24, no. 1, pp. 238–241, 1996.
- [80] G. La Manno, R. Soldatov, A. Zeisel, E. Braun, H. Hochgerner, V. Petukhov, K. Lidschreiber, M. E. Kastrioti, P. Lönnerberg, A. Furlan, *et al.*, “Rna velocity of single cells,” *Nature*, vol. 560, no. 7719, pp. 494–498, 2018.
- [81] C. Trapnell, D. Cacchiarelli, J. Grimsby, P. Pokharel, S. Li, M. Morse, N. J. Lennon, K. J. Livak, T. S. Mikkelsen, and J. L. Rinn, “The dynamics and regulators of cell fate decisions are revealed by pseudotemporal ordering of single cells,” *Nature biotechnology*, vol. 32, no. 4, pp. 381–386, 2014.
- [82] B. L. Myers, K. J. Brayer, L. E. Paez-Beltran, E. Villicana, M. S. Keith, H. Suzuki, J. Newville, R. H. Anderson, Y. Lo, C. M. Mertz, *et al.*, “Transcription factors ascl1 and olig2 drive glioblastoma initiation and co-regulate tumor cell types and migration,” *Nature communications*, vol. 15, no. 1, p. 10363, 2024.
- [83] P. Bao, T. Yokobori, B. Altan, M. Iijima, Y. Azuma, R. Onozato, T. Yajima, A. Watanabe, A. Mogi, K. Shimizu, *et al.*, “High stmn1 expression is associated with cancer progression and chemo-resistance in lung squamous cell carcinoma,” *Annals of Surgical Oncology*, vol. 24, no. 13, pp. 4017–4024, 2017.
- [84] M. Li, A. Xiao, D. Floyd, I. Olmez, J. Lee, J. Godlewski, A. Bronisz, K. P. Bhat, E. P. Sulman, I. Nakano, *et al.*, “Cdk4/6 inhibition is more active against the glioblastoma proneural subtype,” *Oncotarget*, vol. 8, no. 33, p. 55319, 2017.
- [85] K. Michaud, D. A. Solomon, E. Oermann, J.-S. Kim, W.-Z. Zhong, M. D. Prados, T. Ozawa, C. D. James, and T. Waldman, “Pharmacologic inhibition of cyclin-dependent kinases 4 and 6 arrests the growth of glioblastoma multiforme intracranial xenografts,” *Cancer research*, vol. 70, no. 8, pp. 3228–3238, 2010.
- [86] R. Wei, H. Xie, Y. Zhou, X. Chen, L. Zhang, B. Bui, and X. Liu, “Vcan in the extracellular matrix drives glioma recurrence by enhancing cell proliferation and migration,” *Frontiers in Neuroscience*, vol. 18, p. 1501906, 2024.
- [87] S. M. Turaga and J. D. Lathia, “Adhering towards tumorigenicity: altered adhesion mechanisms in glioblastoma cancer stem cells,” *CNS oncology*, vol. 5, no. 4, pp. 251–259, 2016.
- [88] L. M. Parkinson, S. L. Gillen, L. M. Woods, L. Chaytor, D. Marcos, F. R. Ali, J. S. Carroll, and A. Philpott, “The proneural transcription factor ascl1 regulates cell proliferation and primes for differentiation in neuroblastoma,” *Frontiers in Cell and Developmental Biology*, vol. 10, p. 942579, 2022.
- [89] X. Cheng, Z. Tan, X. Huang, Y. Yuan, S. Qin, Y. Gu, D. Wang, C. He, and Z. Su, “Inhibition of glioma development by ascl1-mediated direct neuronal reprogramming,” *Cells*, vol. 8, no. 6, p. 571, 2019.
- [90] M. L. Suvà, E. Rheinbay, S. M. Gillespie, A. P. Patel, H. Wakimoto, S. D. Rabkin, N. Riggi, A. S. Chi, D. P. Cahill, B. V. Nahed, *et al.*, “Reconstructing and reprogramming the tumor-propagating potential of glioblastoma stem-like cells,” *Cell*, vol. 157, no. 3, pp. 580–594, 2014.
- [91] P. L. Bartlett, O. Bousquet, and S. Mendelson, “Local rademacher complexities,” *Ann. Statist.*, vol. 33, no. 1, pp. 1497–1537, 2005.
- [92] E. Z. Macosko, A. Basu, R. Satija, J. Nemeshegyi, K. Shekhar, M. Goldman, I. Tirosh, A. R. Bialas, N. Kamitaki, E. M. Martersteck, *et al.*, “Highly parallel genome-wide expression profiling of individual cells using nanoliter droplets,” *Cell*, vol. 161, no. 5, pp. 1202–1214, 2015.
- [93] J. D. Buenrostro, B. Wu, U. M. Litzenburger, D. Ruff, M. L. Gonzales, M. P. Snyder, H. Y. Chang, and W. J. Greenleaf, “Single-cell chromatin accessibility reveals principles of regulatory variation,” *Nature*, vol. 523, no. 7561, pp. 486–490, 2015.
- [94] H. S. Kaya-Okur, S. J. Wu, C. A. Codomo, E. S. Pledger, T. D. Bryson, J. G. Henikoff, K. Ahmad, and S. Henikoff, “Cut&tag for efficient epigenomic profiling of small samples and single cells,” *Nature communications*, vol. 10, no. 1, p. 1930, 2019.

- [95] E. P. Consortium *et al.*, “An integrated encyclopedia of dna elements in the human genome,” *Nature*, vol. 489, no. 7414, p. 57, 2012.
- [96] J. Pickard, A. Bloch, and I. Rajapakse, “Scalable hypergraph algorithms for observability of gene regulation,” in *2025 European Control Conference (ECC)*, pp. 3145–3150, IEEE, 2025.
- [97] C. Medlock, A. Oppenheim, and P. Boufounos, “Informationally overcomplete povms for quantum state estimation and binary detection,” *arXiv preprint arXiv:2012.05355*, 2020.
- [98] J. A. Tropp *et al.*, “An introduction to matrix concentration inequalities,” *Foundations and Trends® in Machine Learning*, vol. 8, no. 1-2, pp. 1–230, 2015.
- [99] S. Shalev-Shwartz and S. Ben-David, *Understanding machine learning: From theory to algorithms*. Cambridge university press, 2014.
- [100] R. M. Dudley, “The sizes of compact subsets of hilbert space and continuity of gaussian processes,” *Journal of Functional Analysis*, vol. 1, no. 3, pp. 290–330, 1967.
- [101] D. Marbach, J. C. Costello, R. Küffner, N. M. Vega, R. J. Prill, D. M. Camacho, K. R. Allison, M. Kellis, J. J. Collins, *et al.*, “Wisdom of crowds for robust gene network inference,” *Nature methods*, vol. 9, no. 8, pp. 796–804, 2012.
- [102] S. Aibar, C. B. González-Blas, T. Moerman, V. A. Huynh-Thu, H. Imrichova, G. Hulselmans, F. Rambow, J.-C. Marine, P. Geurts, J. Aerts, *et al.*, “Scenic: single-cell regulatory network inference and clustering,” *Nature methods*, vol. 14, no. 11, pp. 1083–1086, 2017.
- [103] M. A. Nielsen and I. L. Chuang, *Quantum computation and quantum information*. Cambridge university press, 2010.
- [104] J. M. Renes, R. Blume-Kohout, A. J. Scott, and C. M. Caves, “Symmetric informationally complete quantum measurements,” *Journal of Mathematical Physics*, vol. 45, no. 6, pp. 2171–2180, 2004.
- [105] F. A. Wolf, P. Angerer, and F. J. Theis, “Scanpy: large-scale single-cell gene expression data analysis,” *Genome biology*, vol. 19, no. 1, p. 15, 2018.
- [106] Y. Hao, T. Stuart, M. H. Kowalski, S. Choudhary, P. Hoffman, A. Hartman, A. Srivastava, G. Molla, S. Madad, C. Fernandez-Granda, *et al.*, “Dictionary learning for integrative, multimodal and scalable single-cell analysis,” *Nature biotechnology*, vol. 42, no. 2, pp. 293–304, 2024.
- [107] C. Trapnell, D. Cacchiarelli, J. Grimsby, P. Pokharel, S. Li, M. Morse, N. J. Lennon, K. J. Livak, T. S. Mikkelsen, and J. L. Rinn, “The dynamics and regulators of cell fate decisions are revealed by pseudotemporal ordering of single cells,” *Nature Biotechnology*, vol. 32, no. 4, pp. 381–386, 2014.
- [108] P. Brennecke, S. Anders, J. K. Kim, A. A. Kolodziejczyk, X. Zhang, V. Proserpio, B. Baying, V. Benes, S. A. Teichmann, J. C. Marioni, *et al.*, “Accounting for technical noise in single-cell rna-seq experiments,” *Nature methods*, vol. 10, no. 11, pp. 1093–1095, 2013.
- [109] D. Grün, L. Kester, and A. Van Oudenaarden, “Validation of noise models for single-cell transcriptomics,” *Nature methods*, vol. 11, no. 6, pp. 637–640, 2014.
- [110] W. Saelens, R. Cannoodt, H. Todorov, and Y. Saeys, “A comparison of single-cell trajectory inference methods,” *Nature biotechnology*, vol. 37, no. 5, pp. 547–554, 2019.
- [111] M. Lange, V. Bergen, M. Klein, M. Setty, B. Reuter, M. Bakhti, H. Lickert, M. Ansari, J. Schniering, H. B. Schiller, *et al.*, “Cellrank for directed single-cell fate mapping,” *Nature methods*, vol. 19, no. 2, pp. 159–170, 2022.
- [112] V. Bergholm, J. Izaac, M. Schuld, C. Gogolin, S. Ahmed, V. Ajith, M. S. Alam, G. Alonso-Linaje, B. AkashNarayanan, A. Asadi, *et al.*, “Pennylane: Automatic differentiation of hybrid quantum-classical computations,” *arXiv preprint arXiv:1811.04968*, 2018.
- [113] J. Bradbury, R. Frostig, P. Hawkins, M. J. Johnson, C. Leary, D. Maclaurin, G. Necula, A. Paszke, J. VanderPlas, S. Wanderman-Milne, and Q. Zhang, “JAX: composable transformations of Python+NumPy programs,” 2018.
- [114] A. Gayoso, R. Lopez, G. Xing, P. Boyeau, V. Valiollah Pour Amiri, J. Hong, K. Wu, M. Jayasuriya, E. Mehlman, M. Langevin,

- et al.*, “A python library for probabilistic analysis of single-cell omics data,” *Nature biotechnology*, vol. 40, no. 2, pp. 163–166, 2022.
- [115] D. B. Zamler and J. Hu, “Primitive oligodendrocyte precursor cells are highly susceptible to gliomagenic transformation,” *Cancer Research*, vol. 83, no. 6, pp. 807–808, 2023.
- [116] A. Liberzon, C. Birger, H. Thorvaldsdóttir, M. Ghandi, J. P. Mesirov, and P. Tamayo, “The molecular signatures database hallmark gene set collection,” *Cell systems*, vol. 1, no. 6, pp. 417–425, 2015.
- [117] F. Pedregosa, G. Varoquaux, A. Gramfort, V. Michel, B. Thirion, O. Grisel, M. Blondel, P. Prettenhofer, R. Weiss, V. Dubourg, *et al.*, “Scikit-learn: Machine learning in python,” *the Journal of machine Learning research*, vol. 12, pp. 2825–2830, 2011.
- [118] F. Nielsen and K. Sun, “Guaranteed bounds on information-theoretic measures of univariate mixtures using piecewise log-sum-exp inequalities,” *Entropy*, vol. 18, no. 12, p. 442, 2016.
- [119] H. E. Haber, “Notes on the matrix exponential and logarithm,” *Santa Cruz Institute for Particle Physics, University of California: Santa Cruz, CA, USA*, 2018.
- [120] J. Watrous, *The theory of quantum information*. Cambridge university press, 2018.

APPENDIX

A. Benchmarking Classical Inference Methods on QHGM-Generated Data

In this subsection, we benchmark state-of-the-art classical inference methods, including ARACNE, GeneNet, GENIE3, and SINCERITIES, on the QHGM-generated data. Recall, QHGM generates discretized gene expression data. However, the classical methods operate. Therefore, we convert the discrete four-level gene expression data to continuous values between 0 and 1 via Beta distributions with expression scores $\{\tau_m\}_{m=0}^3$ as the mode of the distributions (see Appendix B). We empirically evaluate the performance of these classical inference methods using the F1 score and accuracy. In Figs.5A and B, we evaluate F1 score and accuracy for network edge recovery and weights sign recovery, respectively, against different total sample sizes. Network edge recovery is the ability to correctly identify the presence of interactions, regardless of the sign of the weights. Weights sign recovery is the correct identification of both the presence of an edge and the sign of the weights (up-regulation or down-regulation). We keep the ground-truth network’s sparsity at roughly 15% for both network edge recovery and weights sign recovery. Error bars indicate variability across different values of N_t . For a fixed total sample size ($N_t \cdot N_c$), samples are randomly subsampled for each N_t , and the resulting error bars for ARACNE, GeneNet, and GENIE3 reflect the corresponding performance variability.

The average performance of VQ-Net for both network edge recovery and weight sign recovery is above 0.95, and the error bars decrease as the sample size increases. In contrast, for network edge recovery, GENIE3 and GeneNet exhibit slightly better performance than ARACNE and SINCERITIES; however, the average performance remains below that of VQ-NET by more than 20%. Both GeneNet and SINCERITIES do not achieve an F_1 score and accuracy of 0.5 for signed edge recovery. Across all classical methods, we observe that increasing sample size does not yield a substantial improvement in accuracy or F_1 score for both edge and sign recovery.

In Fig. 5C, we assess the performance of classical methods in recovering network edges at various levels of network sparsity, defined as the fraction of edges with non-zero weights in the ground-truth network. Here, VQ-Net again exhibits consistent performance across different levels of sparsity. In contrast, classical methods show a considerable sensitivity to sparsity. For example, GENIE3 performs well at lower sparsity levels, but its performance degrades sharply as the sparsity increases. SINCERITIES’ performance remains the same across different sparsity levels. Whereas GeneNet and ARACNE performance increase as sparsity increases. However, their F_1 score and accuracy are significantly lower than VQ-Net’s at lower sparsity levels.

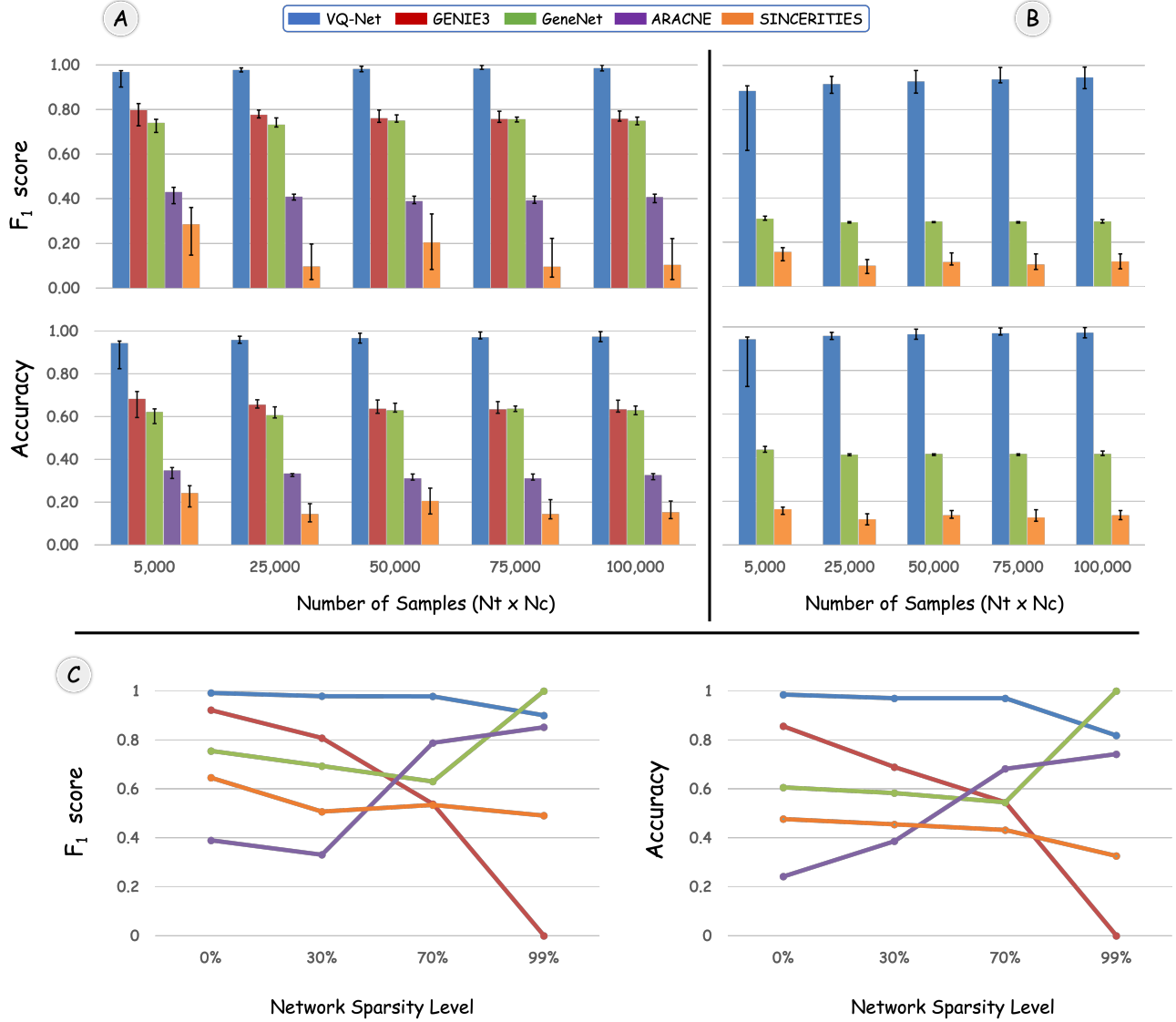


Figure 5: Performance of state-of-the-art classical inference methods on QHGM-generated data. (A) Network Edge recovery (B) Weights Sign recovery (C) Sparsity-Edge recovery Tradeoff

B. Converting Discretized QHGM-Generated Data to Continuous Gene Expression Levels

To transform discrete labels from QHGM into continuous gene expression values, we employ a localized dequantization strategy based on Beta distributions. This approach ensures that each continuous value remains strictly bounded within the IC-POVM bin, while allowing for a controllable degree of stochasticity. We set the expression scores $\tau_0 = 0.067$, $\tau_1 = 0.25$, $\tau_2 = 0.75$, and $\tau_3 = 0.933$, as the mode of the four Beta distributions (see Fig. 6). To generate samples within a bin, we map the interval $[b_{i-1}, b_i]$ to the standard support of the Beta distribution via a linear transformation $z = (x - b_{i-1}) / (b_i - b_{i-1})$, such that the resulting continuous value is recovered via $x = b_{i-1} + z(b_i - b_{i-1})$, where $z \sim \text{Beta}(\alpha_i, \beta_i)$.

The shape parameters α_i and β_i are determined by aligning the mode of the Beta distribution with a representative target value $\tau_i \in [b_{i-1}, b_i]$, such that the probability mass within each bin congregates around τ_i . Defining the normalized location $\gamma_i = (\tau_i - b_{i-1}) / (b_i - b_{i-1})$, and introducing a concentration parameter $c_i = \alpha_i + \beta_i$ to control the spread, we use the mode-based relation $\gamma_i = (\alpha_i - 1) / (\alpha_i + \beta_i - 2)$ to obtain $\alpha_i = 1 + \gamma_i(c_i - 2)$, $\beta_i = 1 + (1 - \gamma_i)(c_i - 2)$. The concentration parameter c_i is selected such that $\int_{0.025}^{0.975} \text{Beta}(z; \alpha_i, \beta_i) dz = 0.99$, ensuring that 99% of the probability mass lies within the central 95% of the normalized interval.

Training Details. ARACNE estimates pairwise gene dependencies by computing Spearman rank-based mutual information, followed by network reconstruction, yielding a weighted adjacency matrix of inferred interactions. In parallel, partial correlations are estimated using a shrinkage Gaussian graphical model implemented in GeneNet, and edge significance is evaluated. A symmetric adjacency matrix is constructed from the resulting partial correlation coefficients, with diagonal elements set to 0. Additionally, regulatory interactions are inferred using GENIE3, a tree-based ensemble method based on random forests, with all genes considered as candidate regulators, 500 trees per target gene, and the number of variables tried at each split set to the square root of the total number of genes. In addition, time-series-based regulatory interactions are inferred using SINCERITIES, which estimates signed gene-gene influences from expression dynamics. It runs in R using `distance = 1` (Kolmogorov-Smirnov distributional distance between time points), `method = 1` (ridge regression for regularization), `noDIAG = 1` (self-regulatory edges not allowed), and `SIGN = 1` (estimation of activation vs repression to obtain a signed adjacency matrix). The resulting adjacency matrix is subsequently normalized by dividing all entries by the maximum edge weight to yield a unit-scaled matrix used for downstream analyses.

For both GeneNet and SINCERITIES, given a predicted weighted adjacency matrix $\hat{\mathbf{A}}$ and the ground-truth signed adjacency matrix \mathbf{A} , we first discretize the predicted interactions by mapping positive weights to +1 (upregulation), negative weights to -1 (downregulation), and zero to 0 (no interaction). Self-interactions are excluded by removing diagonal entries. Performance is then evaluated by comparing the flattened off-diagonal entries of $\hat{\mathbf{A}}$ and \mathbf{A} using macro-averaged precision, recall, and F_1 score over the three classes $\{-1, 0, +1\}$, along with overall accuracy. This metric jointly assesses correct edge detection and regulatory sign assignment. For network edge recovery, we ignore the interaction sign and consider only the presence or absence of edges. Both the predicted and ground-truth adjacency matrices are binarized, with nonzero entries indicating an interaction and zero entries indicating no interaction. Diagonal elements are excluded. Precision, recall, F_1 score, and accuracy are computed by comparing the flattened off-diagonal binary matrices. This metric assesses the ability to accurately recover the network topology, regardless of the regulatory sign.

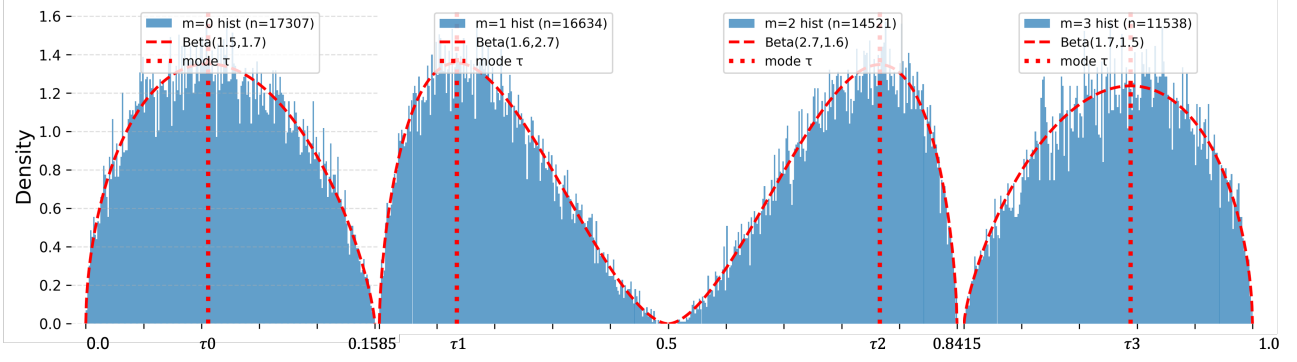


Figure 6: Visualization of continuous value gene expression data generated from discrete QHGM-generated data using localized Beta distributions.

C. Proof of Lemma 2.

Let $\Upsilon := \sum_k \sigma_k \Lambda_k$. We can express the spectral norm of the Hermitian matrix Υ as follows:

$$\begin{aligned} \|\Upsilon\| &= \max\{\lambda_{\max}(\Upsilon), \lambda_{\max}(-\Upsilon)\} \stackrel{a}{\leq} \frac{1}{\theta} \log(\exp\{\theta \lambda_{\max}(\Upsilon)\} + \exp\{\theta \lambda_{\max}(-\Upsilon)\}) \text{ for all } \theta > 0 \\ &\stackrel{b}{\leq} \frac{1}{\theta} \log(\text{tr}(\exp\{\theta \Upsilon\}) + \text{tr}(\exp\{-\theta \Upsilon\})), \end{aligned}$$

where $\lambda_{\max}(\pm \Upsilon)$ denotes the maximum eigenvalue of $\pm \Upsilon$, (a) follows from the LogSumExp inequality [118, Eqn. 4] stated below:

$$\max\{x_1, x_2, \dots, x_m\} \leq \frac{1}{\theta} \log\left(\sum_{i=1}^m \exp(\theta x_i)\right) \leq \max\{x_1, x_2, \dots, x_m\} + \frac{\log n}{\theta} \text{ for all } x_i \in \mathbb{R}, \theta > 0,$$

and (b) follows because $\exp\{\theta \lambda_{\max}(\Upsilon)\} \leq \text{tr}(\exp\{\theta \Upsilon\})$. Next, we take the expectation with respect to Rademacher variables on both sides.

$$\begin{aligned} \mathbb{E}_\sigma[\|\Upsilon\|] &\stackrel{c}{\leq} \frac{1}{\theta} \log(\mathbb{E}[\text{tr} \exp\{\theta \Upsilon\}] + \mathbb{E}[\text{tr} \exp\{-\theta \Upsilon\}]) \\ &\stackrel{d}{\leq} \frac{1}{\theta} \log\left(\text{tr} \exp\left\{\sum_k \log \mathbb{E}[e^{\theta \sigma_k \Lambda_k}]\right\} + \text{tr} \exp\left\{\sum_k \log \mathbb{E}[e^{-\theta \sigma_k \Lambda_k}]\right\}\right) \\ &\stackrel{e}{\leq} \frac{1}{\theta} \log\left(2 \text{tr} \exp\left\{\frac{1}{2} \sum_k \theta^2 \Lambda_k^2\right\}\right) \stackrel{f}{\leq} \frac{1}{\theta} \log\left(2D \exp\left\{\frac{\theta^2}{2} \left\|\sum_k \Lambda_k^2\right\|\right\}\right) = \frac{1}{\theta} \log(2D) + \frac{\theta}{2} \left\|\sum_k \Lambda_k^2\right\|, \end{aligned}$$

where (c) follows from Jensen's inequality, (d) follows from sub-additivity of matrix cumulant generating function [98, Lemma 3.1], (e) is derived using the following results:

- **(Lemma 4.2 [98].)** Suppose A is a fixed Hermitian matrix and σ is a Rademacher variable. Then, for $\theta \in \mathbb{R}$, we have $\mathbb{E}_\sigma[e^{\theta \sigma A}] \leq \exp\{\theta^2 A^2/2\}$ and $\log(\mathbb{E}_\sigma[e^{\theta \sigma A}]) \leq \theta^2 A^2/2$.
- For Hermitian matrices A_1, A_2, B_1, B_2 , if $A_1 \leq B_1$ and $A_2 \leq B_2$, then $A_1 + A_2 \leq B_1 + B_2$.
- $\text{tr} \exp$ (trace-exponential) function is monotone with respect to the semi-definite order [98].

and (f) follows from the inequality $\text{tr}(e^A) \leq d \cdot \exp\{\lambda_{\max}(A)\}$, which holds for all $d \times d$ Hermitian matrix A . Additionally, since Λ_k^2 is a positive semi-definite matrix for each k , it follows that $\lambda_{\max}(\sum_k \Lambda_k^2) = \|\sum_k \Lambda_k^2\|$. Now, by minimizing the right-hand side of the inequality with respect to $\theta > 0$, we get $\theta^* = \sqrt{2 \log(2D) / \|\sum_k \Lambda_k^2\|}$. Finally, this leads us to conclude that

$$\mathbb{E}_\sigma \left[\left\| \sum_k \sigma_k \Lambda_k \right\| \right] \leq \sqrt{2 \log(2D)} \left\| \sum_k \Lambda_k^2 \right\|^{1/2}.$$

D. Proof of Lemma 3.

Following [119, Theorem 3], we recall the parametric derivative formula for the operator exponential:

$$\frac{\partial}{\partial w_k} e^{-A(\mathbf{w})} = - \int_0^1 e^{-(1-s)A(\mathbf{w})} \left(\frac{\partial A(\mathbf{w})}{\partial w_k} \right) e^{-sA(\mathbf{w})} ds, \quad (20)$$

where $A(\mathbf{w})$ is a parameterized Hermitian operator. Using (20), we compute the derivative of $U_t(\mathbf{w}) = e^{-itH(\mathbf{w})}$ with respect to the parameter w_k as follows:

$$\begin{aligned} \frac{\partial}{\partial w_k} U_t(\mathbf{w}) &= - \int_0^1 e^{-(1-s)(itH(\mathbf{w}))} \frac{\partial}{\partial w_k} (itH(\mathbf{w})) e^{-s(itH(\mathbf{w}))} ds \\ &= -it \int_0^1 e^{-(1-s)(itH(\mathbf{w}))} H_k e^{-s(itH(\mathbf{w}))} ds = -i \int_0^t U_t(\mathbf{w}) H_k(s) ds, \end{aligned}$$

where the final equality follows from the change of variables $st \rightarrow s$. Applying the adjoint operation to both sides yields

$$\frac{\partial}{\partial w_k} U_t^\dagger(\mathbf{w}) = +i \int_0^t H_k(s) U_t^\dagger(\mathbf{w}) ds.$$

Now, we compute the derivative of time-evolved state $\rho_t(\mathbf{w}) = U_t \rho_0 U_t^\dagger$ as follows:

$$\begin{aligned} \frac{\partial \rho_t}{\partial w_k} &= \left(\frac{\partial U_t}{\partial w_k} \right) \rho_0 U_t^\dagger + U_t \rho_0 \left(\frac{\partial U_t^\dagger}{\partial w_k} \right) \\ &= -i \int_0^t U_t(\mathbf{w}) H_k(s) \rho_0 U_t^\dagger(\mathbf{w}) ds + i \int_0^t U_t(\mathbf{w}) \rho_0 H_k(s) U_t^\dagger(\mathbf{w}) ds = -i \int_0^t U_t [H_k(s), \rho_0] U_t^\dagger ds. \quad (21) \end{aligned}$$

Therefore,

$$\frac{\partial}{\partial w_k} \text{tr}(\Lambda_{\mathbf{m}} \rho_t) = -i \int_0^t \text{tr}(\Lambda_{\mathbf{m}} U_t [H_k(s), \rho_0] U_t^\dagger) ds = -i \int_0^t \text{tr}(\Lambda_{\mathbf{m}}(t) [H_k(s), \rho_0]) ds,$$

where we used cyclicity of trace and $\Lambda_{\mathbf{m}}(t) := U_t^\dagger \Lambda_{\mathbf{m}} U_t$. Next, we compute the second-order partial derivative as follows:

$$\frac{\partial^2}{\partial w_j \partial w_k} \text{tr}(\Lambda_{\mathbf{m}} \rho_t) = \underbrace{-i \int_0^t \text{tr} \left(\left(\frac{\partial}{\partial w_j} \Lambda_{\mathbf{m}}(t) \right) [H_k(s), \rho_0] \right) ds}_{T_1} \underbrace{-i \int_0^t \text{tr} \left(\Lambda_{\mathbf{m}}(t) \left[\left(\frac{\partial}{\partial w_j} H_k(s) \right), \rho_0 \right] \right) ds}_{T_2}.$$

By applying steps analogous to the derivative of the time-evolved state $\rho_t(\mathbf{w})$ (21), we derive the following:

$$\frac{\partial}{\partial w_j} \Lambda_{\mathbf{m}}(t) = i \int_0^t [H_j(s), \Lambda_{\mathbf{m}}(t)] ds \quad \text{and} \quad \frac{\partial}{\partial w_j} H_k(s) = i \int_0^s [H_j(s_1), H_k(s)] ds_1. \quad (22)$$

This gives,

$$\begin{aligned}
T_1 &= \int_0^t \int_0^t \text{tr}([\mathbf{H}_j(s_2), \Lambda_{\mathbf{m}}(t)] [\mathbf{H}_k(s_1), \rho_0]) \, ds_2 \, ds_1 \\
&\stackrel{a}{=} - \int_0^t \int_0^t \text{tr}(\Lambda_{\mathbf{m}}(t) [\mathbf{H}_j(s_2), [\mathbf{H}_k(s_1), \rho_0]]) \, ds_2 \, ds_1 \\
&\stackrel{b}{=} - \int_0^t \int_0^{s_1} \left(\text{tr}(\Lambda_{\mathbf{m}}(t) [\mathbf{H}_j(s_1), [\mathbf{H}_k(s_2), \rho_0]]) + \text{tr}(\Lambda_{\mathbf{m}}(t) [\mathbf{H}_j(s_2), [\mathbf{H}_k(s_1), \rho_0]]) \right) \, ds_2 \, ds_1, \quad (23)
\end{aligned}$$

where (a) follows from the fact that the trace of the product of two commutators is given by the equation $\text{tr}([A, B][C, D]) = -\text{tr}(B[A, [C, D]])$ and (b) is derived from the fact that for any function $f(s_1, s_2)$, the square integral over the region $[0, t]^2$ can be expressed as follows:

$$\begin{aligned}
\int_0^t \int_0^t f(s_1, s_2) \, ds_2 \, ds_1 &= \int_{0 \leq s_2 \leq s_1 \leq t} f(s_1, s_2) \, ds_2 \, ds_1 + \int_{0 \leq s_1 < s_2 \leq t} f(s_1, s_2) \, ds_2 \, ds_1 \\
&= \int_{0 \leq s_2 \leq s_1 \leq t} (f(s_1, s_2) + f(s_2, s_1)) \, ds_2 \, ds_1 \\
&= \int_0^t \int_0^{s_1} (f(s_1, s_2) + f(s_2, s_1)) \, ds_2 \, ds_1.
\end{aligned}$$

$$\begin{aligned}
T_2 &= \int_0^t \int_0^{s_1} \text{tr}(\Lambda_{\mathbf{m}}(t) [[\mathbf{H}_j(s_2), \mathbf{H}_k(s_1)], \rho_0]) \, ds_2 \, ds_1 \\
&\stackrel{c}{=} \int_0^t \int_0^{s_1} \left(\text{tr}(\Lambda_{\mathbf{m}}(t) [\mathbf{H}_j(s_2), [\mathbf{H}_k(s_1), \rho_0]]) - \text{tr}(\Lambda_{\mathbf{m}}(t) [\mathbf{H}_k(s_1), [\mathbf{H}_j(s_2), \rho_0]]) \right) \, ds_2 \, ds_1, \quad (24)
\end{aligned}$$

where (c) follows from the use of Jacobi identity $[[A, B], C] = [A, [B, C]] - [B, [A, C]]$. Adding T_1 (23) and T_2 (24), we get

$$\begin{aligned}
\frac{\partial^2}{\partial w_j \partial w_k} \text{tr}(\Lambda_{\mathbf{m}} \rho_t) &= - \int_0^t \int_0^{s_1} \text{tr}(\Lambda_{\mathbf{m}}(t) [\mathbf{H}_j(s_1), [\mathbf{H}_k(s_2), \rho_0]]) \, ds_2 \, ds_1 \\
&\quad - \int_0^t \int_0^{s_1} \text{tr}(\Lambda_{\mathbf{m}}(t) [\mathbf{H}_k(s_1), [\mathbf{H}_j(s_2), \rho_0]]) \, ds_2 \, ds_1.
\end{aligned}$$

This completes the first part of Lemma 3. Next, we show gradient and Hessian are bounded. Consider the following inequalities:

$$\begin{aligned}
\left| \frac{\partial}{\partial w_k} \phi(\mathbf{m}|t, \mathbf{w}) \right| &= \left| -i \int_0^t \text{tr}(\Lambda_{\mathbf{m}}(t) [\mathbf{H}_k(s), \rho_0]) \, ds \right| \\
&\leq \int_0^t |\text{tr}(\Lambda_{\mathbf{m}}(t) [\mathbf{H}_k(s), \rho_0])| \, ds && \text{using triangle inequality} \\
&\stackrel{a}{\leq} \int_0^t \|\Lambda_{\mathbf{m}}(t)\| \|\mathbf{H}_k(s), \rho_0\|_1 \, ds \\
&\stackrel{b}{\leq} \int_0^t \|\mathbf{H}_k(s), \rho_0\|_1 \, ds \stackrel{c}{\leq} 2 \int_0^t \|\mathbf{H}_k(s)\| \|\rho_0\|_1 \, ds \leq 2t_{\max} \|\mathbf{H}_k\|,
\end{aligned}$$

where (a) follows from the inequality $|\text{tr}(A^\dagger B)| \leq \|A\| \|B\|_1$ [120, Eqn. 1.174], (b) is derived from the isometric invariance property of spectral norm, i.e., $\|\Lambda_{\mathbf{m}}(t)\| = \|\Lambda_{\mathbf{m}}\|$, along with the fact that $\|\Lambda_{\mathbf{m}}\| \leq 1$,

and (c) follows from Hölder's inequality, which states that for $\frac{1}{p} + \frac{1}{q} = 1$, we have $\|AB\|_1 \leq \|A\|_p \|B\|_q$ (see [120, Eqn. 1.175]). Therefore, we get,

$$\|\nabla_{\mathbf{w}} \phi(\mathbf{m}|t, \mathbf{w})\|_2 \leq \left(4t_{\max}^2 \sum_{k=1}^c \|\mathbf{H}_k\|^2 \right)^{1/2} \leq 2t_{\max} \sqrt{c} \|\mathbf{H}\|_{\infty, \max}.$$

Next, by applying steps analogous to those for the derivative of the likelihood function, we bound its Hessian.

Consider the following inequalities:

$$\begin{aligned} \left| \frac{\partial^2}{\partial w_j \partial w_k} \phi(\mathbf{m}|t, \mathbf{w}) \right| &\leq \left| \int_0^t \int_0^{s_1} \text{tr}(\Lambda_{\mathbf{m}}(t) [\mathbf{H}_j(s_1), [\mathbf{H}_k(s_2), \rho_0]]) \, ds_2 \, ds_1 \right| \\ &\quad + \left| \int_0^t \int_0^{s_1} \text{tr}(\Lambda_{\mathbf{m}}(t) [\mathbf{H}_k(s_1), [\mathbf{H}_j(s_2), \rho_0]]) \, ds_2 \, ds_1 \right| \\ &\leq \int_0^t \int_0^{s_1} \left| \text{tr}(\Lambda_{\mathbf{m}}(t) [\mathbf{H}_j(s_1), [\mathbf{H}_k(s_2), \rho_0]]) \right| \, ds_2 \, ds_1 \\ &\quad + \int_0^t \int_0^{s_1} \left| \text{tr}(\Lambda_{\mathbf{m}}(t) [\mathbf{H}_k(s_1), [\mathbf{H}_j(s_2), \rho_0]]) \right| \, ds_2 \, ds_1 \\ &\stackrel{a}{\leq} \int_0^t \int_0^{s_1} \|\Lambda_{\mathbf{m}}(t)\| \left\| [\mathbf{H}_j(s_1), [\mathbf{H}_k(s_2), \rho_0]] \right\|_1 \, ds_2 \, ds_1 \\ &\quad + \int_0^t \int_0^{s_1} \|\Lambda_{\mathbf{m}}(t)\| \left\| [\mathbf{H}_k(s_1), [\mathbf{H}_j(s_2), \rho_0]] \right\|_1 \, ds_2 \, ds_1 \\ &\stackrel{b}{\leq} 8 \int_0^t \int_0^{s_1} \|\mathbf{H}_k\| \|\mathbf{H}_j\| \, ds_2 \, ds_1 \leq 4t_{\max}^2 \|\mathbf{H}_k\| \|\mathbf{H}_j\| \end{aligned}$$

where (a) follows from [120, Eqn. 1.174], and (b) derives from the matrix Hölder inequality applied to the commutator, leading to $\|[A, B]\| \leq 2\|A\| \|B\|_1$. Thus, we obtain

$$\|\nabla_{\mathbf{w}}^2 \phi(\mathbf{m}|t, \mathbf{w})\| \leq \|\nabla_{\mathbf{w}}^2 \phi(\mathbf{m}|t, \mathbf{w})\|_{\text{F}} = 4t_{\max}^2 \left(\sum_{j,k} \|\mathbf{H}_k\|^2 \|\mathbf{H}_j\|^2 \right)^{1/2} \leq 4t_{\max}^2 c \|\mathbf{H}\|_{\infty, \max}^2,$$

where $\|\cdot\|_{\text{F}}$ is the Frobenius norm.

Since the gradient and the Hessian of the likelihood function are bounded, the likelihood function and its gradient are Lipschitz continuous by definition. Finally, we show the Lipschitz continuity of the Hessian. To this end, define $\mathbf{H}'_k(s) := U_s^\dagger(\mathbf{w}') \mathbf{H}_k U_s(\mathbf{w}')$. Consider the following inequalities:

$$\begin{aligned} &\left| \frac{\partial^2}{\partial w_j \partial w_k} \phi(\mathbf{m}|t, \mathbf{w}) - \frac{\partial^2}{\partial w_j \partial w_k} \phi(\mathbf{m}|t, \mathbf{w}') \right| \\ &\leq \underbrace{\int_0^t \int_0^{s_1} \left| \text{tr} \{ \Lambda_{\mathbf{m}}(U_t(\mathbf{w}) [\mathbf{H}_k(s_1), [\mathbf{H}_j(s_2), \rho_0]]) U_t^\dagger(\mathbf{w}) - U_t(\mathbf{w}') [\mathbf{H}'_k(s_1), [\mathbf{H}'_j(s_2), \rho_0]]) U_t^\dagger(\mathbf{w}') \} \right| \, ds_2 \, ds_1}_{\text{A}_1} \\ &\quad + \underbrace{\int_0^t \int_0^{s_1} \left| \text{tr} \{ \Lambda_{\mathbf{m}}(U_t(\mathbf{w}) [\mathbf{H}_j(s_1), [\mathbf{H}_k(s_2), \rho_0]]) U_t^\dagger(\mathbf{w}) - U_t(\mathbf{w}') [\mathbf{H}'_j(s_1), [\mathbf{H}'_k(s_2), \rho_0]]) U_t^\dagger(\mathbf{w}') \} \right| \, ds_2 \, ds_1}_{\text{A}_2}. \end{aligned}$$

Since A_1 and A_2 are similar except that the indices j and k are reversed, if we set bounds on one, we can similarly bound the other. Without loss of generality, consider A_1 , and then apply [120, Eqn. 1.174].

$$\begin{aligned}
A_1 &\leq \int_0^t \int_0^{s_1} \|U_t(\mathbf{w})[\mathbf{H}_k(s_1), [\mathbf{H}_j(s_2), \rho_0]]U_t^\dagger(\mathbf{w}) - U_t(\mathbf{w}')[\mathbf{H}'_k(s_1), [\mathbf{H}'_j(s_2), \rho_0]]U_t^\dagger(\mathbf{w}')\| ds_2 ds_1 \\
&\stackrel{a}{\leq} \int_0^t \int_0^{s_1} \|U_t(\mathbf{w})[\mathbf{H}_k(s_1), [\mathbf{H}_j(s_2), \rho_0]]U_t^\dagger(\mathbf{w}) - U_t(\mathbf{w}')[\mathbf{H}_k(s_1), [\mathbf{H}_j(s_2), \rho_0]]U_t^\dagger(\mathbf{w}')\| ds_2 ds_1 \\
&\quad + \int_0^t \int_0^{s_1} \|[\mathbf{H}_k(s_1), [\mathbf{H}_j(s_2), \rho_0]] - [\mathbf{H}'_k(s_1), [\mathbf{H}'_j(s_2), \rho_0]]\|_1 ds_2 ds_1 \\
&\stackrel{b}{\leq} \int_0^t \int_0^{s_1} 2\|U_t(\mathbf{w}) - U_t(\mathbf{w}')\| \|[\mathbf{H}_k(s_1), [\mathbf{H}_j(s_2), \rho_0]]\|_1 ds_2 ds_1 \\
&\quad + \int_0^t \int_0^{s_1} \left(\|[\mathbf{H}_k(s_1) - \mathbf{H}'_k(s_1), [\mathbf{H}_j(s_2), \rho_0]]\|_1 + \|[\mathbf{H}'_k(s_1), [\mathbf{H}_j(s_2), \rho_0]] - [\mathbf{H}'_k(s_1), [\mathbf{H}'_j(s_2), \rho_0]]\|_1 \right) ds_2 ds_1,
\end{aligned}$$

where (a) follows by adding and subtracting $U_t(\mathbf{w}')[\mathbf{H}_k(s_1), [\mathbf{H}_j(s_2), \rho_0]]U_t^\dagger(\mathbf{w}')$ and (b) follows by first adding and subtracting $U_t(\mathbf{w})[\mathbf{H}_k(s_1), [\mathbf{H}_j(s_2), \rho_0]]U_t^\dagger(\mathbf{w}')$ and then using [120, Eqn. 1.175]. Next, applying the identity $e^A - e^B = \int_0^1 e^{sA}(A - B)e^{(1-s)B} ds$ [119, Eqn.43], we obtain

$$\|U_t(\mathbf{w}) - U_t(\mathbf{w}')\| \leq t\|\mathbf{H}(\mathbf{w}) - \mathbf{H}(\mathbf{w}')\| \leq t\|\mathbf{H}\|_{\infty, \max} \|\mathbf{w} - \mathbf{w}'\|_1, \quad (25)$$

and using [120, Eqn.1.175] for $p = \infty$ yields

$$\|\mathbf{H}_k(s) - \mathbf{H}'_k(s)\| \leq 2\|\mathbf{H}_j\| \|U_s(\mathbf{w}) - U_s(\mathbf{w}')\| \leq 2s\|\mathbf{H}\|_{\infty, \max}^2 \|\mathbf{w} - \mathbf{w}'\|_1. \quad (26)$$

Using (25) and (26) along with matrix Hölder inequality applied to the commutator, we get

$$\begin{aligned}
A_1 &\leq \int_0^t \int_0^{s_1} 8t\|\mathbf{H}\|_{\infty, \max}^3 \|\mathbf{w} - \mathbf{w}'\|_1 ds_2 ds_1 + \int_0^t \int_0^{s_1} 8(s_1 + s_2)\|\mathbf{H}\|_{\infty, \max}^3 \|\mathbf{w} - \mathbf{w}'\|_1 ds_2 ds_1 \\
&\leq 8t_{\max}^3 \|\mathbf{H}\|_{\infty, \max}^3 \|\mathbf{w} - \mathbf{w}'\|_1.
\end{aligned}$$

Therefore,

$$\begin{aligned}
\left| \frac{\partial^2}{\partial w_j \partial w_k} \phi(\mathbf{m}|t, \mathbf{w}) - \frac{\partial^2}{\partial w_j \partial w_k} \phi(\mathbf{m}|t, \mathbf{w}') \right| &\leq 16t_{\max}^3 \|\mathbf{H}\|_{\infty, \max}^3 \|\mathbf{w} - \mathbf{w}'\|_1 \\
\implies \|\nabla_{\mathbf{w}}^2 \phi(\mathbf{m}|t, \mathbf{w}) - \nabla_{\mathbf{w}}^2 \phi(\mathbf{m}|t, \mathbf{w}')\| &\leq \|\nabla_{\mathbf{w}}^2 \phi(\mathbf{m}|t, \mathbf{w}) - \nabla_{\mathbf{w}}^2 \phi(\mathbf{m}|t, \mathbf{w}')\|_{\text{F}} \\
&\leq 16t_{\max}^3 c^2 \|\mathbf{H}\|_{\infty, \max}^3 \|\mathbf{w} - \mathbf{w}'\|_1 \\
&\leq 16t_{\max}^3 c^{3/2} \|\mathbf{H}\|_{\infty, \max}^3 \|\mathbf{w} - \mathbf{w}'\|_2 = 2L_{\phi}^3 \|\mathbf{w} - \mathbf{w}'\|_2,
\end{aligned}$$

where the last inequality follows from the inequality $\|x\|_1 \leq \sqrt{n}\|x\|$ for $x \in \mathbb{R}^n$. This completes the proof of Lemma 3.

E. Proof of Equation 10

Consider the following inequalities:

$$\begin{aligned} \|\nabla_{\mathbf{w}}^2 \log(\phi(\mathbf{m}|t, \mathbf{w}))\| &= \left\| \frac{\nabla_{\mathbf{w}}^2 \phi(\mathbf{m}|t, \mathbf{w})}{\phi(\mathbf{m}|t, \mathbf{w})} - \frac{\nabla_{\mathbf{w}} \phi(\mathbf{m}|t, \mathbf{w}) \nabla_{\mathbf{w}} \phi(\mathbf{m}|t, \mathbf{w})^\top}{\phi(\mathbf{m}|t, \mathbf{w})^2} \right\| \\ &\leq \left\| \frac{\nabla_{\mathbf{w}}^2 \phi(\mathbf{m}|t, \mathbf{w})}{\phi(\mathbf{m}|t, \mathbf{w})} \right\| + \left\| \frac{\nabla_{\mathbf{w}} \phi(\mathbf{m}|t, \mathbf{w}) \nabla_{\mathbf{w}} \phi(\mathbf{m}|t, \mathbf{w})^\top}{\phi(\mathbf{m}|t, \mathbf{w})^2} \right\| \\ &\stackrel{a}{\leq} \frac{\|\nabla_{\mathbf{w}}^2 \phi(\mathbf{m}|t, \mathbf{w})\|}{p_{\min}} + \frac{\|\nabla_{\mathbf{w}} \phi(\mathbf{m}|t, \mathbf{w})\|^2}{p_{\min}^2} \stackrel{b}{\leq} \frac{L_\phi^2}{p_{\min}} + \frac{L_\phi^2}{p_{\min}^2} \leq \frac{2L_\phi^2}{p_{\min}^2}, \end{aligned}$$

where (a) follows from the fact that for any vector v , the spectral norm of the outer product $\|vv^\top\|$ equals $\|v\|^2$, and (b) follows from Lemma 3. Next, consider the following inequalities:

$$\|\bar{H}_t(\mathbf{w})\| \stackrel{c}{\leq} \mathbb{E}_{\mathbf{m} \sim \phi(\cdot|t, \mathbf{w}^*)} \|\nabla_{\mathbf{w}}^2 \log(\phi(\mathbf{m}|t, \mathbf{w}))\| \leq \frac{2L_\phi^2}{p_{\min}^2},$$

where (c) follows from Jensen's inequality.

F. Proof of Proposition 1

For a given t_i , the random matrices $\hat{H}_{(i,k)}(\mathbf{w})$ are independent satisfying $\mathbb{E}_{\phi(\cdot|t_i, \mathbf{w}^*)} [\hat{H}_{(i,k)}(\mathbf{w})] = \bar{H}_{t_i}(\mathbf{w})$, and from Eqn. (10), $\|\hat{H}_{(i,k)}(\mathbf{w})\| \leq 2(L_\phi/p_{\min})^2$. Therefore, using Lemma 1, we obtain, for all $\varepsilon_1 > 0$,

$$\Pr \left\{ \left\| \frac{1}{N_c} \sum_{k=1}^{N_c} \hat{H}_{(i,k)}(\mathbf{w}) - \bar{H}_{t_i}(\mathbf{w}) \right\| \geq \varepsilon_1 \right\} \leq 2c \cdot \exp \left\{ \frac{-N_c \varepsilon_1^2/2}{\sigma_i^2 + 4\varepsilon_1 L_\phi^2/3p_{\min}^2} \right\},$$

where $\sigma_i^2 := \|\mathbb{E}_{\phi(\cdot|t_i, \mathbf{w}^*)} [(\hat{H}_{(i,k)}(\mathbf{w}))^2]\|$. Applying the union bound, we get

$$\begin{aligned} \Pr \left\{ \max_{1 \leq i \leq N_t} \|\hat{H}_{t_i}(\mathbf{w}) - \bar{H}_{t_i}(\mathbf{w})\| \geq \varepsilon_1 \right\} &= \Pr \left\{ \bigcup_{i=1}^{N_t} \{\|\hat{H}_{t_i}(\mathbf{w}) - \bar{H}_{t_i}(\mathbf{w})\| \geq \varepsilon_1\} \right\} \\ &\leq 2c N_t \exp \left\{ \frac{-N_c \varepsilon_1^2/2}{\sigma_{\max}^2 + 4\varepsilon_1 L_\phi^2/3p_{\min}^2} \right\}. \end{aligned}$$

It remains to bound $\sigma_{\max}^2 := \max_i \sigma_i^2$, which we do next using Lemma 3. Consider the following inequalities:

$$\sigma_i^2 \leq \mathbb{E}_{\phi(\cdot|t_i, \mathbf{w}^*)} \left\| (\nabla_{\mathbf{w}}^2 \log(\phi(\mathbf{m}_{(i,k)}|t_i, \mathbf{w})))^2 \right\| = \mathbb{E}_{\phi(\cdot|t_i, \mathbf{w}^*)} \left\| \nabla_{\mathbf{w}}^2 \log(\phi(\mathbf{m}_{(i,k)}|t_i, \mathbf{w})) \right\|^2 \leq 4(L_\phi/p_{\min})^4,$$

where the equality follows from the property that for any Hermitian matrix A , it holds that $\|A^2\| = \|A\|^2$ and the last inequality follows from Eqn.(10). Hence, $\sigma_{\max}^2 \leq 4(L_\phi/p_{\min})^4$. This completes the bound on T_1 . We next bound T_2 , which captures the deviation of the per-time expected Hessian from the expected Hessian. Observe that the random matrices $\bar{H}_{t_i}(\mathbf{w})$ are independent satisfying $\mathbb{E}_{t_i} [\bar{H}_{t_i}(\mathbf{w})] = \bar{H}(\mathbf{w})$, and using (10) $\|\bar{H}_{t_i}(\mathbf{w})\| \leq 2(L_\phi/p_{\min})^2$. Therefore, applying Lemma 1, we obtain, for all $\varepsilon_2 > 0$,

$$\Pr \left\{ \left\| \frac{1}{N_t} \sum_{i=1}^{N_t} \bar{H}_{t_i}(\mathbf{w}) - \bar{H}(\mathbf{w}) \right\| \geq \varepsilon_2 \right\} \leq 2c \cdot \exp \left\{ \frac{-N_c \varepsilon_2^2/2}{\sigma^2 + 2\varepsilon_2 L_\phi^2/3p_{\min}^2} \right\},$$

where $\sigma^2 := \|\mathbb{E}_{t \sim \pi} [(\bar{H}_t(\mathbf{w}))^2]\| \leq 4(L_\phi/p_{\min})^4$. This completes the proof of Proposition 1.

G. Proof of Proposition 2

Define $s(\mathbf{m}, t, \mathbf{w}) := -\nabla_{\mathbf{w}}^2 \log(\phi(\mathbf{m}|t, \mathbf{w}))$, which can be simplified as

$$s(\mathbf{m}, t, \mathbf{w}) = \frac{\nabla_{\mathbf{w}}\phi(\mathbf{m}|t, \mathbf{w})\nabla_{\mathbf{w}}\phi(\mathbf{m}|t, \mathbf{w})^\top}{\phi(\mathbf{m}|t, \mathbf{w})^2} - \frac{\nabla_{\mathbf{w}}^2\phi(\mathbf{m}|t, \mathbf{w})}{\phi(\mathbf{m}|t, \mathbf{w})}.$$

For every $\mathbf{m} \in \mathcal{M}^n$ and $t \in (0, t_{\max}]$, consider the following inequalities:

$$\begin{aligned} & \|s(\mathbf{m}, t, \mathbf{w}) - s(\mathbf{m}, t, \mathbf{w}')\| \\ & \leq \left\| \frac{\nabla_{\mathbf{w}}\phi(\mathbf{m}|t, \mathbf{w})\nabla_{\mathbf{w}}\phi(\mathbf{m}|t, \mathbf{w})^\top}{\phi(\mathbf{m}|t, \mathbf{w})^2} - \frac{\nabla_{\mathbf{w}}\phi(\mathbf{m}|t, \mathbf{w}')\nabla_{\mathbf{w}}\phi(\mathbf{m}|t, \mathbf{w}')^\top}{\phi(\mathbf{m}|t, \mathbf{w}')^2} \right\| + \left\| \frac{\nabla_{\mathbf{w}}^2\phi(\mathbf{m}|t, \mathbf{w})}{\phi(\mathbf{m}|t, \mathbf{w})} - \frac{\nabla_{\mathbf{w}}^2\phi(\mathbf{m}|t, \mathbf{w}')}{\phi(\mathbf{m}|t, \mathbf{w}')} \right\| \\ & \leq \frac{1}{\phi(\mathbf{m}|t, \mathbf{w})^2} \|\nabla_{\mathbf{w}}\phi(\mathbf{m}|t, \mathbf{w})\nabla_{\mathbf{w}}\phi(\mathbf{m}|t, \mathbf{w})^\top - \nabla_{\mathbf{w}}\phi(\mathbf{m}|t, \mathbf{w}')\nabla_{\mathbf{w}}\phi(\mathbf{m}|t, \mathbf{w}')^\top\| \\ & \quad + \|\nabla_{\mathbf{w}}\phi(\mathbf{m}|t, \mathbf{w}')\|^2 \frac{|\phi(\mathbf{m}|t, \mathbf{w})^2 - \phi(\mathbf{m}|t, \mathbf{w}')^2|}{(\phi(\mathbf{m}|t, \mathbf{w})\phi(\mathbf{m}|t, \mathbf{w}'))^2} + \|\nabla_{\mathbf{w}}^2\phi(\mathbf{m}|t, \mathbf{w}')\| \frac{|\phi(\mathbf{m}|t, \mathbf{w}) - \phi(\mathbf{m}|t, \mathbf{w}')|}{\phi(\mathbf{m}|t, \mathbf{w})\phi(\mathbf{m}|t, \mathbf{w}')} \\ & \quad + \frac{1}{\phi(\mathbf{m}|t, \mathbf{w})} \|\nabla_{\mathbf{w}}^2\phi(\mathbf{m}|t, \mathbf{w}) - \nabla_{\mathbf{w}}^2\phi(\mathbf{m}|t, \mathbf{w}')\| \\ & \leq \frac{1}{p_{\min}^2} \|\nabla_{\mathbf{w}}\phi(\mathbf{m}|t, \mathbf{w})\nabla_{\mathbf{w}}\phi(\mathbf{m}|t, \mathbf{w})^\top - \nabla_{\mathbf{w}}\phi(\mathbf{m}|t, \mathbf{w}')\nabla_{\mathbf{w}}\phi(\mathbf{m}|t, \mathbf{w}')^\top\| \\ & \quad + 2\frac{L_\phi^3}{p_{\min}^3} \|\mathbf{w} - \mathbf{w}'\| + \frac{L_\phi^3}{p_{\min}^2} \|\mathbf{w} - \mathbf{w}'\| + 2\frac{L_\phi^3}{p_{\min}} \|\mathbf{w} - \mathbf{w}'\| \\ & \leq \frac{1}{p_{\min}^2} \|\nabla_{\mathbf{w}}\phi(\mathbf{m}|t, \mathbf{w}) - \nabla_{\mathbf{w}}\phi(\mathbf{m}|t, \mathbf{w}')\| (\|\nabla_{\mathbf{w}}\phi(\mathbf{m}|t, \mathbf{w})\| + \|\nabla_{\mathbf{w}}\phi(\mathbf{m}|t, \mathbf{w}')\|) + \frac{5L_\phi^3}{p_{\min}^3} \|\mathbf{w} - \mathbf{w}'\| \\ & \leq \frac{2L_\phi^3}{p_{\min}^2} \|\mathbf{w} - \mathbf{w}'\| + \frac{5L_\phi^3}{p_{\min}^3} \|\mathbf{w} - \mathbf{w}'\| \leq \frac{7L_\phi^3}{p_{\min}^3} \|\mathbf{w} - \mathbf{w}'\|. \end{aligned}$$

where the fourth inequality follows by adding and subtracting $\nabla_{\mathbf{w}}\phi(\mathbf{m}|t, \mathbf{w})\nabla_{\mathbf{w}}\phi(\mathbf{m}|t, \mathbf{w}')^\top$ and using the fact that for any vectors a and $b \in \mathbb{R}^n$, we have $\|ab^\top\| = \|a\|\|b\|$. We are now equipped to bound the following:

$$\begin{aligned} \|\widehat{H}(\mathbf{w}) - \widehat{H}(\mathbf{w}')\| & = \left\| \frac{1}{N_t} \sum_{i=1}^{N_t} \frac{1}{N_c} \sum_{k=1}^{N_c} s(\mathbf{m}_{(i,k)}, t_i, \mathbf{w}) - \frac{1}{N_t} \sum_{i=1}^{N_t} \frac{1}{N_c} \sum_{k=1}^{N_c} s(\mathbf{m}_{(i,k)}, t_i, \mathbf{w}') \right\| \\ & \leq \frac{1}{N_t} \sum_{i=1}^{N_t} \frac{1}{N_c} \sum_{k=1}^{N_c} \|s(\mathbf{m}_{(i,k)}, t_i, \mathbf{w}) - s(\mathbf{m}_{(i,k)}, t_i, \mathbf{w}')\| \leq \frac{7L_\phi^3}{p_{\min}^3} \|\mathbf{w} - \mathbf{w}'\|. \end{aligned}$$

Next, applying the similar inequalities as above, we obtain $\|\bar{H}(\mathbf{w}) - \bar{H}(\mathbf{w}')\| \leq 7(L_\phi/p_{\min})^3 \|\mathbf{w} - \mathbf{w}'\|$.

H. Equivalent Conditions of Strong Convexity

We state a well-known result on the equivalence conditions of strongly convexity here for convenience [76, Exercise 9.9].

Lemma 4 (Strong convexity). *Let $f : \mathbb{R}^n \rightarrow \mathbb{R}$ be twice continuously differentiable and let $\Omega \subset \mathbb{R}^n$ be a compact set. Then f is μ -strongly convex on Ω if and only if any of the following equivalent conditions hold:*

- (i) For all $x, y \in \Omega$, $f(x) \geq f(y) + \nabla f(y)^\top(x - y) + \frac{\mu}{2}\|x - y\|^2$.
(ii) For all $x, y \in \Omega$, $(\nabla f(x) - \nabla f(y))^\top(x - y) \geq \mu\|x - y\|^2$.
(iii) For all $z \in \Omega$, $\nabla^2 f(z) \succeq \mu I$.

Proof. We prove the equivalence by establishing the implications (i) \Rightarrow (ii) \Rightarrow (iii) \Rightarrow (ii) \Rightarrow (i).

(i) \Rightarrow (ii). Applying (i) to the ordered pairs (x, y) and (y, x) yields

$$\begin{aligned} f(x) &\geq f(y) + \nabla f(y)^\top(x - y) + \frac{\mu}{2}\|x - y\|^2, \\ f(y) &\geq f(x) + \nabla f(x)^\top(y - x) + \frac{\mu}{2}\|x - y\|^2. \end{aligned}$$

Summing these two inequalities gives $(\nabla f(x) - \nabla f(y))^\top(x - y) \geq \mu\|x - y\|^2$.

(ii) \Rightarrow (iii). Fix $z \in B(x_0, r)$ and an arbitrary direction $v \in B(x_0, r)$. Applying (ii) with $x = z + tv$ and $y = z$ gives

$$(\nabla f(z + tv) - \nabla f(z))^\top tv \geq \mu t^2 \|v\|^2 \quad \text{for all } t > 0.$$

After dividing both sides by t^2 gives

$$\left(\frac{\nabla f(z + tv) - \nabla f(z)}{t} \right)^\top v \geq \mu \|v\|^2 \quad \text{for all } t > 0.$$

Since ∇f is differentiable at z , its derivative at z is given by the Hessian matrix $\nabla^2 f(z)$. In particular, for any direction $v \in B(x_0, r)$, the directional derivative of the gradient satisfies

$$\lim_{t \rightarrow 0} \frac{\nabla f(z + tv) - \nabla f(z)}{t} = \nabla^2 f(z) v.$$

Taking the limit $t \rightarrow 0$ in the preceding inequality therefore yields $v^\top \nabla^2 f(z) v \geq \mu \|v\|^2$. Since this inequality holds for every $v \in B(x_0, r)$, it follows that the symmetric matrix $\nabla^2 f(z) - \mu I$ is positive semidefinite. Equivalently, $\nabla^2 f(z) \succeq \mu I$. As z was arbitrary, the result holds for all $z \in B(x_0, r)$.

(iii) \Rightarrow (ii). Consider the line segment $\gamma(t) = y + t(x - y)$ for $t \in [0, 1]$. By the fundamental theorem of calculus applied to the gradient,

$$\nabla f(x) - \nabla f(y) = \int_0^1 \nabla^2 f(\gamma(t)) \gamma'(t) dt.$$

Taking the inner product with $\gamma'(t) = (x - y)$ and using (iii), we obtain

$$(\nabla f(x) - \nabla f(y))^\top \gamma'(t) = \int_0^1 (x - y)^\top \nabla^2 f(\gamma(t)) (x - y) dt \geq \int_0^1 \mu \|x - y\|^2 dt = \mu \|x - y\|^2.$$

(ii) \Rightarrow (i). Consider the line segment $\gamma(t) = y + t(x - y)$ for $t \in [0, 1]$. By the fundamental theorem of calculus,

$$f(x) - f(y) = \int_0^1 \nabla f(\gamma(t))^\top \gamma'(t) dt = \int_0^1 \nabla f(y + t(x - y))^\top (x - y) dt.$$

Using (ii) with the pair $(y + t(x - y), y)$ yields

$$(\nabla f(y + t(x - y)) - \nabla f(y))^\top (x - y) \geq \mu t \|x - y\|^2,$$

for all $t \in [0, 1]$. Substituting this bound into the integral representation above gives

$$f(x) - f(y) \geq \int_0^1 (\nabla f(y)^\top (x - y) + \mu t \|x - y\|^2) dt = \nabla f(y)^\top (x - y) + \frac{\mu}{2} \|x - y\|^2.$$

This completes the proof. \square

I. Derivation of Equation (18)

We use the well-known McDiarmids inequality [76, Corollary 2.21] [99, Lemma 26.4]. Define the function,

$$f(\mathcal{S}_i) = \sup_{\mathbf{w} \in \mathcal{W}_B} |\widehat{L}_{t_i}(\mathbf{w}; \mathcal{S}_i) - L_{t_i}(\mathbf{w})|,$$

where $\mathcal{S}_i = \{\mathbf{m}_{(i,1)}, \dots, \mathbf{m}_{(i,N_c)}\}$ and $\widehat{L}_{t_i}(\mathbf{w}; \mathcal{S}_i) := \frac{1}{N_c} \sum_k \ell(\phi(\mathbf{m}_{(i,k)} | t_i, \mathbf{w}))$. Let $\mathcal{S}'_i = \{\mathbf{m}_{(i,1)}, \dots, \mathbf{m}'_{(i,j)}, \dots, \mathbf{m}_{(i,N_c)}\}$ differ from \mathcal{S}_i in only one coordinate. Then,

$$\begin{aligned} |f(\mathcal{S}_i) - f(\mathcal{S}'_i)| &= \left| \sup_{\mathbf{w} \in \mathcal{W}_B} |\widehat{L}_{t_i}(\mathbf{w}; \mathcal{S}_i) - L_{t_i}(\mathbf{w})| - \sup_{\mathbf{w} \in \mathcal{W}_B} |\widehat{L}_{t_i}(\mathbf{w}; \mathcal{S}'_i) - L_{t_i}(\mathbf{w})| \right| \\ &\leq \sup_{\mathbf{w} \in \mathcal{W}_B} \left| |\widehat{L}_{t_i}(\mathbf{w}; \mathcal{S}_i) - L_{t_i}(\mathbf{w})| - |\widehat{L}_{t_i}(\mathbf{w}; \mathcal{S}'_i) - L_{t_i}(\mathbf{w})| \right| \\ &\leq \sup_{\mathbf{w} \in \mathcal{W}_B} \left| \widehat{L}_{t_i}(\mathbf{w}; \mathcal{S}_i) - \widehat{L}_{t_i}(\mathbf{w}; \mathcal{S}'_i) \right| \leq \frac{1}{N_c} \sup_{\mathbf{w} \in \mathcal{W}_B} |\ell(\phi(\mathbf{m}_{(i,j)} | t_i, \mathbf{w})) - \ell(\phi(\mathbf{m}'_{(i,j)} | t_i, \mathbf{w}))|, \end{aligned}$$

where the second inequality follows from the following result: for bounded functions $g_1, g_2 : \mathcal{X} \rightarrow \mathbb{R}$, we have $|\sup_{\mathcal{X}} g_1 - \sup_{\mathcal{X}} g_2| \leq \sup_{\mathcal{X}} |g_1 - g_2|$, and the third inequality follows the reverse triangle inequality. Since $|\log x - \log y| \leq \log(1/a)$, for all $a \leq x, y \leq 1$, we get $|f(\mathcal{S}_i) - f(\mathcal{S}'_i)| \leq (-\log p_{\min})/N_c$. This means f satisfies the bounded-difference condition of McDiarmid's inequality with $c_j = (-\log p_{\min})/N_c$ for all $k \in \{1, 2, \dots, N_c\}$. Therefore, using McDiarmid's inequality, for any $\varepsilon > 0$,

$$\Pr \{|f(\mathcal{S}_i) - \mathbb{E}[f(\mathcal{S}_i)]| \geq \varepsilon\} \leq 2 \exp \left\{ \frac{-2\varepsilon^2 N_c}{(-\log p_{\min})^2} \right\}.$$

Applying the union bound gives

$$\Pr \left\{ \max_i |f(\mathcal{S}_i) - \mathbb{E}[f(\mathcal{S}_i)]| \geq \varepsilon \right\} = \Pr \left\{ \bigcup_{i=1}^{N_t} \{|f(\mathcal{S}_i) - \mathbb{E}[f(\mathcal{S}_i)]| \geq \varepsilon\} \right\} \leq 2N_t \exp \left\{ \frac{-2\varepsilon^2 N_c}{(-\log p_{\min})^2} \right\}.$$

This yields, for any $\delta_1 \in (0, 1)$, with probability at least $(1 - \delta_1)$,

$$\begin{aligned} \max_i \sup_{\mathbf{w} \in \mathcal{W}_B} |\widehat{L}_{t_i}(\mathbf{w}) - L_{t_i}(\mathbf{w})| &\leq \max_i \mathbb{E} \left[\sup_{\mathbf{w} \in \mathcal{W}_B} |\widehat{L}_{t_i}(\mathbf{w}) - L_{t_i}(\mathbf{w})| \right] + (-\log p_{\min}) \sqrt{\frac{2 \log(2N_t/\delta_1)}{N_c}} \\ &\leq \max_i 2 \mathbb{E}[\widehat{\mathfrak{R}}_{\mathcal{S}_i}(\mathcal{L}_{\mathbf{m}}^{(i)})] + (-\log p_{\min}) \sqrt{\frac{\log(2N_t/\delta_1)}{2N_c}}, \end{aligned} \quad (27)$$

where the last inequality follows from [99, Lemma 26.2]. Next, we apply the bounded-difference property to the empirical Rademacher complexity. With \mathcal{S}'_i as stated above, we have

$$\begin{aligned} |\hat{\mathfrak{R}}_{\mathcal{S}_i}(\mathcal{L}_{\mathbf{m}}^{(i)}) - \hat{\mathfrak{R}}_{\mathcal{S}'_i}(\mathcal{L}_{\mathbf{m}}^{(i)})| &= \left| \mathbb{E}_{\sigma} \sup_{\mathbf{w} \in \mathcal{W}_B} \frac{1}{N_c} \sum_{k=1}^{N_c} \sigma_{(i,k)} \ell(\phi(\mathbf{m}_{(i,k)}|t_i, \mathbf{w})) \right. \\ &\quad \left. - \mathbb{E}_{\sigma} \sup_{\mathbf{w} \in \mathcal{W}_B} \frac{1}{N_c} \left(\sum_{k \neq j} \sigma_{(i,k)} \ell(\phi(\mathbf{m}_{(i,k)}|t_i, \mathbf{w})) + \sigma_{(i,j)} \ell(\phi(\mathbf{m}'_{(i,j)}|t_i, \mathbf{w})) \right) \right| \\ &\leq \mathbb{E}_{\sigma} \sup_{\mathbf{w} \in \mathcal{W}_B} \frac{1}{N_c} |\sigma_{(i,j)} (\ell(\phi(\mathbf{m}_{(i,j)}|t_i, \mathbf{w})) - \ell(\phi(\mathbf{m}'_{(i,j)}|t_i, \mathbf{w})))| \\ &= \frac{1}{N_c} \sup_{\mathbf{w} \in \mathcal{W}_B} |\ell(\phi(\mathbf{m}_{(i,j)}|t_i, \mathbf{w})) - \ell(\phi(\mathbf{m}'_{(i,j)}|t_i, \mathbf{w}))| \leq \frac{(-\log p_{\min})}{N_c}. \end{aligned}$$

Thus, $\hat{\mathfrak{R}}_{\mathcal{S}_i}(\mathcal{L}_{\mathbf{m}}^{(i)})$ satisfies bounded differences with $c_j = -\log p_{\min}/N_c$. By McDiarmid's inequality, for any $\varepsilon > 0$

$$\Pr \left\{ \left| \hat{\mathfrak{R}}_{\mathcal{S}_i}(\mathcal{L}_{\mathbf{m}}^{(i)}) - \mathbb{E}[\hat{\mathfrak{R}}_{\mathcal{S}_i}(\mathcal{L}_{\mathbf{m}}^{(i)})] \right| \geq \varepsilon \right\} \leq 2 \exp \left\{ \frac{-2\varepsilon^2 N_c}{(-\log p_{\min})^2} \right\}.$$

Applying the union bound, we get,

$$\Pr \left\{ \max_i \left| \hat{\mathfrak{R}}_{\mathcal{S}_i}(\mathcal{L}_{\mathbf{m}}^{(i)}) - \mathbb{E}[\hat{\mathfrak{R}}_{\mathcal{S}_i}(\mathcal{L}_{\mathbf{m}}^{(i)})] \right| \geq \varepsilon \right\} \leq 2N_t \exp \left\{ \frac{-2\varepsilon^2 N_c}{(-\log p_{\min})^2} \right\}.$$

Therefore, for any $\delta_2 \in (0, 1)$, with probability at least $(1 - \delta_2)$, we have

$$\max_i \mathbb{E}[\hat{\mathfrak{R}}_{\mathcal{S}_i}(\mathcal{L}_{\mathbf{m}}^{(i)})] \leq \max_i \hat{\mathfrak{R}}_{\mathcal{S}_i}(\mathcal{L}_{\mathbf{m}}^{(i)}) + (-\log p_{\min}) \sqrt{\frac{\log(2N_t/\delta_2)}{2N_c}}.$$

Finally, by letting $\delta_1 = \delta_2 = \delta$, we obtain

$$\max_{1 \leq i \leq N_t} \sup_{\mathbf{w} \in \mathcal{W}_B} T_1^{(i)}(\mathbf{w}) \leq \max_i 2 \hat{\mathfrak{R}}_{\mathcal{S}_i}(\mathcal{L}_{\mathbf{m}}^{(i)}) + 3(-\log p_{\min}) \sqrt{\frac{\log(2N_t/\delta)}{2N_c}},$$

which holds with probability at least $(1 - 2\delta)$.

J. Derivation of Equation (19)

We use the well-known McDiarmids inequality [76, Corollary 2.21] [99, Lemma 26.4]. Define the function,

$$f(\mathcal{T}) = \sup_{\mathbf{w} \in \mathcal{W}_B} \left| \frac{1}{N_t} \sum_{i=1}^{N_t} L_{t_i}(\mathbf{w}) - L(\mathbf{w}) \right|,$$

Let $\mathcal{T}' = \{t_i, \dots, t'_j, \dots, t_{N_c}\}$ differ from \mathcal{T} in only one coordinate. Then,

$$\begin{aligned} |f(\mathcal{T}) - f(\mathcal{T}')| &\leq \frac{1}{N_t} \sup_{\mathbf{w} \in \mathcal{W}_B} \left| \mathbb{E}_{\mathbf{m} \sim \phi(\cdot|t_j, \mathbf{w}^*)} [\ell(\phi(\mathbf{m}|t_j, \mathbf{w}))] - \mathbb{E}_{\mathbf{m} \sim \phi(\cdot|t'_j, \mathbf{w}^*)} [\ell(\phi(\mathbf{m}|t'_j, \mathbf{w}))] \right| \\ &\leq \frac{1}{N_t} \sup_{\mathbf{w} \in \mathcal{W}_B} \left| \mathbb{E}_{\mathbf{m} \sim \phi(\cdot|t_j, \mathbf{w}^*)} [\ell(\phi(\mathbf{m}|t_j, \mathbf{w}))] \right| + \frac{1}{N_t} \sup_{\mathbf{w} \in \mathcal{W}_B} \left| \mathbb{E}_{\mathbf{m} \sim \phi(\cdot|t'_j, \mathbf{w}^*)} [\ell(\phi(\mathbf{m}|t'_j, \mathbf{w}))] \right| \\ &\leq 2(-\log p_{\min})/N_t. \end{aligned}$$

Therefore, applying McDiarmid's inequality and [99, Lemma 26.2] gives, for any $\delta_1 \in (0, 1)$, with probability at least $(1 - \delta_1)$,

$$\sup_{\mathbf{w} \in \mathcal{W}_B} \left| \frac{1}{N_t} \sum_{i=1}^{N_t} L_{t_i}(\mathbf{w}) - L(\mathbf{w}) \right| \leq 2 \mathbb{E}[\hat{\mathfrak{R}}_{\mathcal{T}}(\mathcal{L}_t)] + (-\log p_{\min}) \sqrt{\frac{\log(2/\delta_1)}{2N_t}}, \quad (28)$$

Next, we apply the bounded-difference property to the empirical Rademacher complexity. With \mathcal{S}'_i as stated above, we have

$$\begin{aligned} |\hat{\mathfrak{R}}_{\mathcal{T}}(\mathcal{L}_t) - \hat{\mathfrak{R}}_{\mathcal{T}'}(\mathcal{L}_t)| &= \left| \mathbb{E}_{\sigma} \sup_{\mathbf{w} \in \mathcal{W}_B} \frac{1}{N_t} \sum_{i=1}^{N_t} \sigma_i L_{t_i}(\mathbf{w}) - \mathbb{E}_{\sigma} \sup_{\mathbf{w} \in \mathcal{W}_B} \frac{1}{N_t} \left(\sum_{i \neq j} \sigma_i L_{t_i}(\mathbf{w}) + \sigma_j L_{t'_j}(\mathbf{w}) \right) \right| \\ &\leq \mathbb{E}_{\sigma} \sup_{\mathbf{w} \in \mathcal{W}_B} \frac{1}{N_t} |\sigma_j (L_{t_j}(\mathbf{w}) - L_{t'_j}(\mathbf{w}))| \leq 2(-\log p_{\min})/N_t. \end{aligned}$$

Thus, $\hat{\mathfrak{R}}_{\mathcal{T}}(\mathcal{L}_t)$ satisfies bounded differences with $c_j = -\log p_{\min}/N_c$. By McDiarmid's inequality [76, Corollary 2.21] [99, Lemma 26.4], we obtain, for any $\delta_2 \in (0, 1)$, with probability at least $(1 - \delta_2)$, we have

$$\mathbb{E}[\hat{\mathfrak{R}}_{\mathcal{T}}(\mathcal{L}_t)] \leq \hat{\mathfrak{R}}_{\mathcal{T}}(\mathcal{L}_t) + (-\log p_{\min}) \sqrt{\frac{2 \log(2/\delta_2)}{N_c}}.$$

Finally, by letting $\delta_1 = \delta_2 = \delta$, we obtain

$$\sup_{\mathbf{w} \in \mathcal{W}_B} T_2(\mathbf{w}) \leq 2 \hat{\mathfrak{R}}_{\mathcal{T}}(\mathcal{L}_t) + 3(-\log p_{\min}) \sqrt{\frac{2 \log(2/\delta)}{N_t}},$$

which holds with probability at least $(1 - 2\delta)$.

K. Proof of Proposition 3.

Using the definition of empirical Rademacher complexity and the contraction lemma [99, Lemma 26.9], we get

$$\hat{\mathfrak{R}}_{\mathcal{S}_i}(\mathcal{L}_{\mathbf{m}}^{(i)}) = \mathbb{E}_{\sigma} \left[\sup_{\mathbf{w} \in \mathcal{W}_B} \frac{1}{N_c} \sum_{k=1}^{N_c} \sigma_{(i,k)} \ell(\phi(\mathbf{m}_{(i,k)} | t_i, \mathbf{w})) \right] \leq \frac{1}{p_{\min}} \mathbb{E}_{\sigma} \left[\sup_{\mathbf{w} \in \mathcal{W}_B} \frac{1}{N_c} \sum_{k=1}^{N_c} \sigma_{(i,k)} \text{tr}(\Lambda_{\mathbf{m}_{(i,k)}} \rho_{t_i}(\mathbf{w})) \right],$$

where the inequality follows by noting that ℓ is $1/p_{\min}$ -Lipschitz. Next, by grouping the terms within the trace, we get

$$\sum_k \sigma_{(i,k)} \text{tr}(\Lambda_{\mathbf{m}_{(i,k)}} \rho_{t_i}(\mathbf{w})) = \text{tr} \left(\left(\sum_k \sigma_{(i,k)} \Lambda_{\mathbf{m}_{(i,k)}} \right) \rho_{t_i}(\mathbf{w}) \right).$$

Applying the inequality $|\text{tr}(A^\dagger B)| \leq \|A\| \|B\|_1$ [120, Eqn. 1.174], gives

$$\sup_{\mathbf{w} \in \mathcal{W}_B} \text{tr} \left(\left(\sum_k \sigma_{(i,k)} \Lambda_{\mathbf{m}_{(i,k)}} \right) \rho_{t_i}(\mathbf{w}) \right) \leq \sup_{\mathbf{w} \in \mathcal{W}_B} \left\| \sum_k \sigma_{(i,k)} \Lambda_{\mathbf{m}_{(i,k)}} \right\| \|\rho_{t_i}(\mathbf{w})\|_1 = \frac{1}{N_c} \left\| \sum_k \sigma_{(i,k)} \Lambda_{\mathbf{m}_{(i,k)}} \right\|.$$

Taking expectation and using Lemma 2 for each t , we get

$$\hat{\mathfrak{R}}_{\mathcal{S}_i}(\mathcal{L}_{\mathbf{m}}^{(i)}) \leq \frac{\sqrt{2 \log(2D)}}{p_{\min} N_c} \left\| \sum_k \Lambda_{\mathbf{m}_{(i,k)}}^2 \right\|^{1/2}.$$

Finally, using triangle inequality, $\sqrt{\|\sum_k \Lambda_{\mathbf{m}(i,k)}^2\|} \leq \sqrt{\sum_k \|\Lambda_{\mathbf{m}(i,k)}^2\|} \leq \sqrt{N_c}$ since $0 \leq \Lambda_{\mathbf{m}} \leq \mathbf{I}$. Thus,

$$\hat{\mathfrak{R}}_{\mathcal{S}_i}(\mathcal{L}_{\mathbf{m}}^{(i)}) \leq \frac{\sqrt{2 \log(2D)}}{p_{\min} N_c} \sqrt{N_c} = \frac{\sqrt{2 \log(2D)}}{p_{\min} \sqrt{N_c}}.$$

This completes the proof of Proposition 3.

L. Proof of Proposition 4.

Recall, for a metric space (\mathcal{X}, d) , the covering number, denoted as $\mathcal{N}(\varepsilon, \mathcal{X}, d)$, is the minimum number of balls of radius ε required to cover the given space \mathcal{X} using metric d . Note that for c -dimensional Euclidean ball of radius B , the covering $\mathcal{N}(\eta, \mathcal{W}_B, \|\cdot\|_2)$ is upper bounded as: $\mathcal{N}(\eta, \mathcal{W}_B, \|\cdot\|_2) \leq \left(\frac{3B}{\eta}\right)^c$. Next, on the sample $\mathcal{T} = \{t_1, \dots, t_{N_t}\}$, define a data-dependent pseudo-metric on function L_{t_i}

$$d_{\mathcal{T}}(\mathbf{w}, \mathbf{w}') := \left(\frac{1}{N_t} \sum_{i=1}^{N_t} (L_{t_i}(\mathbf{w}) - L_{t_i}(\mathbf{w}'))^2 \right)^{1/2}.$$

Using Eqn.17, we get $d_{\mathcal{T}}(\mathbf{w}, \mathbf{w}') \leq K \|\mathbf{w} - \mathbf{w}'\|$, where $K := (L_{\phi}/p_{\min})$. Then, the covering number of the function class \mathcal{L}_t with respect to pseudo-metric $d_{\mathcal{T}}$ is bounded above as

$$\mathcal{N}(\varepsilon, \mathcal{L}_t, d_{\mathcal{T}}) \leq \mathcal{N}(\varepsilon/K, \mathcal{W}_B, \|\cdot\|_2) \leq \left(\frac{3KB}{\varepsilon} \right)^c.$$

Finally, we apply Dudley's theorem, which we restate here for convenience. For more details, please refer to [76, Example 5.24].

Theorem (Dudley's Theorem). *Let \mathcal{F} be a class of real-valued functions from $S = \{z_1, \dots, z_n\}$ to \mathbb{R} . Define the empirical pseudo-metric $d_S(f, g) := \sqrt{\frac{1}{n} \sum_{i=1}^n (f(z_i) - g(z_i))^2}$. Then the empirical Rademacher complexity of \mathcal{F} satisfies*

$$\hat{\mathfrak{R}}_S(\mathcal{F}) \leq \frac{24}{\sqrt{n}} \int_0^{\text{diam}(\mathcal{F}, d_S)} \sqrt{\log \mathcal{N}(\varepsilon, \mathcal{F}, d_S)} d\varepsilon,$$

where $\text{diam}(\mathcal{F}, d_S) := \sup_{f, g \in \mathcal{F}} d_S(f, g)$, and $\mathcal{N}(\varepsilon, \mathcal{F}, d_S)$ denotes the ε -covering number of \mathcal{F} with respect to the metric d_S .

In our setting, the function class is \mathcal{L}_t and the empirical metric is $d_{\mathcal{T}}$. The radius can be bounded as $\text{diam}(\mathcal{L}_t, d_{\mathcal{T}}) \leq 2(-\log p_{\min})$. With this bound in hand, define $L_{\max} := \min\{3KB, 2(-\log p_{\min})\}$. We now derive the following sequence of inequalities.

$$\begin{aligned} \hat{\mathfrak{R}}_{\mathcal{T}}(\mathcal{L}_t) &\leq \frac{24}{\sqrt{N_t}} \int_0^{L_{\max}} \sqrt{c \log \left(\frac{3KB}{\varepsilon} \right)} d\varepsilon = \frac{72KB\sqrt{c}}{\sqrt{N_t}} \int_{\log \left(\frac{3KB}{L_{\max}} \right)}^{\infty} \sqrt{u} e^{-u} du \\ &\leq \frac{72KB\sqrt{c}}{\sqrt{N_t}} \int_0^{\infty} \sqrt{u} e^{-u} du = \frac{36L_{\phi}B\sqrt{\pi c}}{p_{\min} \sqrt{N_t}}. \end{aligned}$$

This completes the proof of Proposition 4.